Title
Thermal and Electrochemical Light Alkane Upgrading

Author
Gurses, Muhammet Sadi

Publication Date
2022

Peer reviewed|Thesis/dissertation

Thermal and Electrochemical Light Alkane Upgrading

By

MUHAMMET SADI GURSES

DISSERTATION

Submitted in partial satisfaction of the requirements for the degree of

DOCTOR OF PHILOSOPHY

in

Chemical Engineering

in the

OFFICE OF GRADUATE STUDIES

of the

UNIVERSITY OF CALIFORNIA

DAVIS

Approved:

Coleman Kronawitter, Chair

David Osborn

Ambarish Kulkarni

Committee in Charge

2022

In dedication to my wife and other family members: my dad, mom and sister who encouraged and supported me all along this journey.

Contents

Thermal and Electrochemical Light Alkane Upgrading

Abstract

The dramatic increase in supply of natural gas in the U.S. presents a unique opportunity to develop new catalytic processes that utilize light hydrocarbons for chemical manufacturing and fuel synthesis. Conventional catalytic processes utilize extreme conditions requiring high energy input for the initial C-H bond activation and multiple-step processes for the conversion of activated compounds into higher-value products. Direct conversion routes, on the other hand, have been investigated and have shown promising results toward more-efficient utilization of natural gas resources. In this dissertation, direct conversion routes are classified into three different categories: liquid-phase thermal catalysis, electrocatalysis, and gas-phase thermal catalysis. Investigations involving each of these conversion routes are presented, adding new fundamental information on light alkane upgrading to contribute to the existing literature.

First, liquid-phase thermal catalysis was studied by utilizing unsupported AuPd nanoparticles and H_2O_2 as an oxidant in water. Numerous C_2 oxygenates, including ethyl hydroperoxide/ethanol, acetaldehyde, and acetic acid were generated with maximum-observed oxygenate yield of 7707 μmol $g_{AuPd}^{-1} h^{-1}$ from ethane at 1 bar and 21 °C. In addition, continuous supply of low H_2O_2 concentrations to a semi-batch reactor over 50 h showed that on-site generated H_2O_2 can serve as an oxygenate-selective oxidant of ethane. Given that, electrochemical approaches could serve as the basis to continuously and sustainably generate the H_2O_2 fed into the chemical reactor to partially oxidize light hydrocarbons. In fact, utilizing air and water under electochemical potential can simply produce H_2O_2. Chapter 3.2 introduces an electrocatalyst that is engineered from electrochemical deposition of Pd ions during O_2 reduction. This catalyst showed an extreme activity towards selective production of H_2O_2 which is determined as the second-highest partial kinetic current density for H_2O_2 production in acidic media reported in the known literature.

The second direct conversion system, electrocatalysis, was also investigated to provide fundamental knowledge about how to effectively activate and functionalize the C-H bond. For this purpose, a prototypical electrocatalyst surface, polycrystalline Pt, was employed to assess the interaction of it with methane and water. Experiments performed by anodic stripping voltammetry

techniques coupled with operando surface-enhanced infrared absorption spectroscopy (SEIRAS) indicated that the sites with lower Pt coordination number (defects or step-edges) are potentially responsible for initial C-H bond activation and its decomposition to surface-bond C-H-O or C-O fragments.

For the last direct conversion route, oxidative coupling of methane (OCM) was considered as the model system and proposed to be investigated by near-surface optical and mass spectrometry techniques. These diagnostic techniques were initially gauged for the partial oxidation of methanol over a silver catalyst to demonstrate the value of the near-surface gas-phase measurements. The success in mapping out the coupling between the gas-phase and surface in heterogeneous catalysis encouraged us to work on the identical system with different metal surfaces. Chapter 4 mainly exhibits the studies on conversion of methanol near atmospheric pressure using molecular beam mass spectrometry on Pd film surfaces. Methoxymethanol,a rarely observed intermediate, was detected and provided as a supporting evidence to previously proposed reaction networks. Later, in order to shift the direction to OCM reaction, the near surface techniques were modified and optimized with the knowledge gathered during methanol oxidation experiments. Preliminary experiments were conducted on OCM and initial results were included in the Appendix of Chapter 4.3.5. More promising results including the radical detection are expected to be obtained in order to elucidate the complex reaction network taking place on the surface and near-surface.

Overall this thesis extensively covers the direct conversion methods for the utilization of light hydrocarbons and provides the detailed experimental procedures in the context of the comprehensive literature.

Acknowledgments

I would like to thank my PI, Prof. Coleman Kronawitter who made me start thinking differently from the very first meeting we had. I still remember our first meeting where he described me the overall goal of the research in his mind on a white board by drawing the design of the reactor serving for different purposes. I am at least happy that we were able to fabricate somewhat similar version of that drawing eventually. I feel very lucky for being his first PhD student. Since we met right at the transition states of our own career paths, I always think of him as more of a friend whom I trust from heart than a PI. Nevertheless, this friendship has never hindered my deep respect for him and his scientific vision and decisions. In fact, this was one of the greatest reasons behind my strong motivation to achieve the project goals throughout my PhD. At this point, I should also mention my dear friend and lab-mate Noah Felvey who participated and provided great help during the lab set-up and all along the way. I will truly miss the days and nights we spend together to set up the lab. I would like to also thank my other lab-mates and friends: Yulei Wang, Ozge Bayoglu, Leah Filardi, Niko Hansen, Patrick Beckett, Jose Hernandez, Brendan Boudreaux.

I would like to also acknowledge and thank Prof. Ambarish Kulkarni and Prof. David Osborn for serving on my thesis committee. I inspired a lot from Prof. Kulkarni on how to be confident on and support your own research ideas and Prof. Osborn on how to deliver an extremely complex subject in a simple way.

The last two years of my PhD was mostly focused on a research project with a collaboration of Sandia National Laboratories funded by a DOE grant DE-SC0020320. I had a chance to work with Dr. Nils Hansen who was my PI at the Sandia National Laboratories, Livermore and taught me how to use a special near-surface probing instrument and analyze the data driven. Therefore, I would also like to thank him for his exceptional guidance.

I would like to also thank my big family members for never leaving me alone with daily basis video calls from thousands miles away and always encouraging me throughout this journey. I would like to point out my sister, Fikos particularly for her unconditional support.

Finally, I would like to especially thank my sweet wife, Sevin for always being there for me. I am so grateful for having you in my life and can't wait to see our upcoming journeys.

CHAPTER 1

Introduction

1.1. Motivation of the research

The production of natural gas has increased considerably with the development of drilling techniques for the extraction of shale gas, a form of natural gas, and shale oil. It is projected that this trend will continue and the natural gas and oil in the U.S. will be a reliable energy source for the near future. [**2**, **3**] In addition, when extracting oil from geographically remote oil fields, often the distance between the source and existing refineries and pipelines prevents efficient utilization of the natural gas obtained during oil extraction. In these situations, natural gas is considered a byproduct and of less value than the oil produced from the same source. Consequently, natural gas obtained during oil extraction is vented or more often flared to CO_2 before release into the environment.

This is because natural gas has greater global warming potential than CO_2. In 2020 the amount of natural gas vented and flared was nearly 420 Bcf (billion cubic feet), which was almost 10% of residential natural gas consumption in that year across U.S. [**1**] These observations highlight the

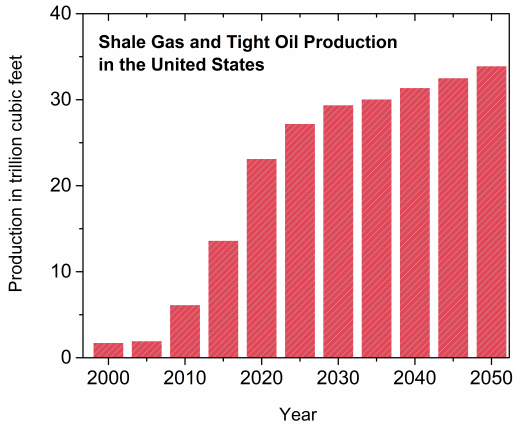

FIGURE 1.1. Shale gas and oil production across United States. [**3**]

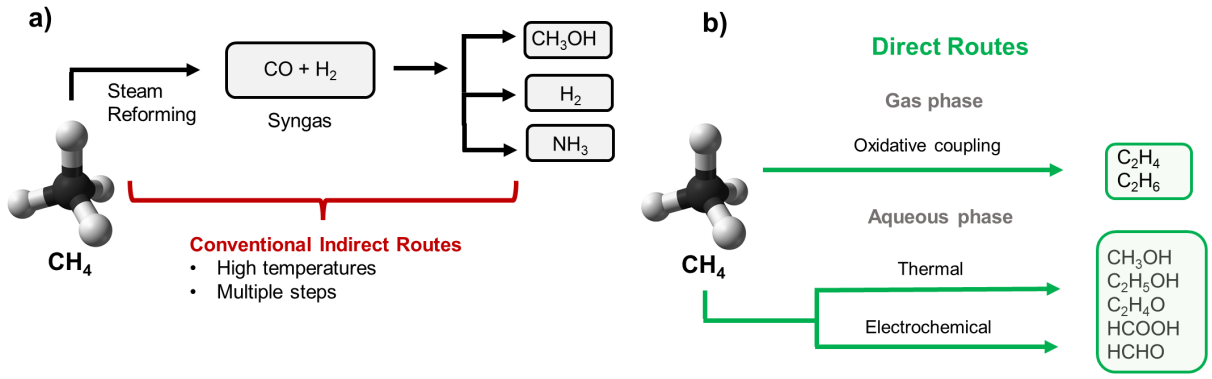

SCHEME 1.1. Comparison of (a) conventional conversion routes with respect to (b) direct conversion methods for methane utilization

urgent need to engineer new direct conversion technologies that utilize wasted natural gas that are economically efficient and have minimum environmental impact. Upgrading the light alkanes, which comprise more than 90% of the components of natural gas, to value-added commodity products would provide an efficient solution for the utilization of natural gas resources. For these conversions, it is beneficial for operating conditions to be mild - near ambient temperature and pressure - to increase the feasibility of distributed facilities.

Light alkane upgrading has been a subject of great interest for years. [**7**, **13**, **93**] Specifically, many studies have been performed to explore alternative ways for the conversion of methane, most abundant chemical component of natural gas. [**13**, **83**] However, methane is an extremely stable chemical compound due to the non-polar chemical bonds of methane associated with the largest C-H bond strength of any alkane. Therefore, extreme conditions are required to activate C-H bond of methane. The conventional methods for the conversion of methane utilizes multi-step processes, including steam reforming and subsequent catalytic reactions as demonstrated in Scheme 1.1a. The direct route to produce chemicals (Scheme 1.1b) from methane is rather challenging but usually thermodynamically favorable in the presence of biological catalysts such as methane monooxygenase. [**11**] This enzyme can convert methane to methanol under ambient condition by utilizing O_2 species as an oxidant. Motivated by the nature, Hutchings et al. showed that copper-promoted Fe-ZSM-5 catalyzes the oxidation of methane to methanol using hydrogen peroxide in water. [**58**] This has proven that homogeneous liquid-phase systems in near ambient conditions are especially

promising for selective oxidation of methane to methanol. Later, the same group conducted a similar approach and was able to improve the selectivity towards methanol by utilizing AuPd catalyst. [**4**] However, it is also noted that hydrogen peroxide is not industrially viable oxidant, because it is itself a commodity chemical. Alternatively, heterogeneous liquid-phase electrochemical processes provide a unique opportunity to overcome the need of oxidizing agent by utilizing the water as an oxidant source. For instance, Mustain et al. first established that electrochemical processes enable the direct partial oxidation of methane to methanol and other oxygenates at room temperature on the surfaces of metal oxide and (oxy)hydroxide catalysts. [**129**] Later, follow-up studies have also shown that the partial anodic oxidation of methane is promising in terms producing C_{1-3} products at ambient conditions. [**71**, **98**, **110**] However, the overall selective conversion of methane is still under the need of industrial and commercial applications. As shown in Scheme 1.1b, oxidative coupling of methane (OCM) is another promising direct method for converting methane to higher hydrocarbons especially ethylene. [**78**] OCM is more of a complex process consisting of both homogeneous (gas-phase coupling) and heterogeneous (interactions of surface adsorbents) catalysis. It requires elevated temperatures to convert methane into higher hydrocarbons. [**78**, **108**] Nevertheless, a recent study, that has proposed OCM activity below 400 °C, indicates the potential of OCM as an alternative direct conversion route. [**92**]

1.2. Overview of dissertation

This thesis aims to provide the experimental approaches conducted to upgrade light alkanes to higher-value commodity chemicals. All three different direct conversion systems as mentioned in the motivation section 1.1 such as liquid-phase thermal catalysis (Chapter 2), electrocatalysis (Chapter 3) and gas-phase thermal catalysis (Chapter 4) were investigated individually.

We initially explored the partial oxidation of ethane,is the second most abundant component of natural gas. This is because it is slightly more soluble in water and reactive than methane. Therefore, utilizing ethane as the reactant is experimentally more convenient to start exploring the essentials of selective light alkane oxidation. Chapter 2 presents the results obtained from conversion of ethane to oxygenates on unsupported AuPd catalyst under mild conditions. H_2O_2 was used as an oxidizing agent consistent with the context of the specific work in literature. Dramatic effect of oxidant concentration over the products' distribution has revealed the importance of utilizing H_2O_2 efficiently, which is denoted as the gain factor throughout the study. Since it is known that H_2O_2 is not a commercially viable oxidant, an alternative approach was suggested by considering the on-site electrochemical production of H_2O_2. A hand-made semi-batch reactor (see Figure 1.2) was employed to simulate the consumption of H_2O_2 which would be generated electrochemically and supplied to reactor continuously. Our results showed that H_2O_2 can be utilized much more efficiently with the continuous supply of the low concentrated oxidant as it would be in the case of electrochemical production. Therefore, in Chapter 3.2, our initial focus was developing an electrocatalyst for the selective production of H_2O_2 from water. Simultaneously, electrochemical oxidation of methane on Pt surface was investigated to benchmark our abilities for the electrochemical C-H bond activation. A well-studied Pt electrode was selected for this purpose and operando FTIR measurements were performed to understand the fundamentals of methane activation over polycrystalline metal surfaces. We were not able to perform a detailed study on simultaneous electrochemical production of H_2O_2 and the utilization of it for the selective light alkane oxidation. Nevertheless, we were able to engineer and test all of the systems and reactors that are essential for conducting experiments on this complex operation. The developed hand-made reactors, which were utilized in Chapter 2 and 3, are listed in the reactor design section 1.3 of this chapter.

In Chapter 4, the direction was shifted to the gas-phase conversion methods which was mainly about oxidative coupling of methane. To investigate this sophisticated system that involves both surface interactions and gas phase collisions, we collaborated with Sandia National Laboratories, Livermore. Through use of the unique near-surface gas-phase characterization techniques, it was aimed to fill the knowledge gap that exists in the near-surface gas-phase and its properties and contribution to catalytic mechanisms. However, the complex nature of OCM and the necessity of elevated temperature led us to benchmark our system over a relatively simple reaction. Partial oxidation of methanol was chosen as the test reaction because it is not only relatively convenient to work on but also has the identical initial dehydrogenation of C-H bond step with OCM. [**123**] Therefore, Chapter 4.2 initially presents the results of bench-marking of near-surface measurement techniques for methanol oxidation above silver catalyst. Motivated by the promising results obtained on Ag surface, we also extensively investigated methanol oxidation on Pd film catalyst. We were able to detect methoxymethanol, previously proposed as an obscure intermediate, with the help of unique instrument provided by Sandia National Laboratories. Further studies were also performed on supported catalyst but the current results were not included in this dissertation. The overall system was prepared to perform controlled experiment for OCM and initial results are included in the Appendix 4.4 of Chapter 4.

1.3. Fabrication and optimization of the reactors for light alkane upgrading

1.3.1. Reactor Design. Low solubility of light hydrocarbons in water limits the flux of reactants reaching to the catalyst surface. Therefore, an optimized reactor was needed to be fabricated to enhance the efficiency of light alkane utilization. During first couple of years of my PhD, I designed and fabricated different reactors for various catalysis systems to perform the planned experiments. For instance, liquid-phase thermal catalysis experiments in Chapter (2) were conducted by employing a hand-made semi-batch reactor presented in Figure 1.2.

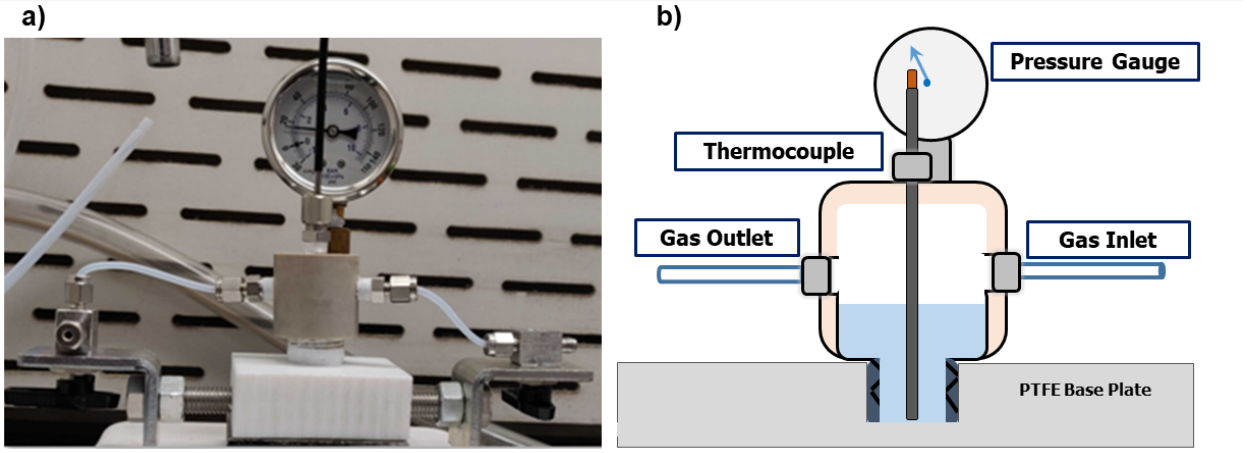

FIGURE 1.2. a) real photo, b) cartoon diagram of the liquid-phase thermal catalysis reactor.[a,b,c]

[a] 1-10 bar operating pressure range (alkane and O_2 mixtures).

[b] 10-80 °C operating temperature range.

[c] Fully compatible with operando surface-enhanced infrared spectroscopy (bottom mounted electrode).

Thermal reactor (Fig. 1.2) is made from PEEK (polyether ether ketone) material which is resistant to corrosive liquids mostly preferred in electrochemistry measurements. The reactor consists two different threaded parts (head and bottom plate) that are designed to be tighten into each other by hand. This also facilitates the coupling of head part into a different bottom plate that is designed to be compatible with FTIR optic box. The reactor was also optimized to be run with a low electrolyte volume (5 ml) for enhancing the concentration of products generated during the reaction. A thermocouple attached into a threaded port which was later used for the

continuous flow of H_2O_2 during semi-batch reactor experiments in Chapter 2. The three-way valves in the inlet and outlet was used for bypassing and gas-sampling, respectively. The gas sampling for the GC measurement was performed by using a syringe that collects the sample from a septum attached to the tube fitting at the outlet. Heating and stirring was done with a hot plate from the bottom of the reactor. This design was sufficient for performing liquid-phase thermal reactions but does not contain any electrode ports. Therefore, an updated prototype was needed for conducting electrochemical measurements.

An identical design with the thermal reactor (Fig.1.2) including three electrode ports was assembled (Figure 1.3). The working electrode is mounted from the bottom with an extra electrode holder piece in order to not only making it compatible with FTIR spectrometer but also increasing the geometric surface area of the electrode facing the electrolyte. A rare earth magnet was coupled from the side for stirring.

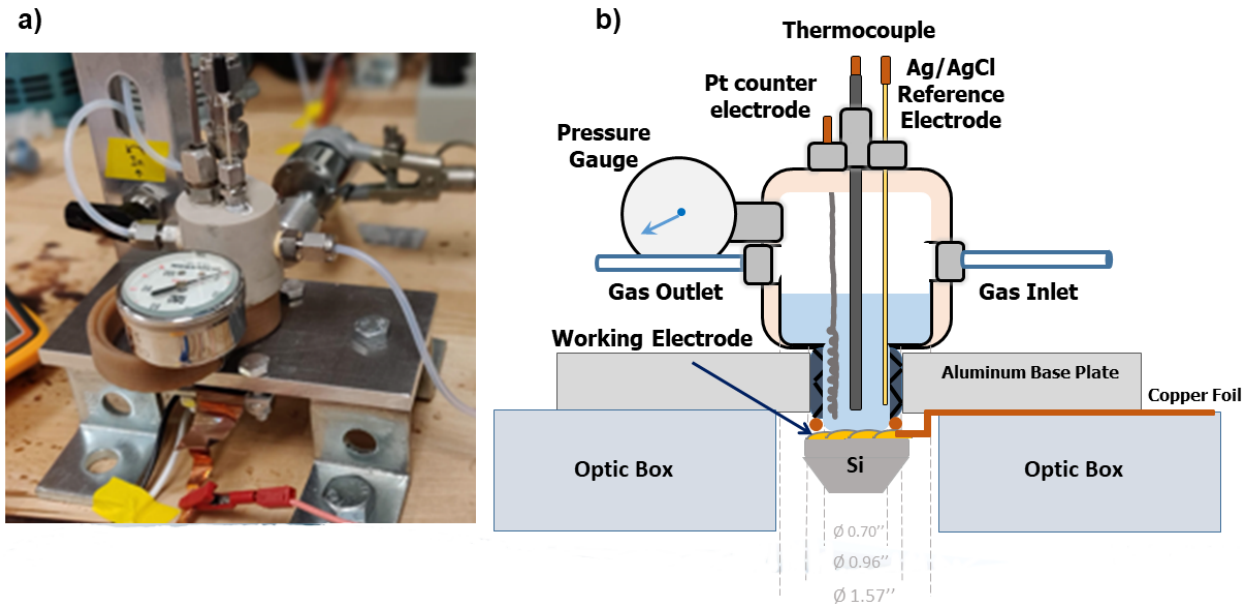

FIGURE 1.3. a) real photo, b) cartoon diagram of the electrocatalytical reactor.[a,b,c,d]

[a] 1-3 bar operating pressure range (alkane and O_2 mixtures).

[b] 10-80 °C operating temperature range.

[c] Electrochemical polarization; three-or two- electrode configuration with 5 ml electrolyte volume.

[d] Fully compatible with operando surface-enhanced infrared spectroscopy (bottom mounted electrode).

Although our second prototype works adequately for anodic oxidation reactions, it was still required to be upgraded in order to achieve our main goal, which is the partial oxidation of light alkanes with the supply of electrochemically produced H_2O_2. Electrochemical H_2O_2 production requires the reduction of O_2 in water at relatively more negative (cathodic) potentials resulting the generation of negative currents at the working electrode.(see Chapter 3.2) This means that the counter electrode will be at more positive (anodic) potentials to supply the current needed for the completion of circuit. This usually causes the oxidation of the products at the cathode that are originally generated at the working electrode surface. Therefore, an ion exchange membrane separating working and counter electrode compartments is essential for this type of a reaction. The electrochemical reactor in Figure 1.4, which was carefully designed for product isolation with an ion-exchange membrane, provides all the required specifications to employ the proposed reactions.

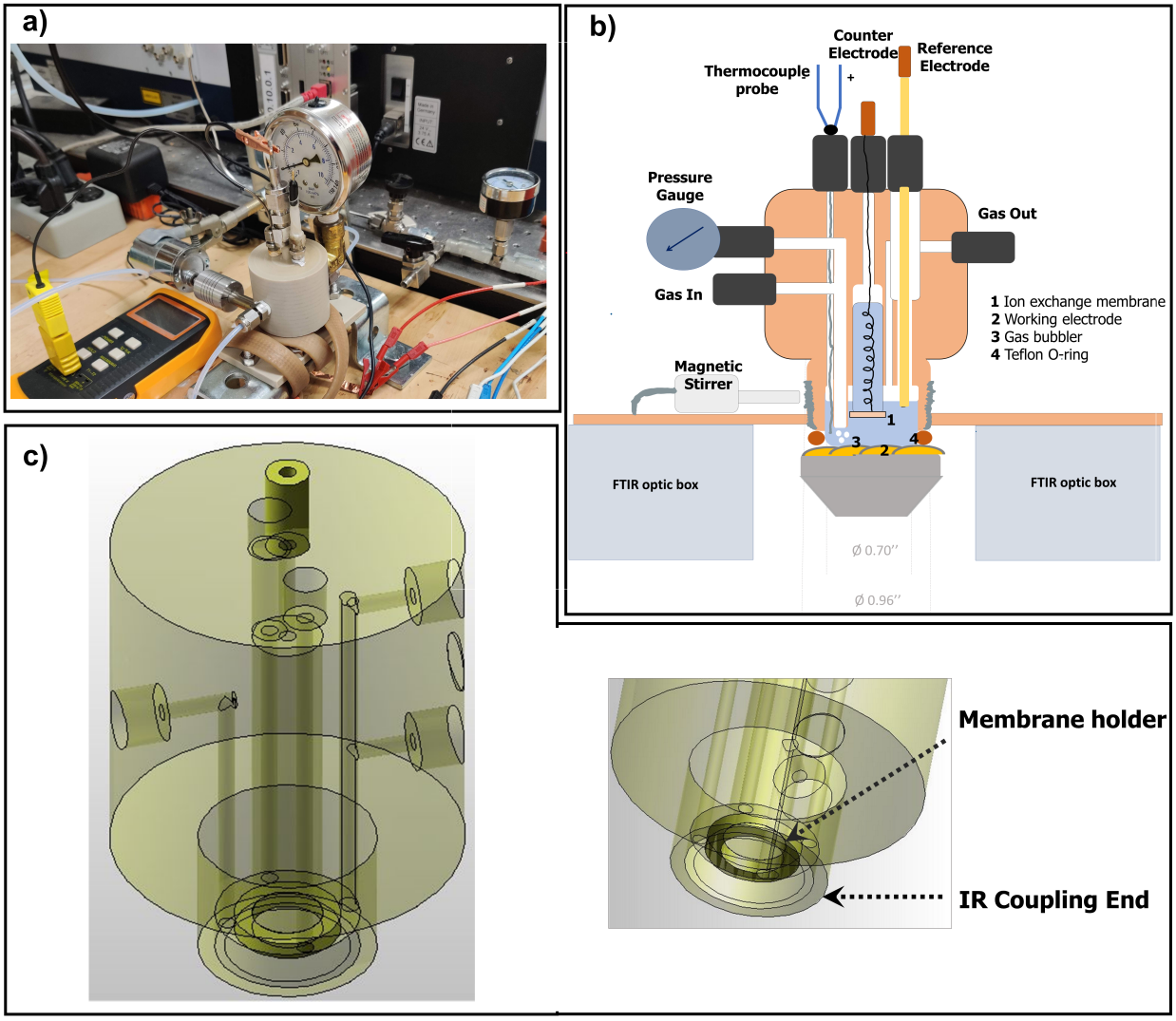

FIGURE 1.4. a) real photo, b) cartoon diagram, c) CAD drawings of hybrid thermal-electrocatalytic reactor.[a,b,c,d,e]

[a] 1-10 bar operating pressure range (alkane and O_2 mixtures).

[b] 10-80 °C operating temperature range.

[c] Electrochemical polarization; three-or two- electrode configuration with 2 ml electrolyte volume.

[d] Ion exchange membrane for the product isolation (analyte-catalyte seperation).

[e] Fully compatible with operando surface-enhanced infrared spectroscopy (bottom mounted electrode).

1.3.2. Optimization of reactor design to be able to perform operando surface enhanced infrared radiation adsorption spectroscopy (SEIRAS) measurements. Internal reflection of an IR light in a high refractive index IR crystal is used to create an evanescent wave on the metal (or catalyst) surface deposited on the crystal. The created evanescent wave interacts with the near-surface and surface-bound species, and provides information on composition of species on the surface during reaction. The deposition of reflective layer comprised of metal nanoparticles, rather than a continuous metal layer, localizes the electromagnetic field associated with the IR light interaction,(see Scheme 1.2) ultimately making the measurements even more surface sensitive. This signal enhancement is called as SEIRAS effect and this technique started to be commonly used for detecting surface bound species generated during an electrochemical reaction. Details on SEIRAS method and the deposition of SEIRAS active film can be found in the experimental section 3.3.3 of Chapter 3.3. Motivated from the promising results of this technique in literature, [**130**] we have decided to engineer all of our reactors in a way of being compatible with operando FTIR measurements. Scheme 1.2 provides the overall diagram of the fabricated hybrid reactor positioned on top of the FTIR box. The scheme also illustrates the real image of an silicon oxide IR crystal with a film of Au nanospheres deposited on.

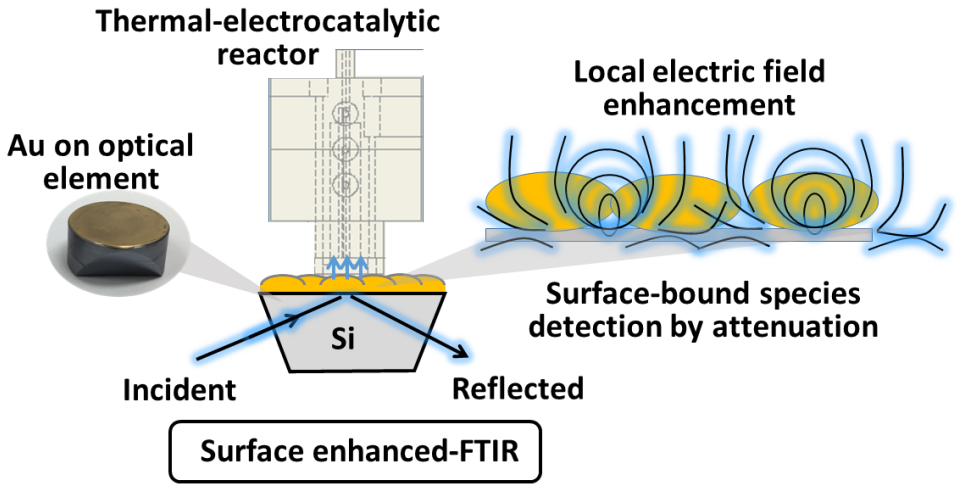

SCHEME 1.2. Hybrid thermal-electrocatalytic reactor coupled to Surface Enhanced Infrared Radiation Adsorption Spectroscopy

CHAPTER 2

Aqueous phase thermal catalysis for light alkane upgrading*

Chapter 2 is adapted from a published work:

Y.L. Wang,‡ S. Gurses,‡ N. Felvey, C.X. Kronawitter; Room temperature and atmospheric pressure aqueous partial oxidation of ethane to oxygenates over AuPd catalysts. *Catal. Sci. Technol.*, 2020, **10**, 6679-6686. (‡Equal contributors)

2.1. Overview of chapter 2

The exceptional activity of biological catalysts, methane monooxygenase, towards selective methanol production from methane serves as the basis of the motivation for the researches on homogeneous liquid-phase systems in near ambient conditions. Existing literature as discussed in the Chapter 1 indicates the unique opportunity of utilization of this system for understanding the selective C-H bond activation. After a comprehensive literature review, we designed our first experimental approach over a liquid-phase thermal catalysis to be able to understand the fundamentals of C-H bond functionalization in light alkanes. Partial oxidation of methane has been broadly explored in liquid-phase thermal catalysis. [**141**] Whereas studies on ethane oxidation is limited, although it is the second most abundant component of natural gas. Moreover, utilizing ethane as the reactant presents some experimental advantages due to its relatively higher solubility and reactivity in water with respect to methane. Therefore, we started our investigations on partial oxidation of ethane. To enhance the solubility of ethane in water, which is one of the major obstacles

*The content of this chapter has previously been published in Ref. [**179**].

for efficient liquid-phase light alkane upgrading, a hand-made reactor working at elevated pressures was fabricated.(Figure 1.2) Most of the experimental work throughout this study was performed in this reactor. This chapter introduces the studies we have performed under this content.

2.2. Room temperature and atmospheric pressure aqueous partial oxidation of ethane to oxygenates over AuPd catalysts

2.2.1. Abstract. New modes of chemical manufacturing based on small-scale, distributed facilities have been proposed to supplement many existing production operations in the chemical industry, including the synthesis of value-added products from light alkanes. Motivated by this prospect, herein the aqueous partial oxidation of ethane over unsupported AuPd nanoparticle catalysts is investigated, with emphasis on outcomes for reactions occurring at 21 °C and 1 bar ethane. When H_2O_2 is used as an oxidant, the system generates numerous C_2 oxygenates, including ethyl hydroperoxide/ethanol, acetaldehyde, and acetic acid. Ethyl hydroperoxide is found to be the primary product resulting from the direct oxidation of ethane: it is produced with 100% selectivity in batch reactions with short durations and with low initial H_2O_2 concentrations. At longer times or in more oxidizing conditions, deeper product oxidations expectedly occur. Product distributions differ when H_2O_2 is replaced by H_2 and O_2 in the headspace. Additionally, to simulate a scenario wherein H_2O_2 is produced on-site and to study ethane oxidation in steady, low H_2O_2 concentrations over 50 h, a semi-batch configuration facilitating continuous injection of dilute H_2O_2 was implemented. These efforts showed that H_2O_2 can serve as an oxygenate-selective oxidant of ethane when its concentration is kept low during reaction. These and other experimental results, as well as initial computational results using density functional theory, suggest that paths forward for aqueous ethane conversion exist, and systems should be engineered to emphasize product stabilization.

2.2.2. Introduction. The rapid discovery of geographically dispersed sources of unconventional feedstocks has provided considerable motivation for the chemical industry to pursue distributed chemical manufacturing as a supplemental mode of production. [**16**, **181**] Advances in renewable energy technologies and the associated reduction in energy costs at remote locations provide further impetus for development of a distributed network of chemical production facilities. Given the reduced scale and the nature of geographically distributed resources, new technologies

that facilitate the catalytic direct functionalization of small molecules in mild conditions (low temperature and pressure and with minimal environmental impact) are expected to be paramount for any significant adoption of distributed chemical manufacturing schemes.

The widespread use of small molecule feedstocks would have parallel disruptive effects on the global chemical industry, which currently relies heavily on conventional petroleum resources. Molecules of interest in this context include the light alkanes - the primary constituents of natural gas - whose global abundance and utility have been made apparent by the recent shale gas revolution, [**124**, **156**] as well as CO_2, H_2O, O_2, and N_2, the utilization of which is considered critical for future sustainability in the energy sector as well as other high-energy-use sectors, including chemical synthesis. [**43**, **138**, **164**, **193**]

In order to develop these technologies, it is essential to explore the behaviors of catalytic systems in relevant mild conditions – especially near room temperature and atmospheric pressure. Although the optimal operating conditions for catalysis will vary greatly among relevant reactions and processes, even for systems that are required to operate at elevated temperatures, knowledge of the reactivity and stability of products in the reaction medium at room temperature is of critical value. Oxidative functionalization of light alkanes is particularly relevant in this context. The local generation of products that exist in the liquid phase at standard temperature and pressure would alleviate distribution and utilization constraints that result from the transportation of large volumes of flammable gases from remote sources. [**7**] Although the aliphatic C–H bonds of light alkanes are strong, e.g. CH_4 (439 kj/mol) [**137**] and C_2H_6 (421 kj/mol) [**197**] with respect to longer chain alkanes as C_4H_{10} (400 kj/mol) [**197**] or alkly aromatics as toluene(C_7H_8) (324 kj/mole) [**165**], a number of catalysts have been studied for the low-temperature oxidative functionalization of alkanes to produce oxygenates including alcohols, aldehydes, and acids. [**4**, **6**, **58**] Ethane is typically the second-most abundant constituent of natural gas, and although its direct low-temperature partial oxidation has not received the same level of attention as that of methane, [**141**] it is a promising feedstock for the distributed production of oxygenates in mild conditions. [**7**] Here, the direct partial oxidation of ethane at unsupported colloidal AuPd nanoparticle catalysts suspended in water is examined.

2.2.3. Results and discussion. Stabilizer-free AuPd (1: 1 molar ratio) nanoparticles were prepared via adaptation of standard colloidal synthesis procedures involving reduction of metal precursors ($PdCl_2$ and $HAuCl_4$), followed by heat treatment (100 °C). Complete synthesis details are provided in the experimental methods.2.2.5 An X-ray diffractogram (XRD) of the AuPd catalyst particles (Fig. 2.1 a) indicates a diffraction pattern with peaks centered at intermediate values between those of metallic Au (PDF#04-0784) and metallic Pd (PDF#46-1043), confirming the formation of an alloy. [**173**] High-angle annular dark-field scanning transmission electron microscopy (HAADF-STEM) images reveal that the AuPd crystals possess multiply twinned lattice fringes, but nanoparticle agglomeration resulting from dispersion onto the TEM grid prevents distinguishing the prevalence of icosahedral versus cuboctahedral structure, which has been true for other studies (Fig. 2.1 b and c). [**72**] The AuPd nanoparticles have a mean diameter of 4.93 nm with a narrow particle-size distribution (Fig. 2.1 d). Au 4f and Pd 3d X-ray photoelectron spectroscopy (XPS) results show that heat treatment of AuPd results in the formation of oxidized species Pd^{2+} and Au^{3+} (Fig. 2.1 e and f), as has been observed previously in AuPd-based catalysts. [**183**] However, no distinct surface phases were detected by XRD or energy dispersive X-ray spectroscopy (EDX) mapping (Fig. 2.5), a typical phenomenon reported in literature. [**196**] Three independent measurements were taken to determine the compositions of the catalysts: XPS, inductively coupled plasma atomic emission spectroscopy (ICP-AES) and EDX analysis Table 2.1. The Au: Pd molar ratio was determined by all techniques to be nearly 1: 1.

Catalytic activity was tested in a purpose-built reactor with all wetted components manufactured from chemically resistant PEEK plastic. In a typical batch experiment, 5 mL aqueous AuPd colloid (6.6 μmol of metals) was combined with hydrogen peroxide (H_2O_2) at room temperature (21 °C) with 1 bar (1 atm) of ethane (C_2H_6). To our best knowledge, this work represents the first example for aqueous partial oxidation of ethane to oxygenates occurring at room temperature and atmospheric pressure (Table 2.2). Liquid-phase products were quantified using 1H NMR through independent calibration curves generated from chemical standards (Figure 2.6), and gas-phase products were analyzed by gas chromatography (GC).

Figure 2.2 provides results of several aqueous batch reactor studies. The data indicate that AuPd catalyzes the partial oxidation of ethane to various oxygenates at room temperature and

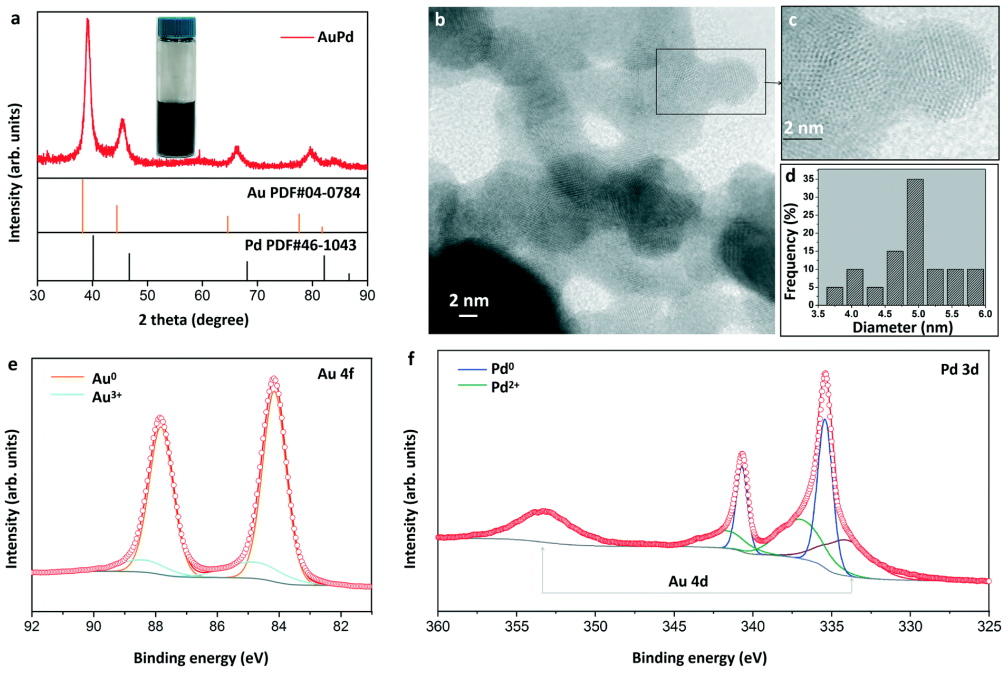

FIGURE 2.1. (a) XRD pattern of the nanoparticulate AuPd catalysts. Inset: A photograph of the aqueous AuPd colloidal suspension. (b) STEM image of AuPd catalysts. (c) Magnification of individual AuPd nanoparticles. (d) Size distribution of AuPd nanoparticles. (e and f) XPS spectra of AuPd in Au 4f and Pd 3d regions.

atmospheric pressure in the presence of (H_2O_2). To confirm this result, several control experiments were performed. It was determined that no liquid oxygenates were observed in the absence of either C_2H_6 or (H_2O_2), indicating that H_2O_2 was necessary to initiate the C_2H_6 oxidation reaction, similar to observations made in other reports. [**4**] Additionally, the potential influence of dissolved metal ions (with equivalent 6.6 μmole dissolved metal) was investigated; no products were observed in the presence of Au and Pd ions but in the absence of AuPd (Table 2.3, entry 1). In all C_2H_6 oxidation experiments, analysis of the headspace by GC revealed no CO_2 was present; however the relatively high solubility of CO_2 in water [**5**] prevents a definitive claim that no complete oxidation occurs (see discussion later in this report for evidence of acetic acid oxidation to CO_2 in alternate conditions used for mechanistic studies).

Figure 2.2 a provides the quantities of oxygenates produced and of H_2O_2 consumed at seven different initial H_2O_2 concentrations ($[H_2O_2]_{initial}$). It is shown that $[H_2O_2]_{initial}$ influences the

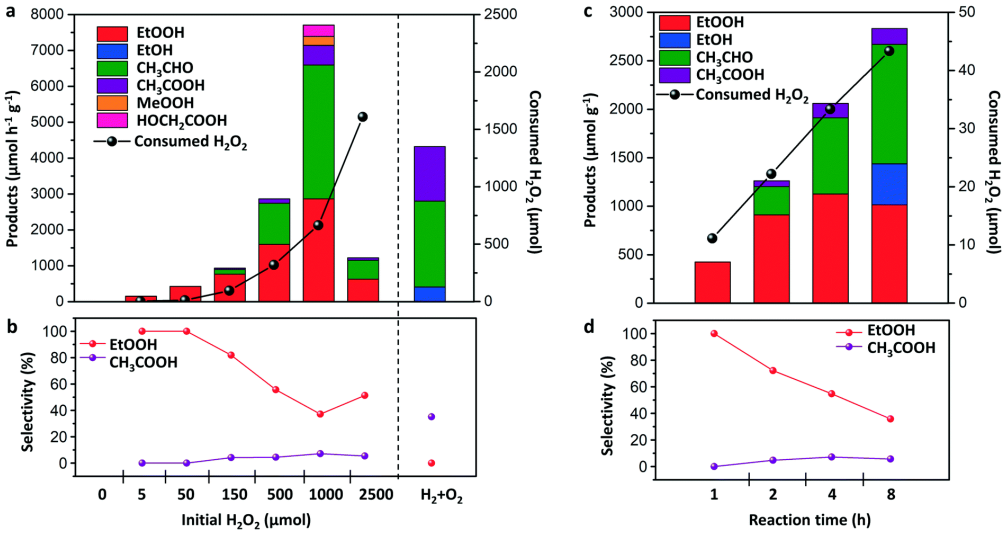

FIGURE 2.2. Catalytic activity of unsupported AuPd nanoparticles for C_2H_6 oxidation. (a) Quantities of oxygenates produced and of H_2O_2 consumed for seven initial quantities of H_2O_2, corresponding to 0, 1, 10, 30, 100, 200, and 500 mM $[H_2O_2]_{initial}$, respectively. The right-hand side shows results generated in the absence of H_2O_2 but in the presence of a H_2/O_2 mixture. Reaction conditions: 5 mL; 1 mg AuPd; 21 °C; 1 h; 1000 rpm; 1 bar C_2H_6 or 2.4 bar gas mixture (4.17% H_2, 16.7% O_2, 37.5% N_2 and 41.6% C_2H_6). (b) Selectivities of EtOOH and CH_3COOH for reactions in (a). (c) Quantities of oxygenates produced and of H_2O_2 consumed for multiple reaction times. Reaction conditions: 5 mL; 1 mg AuPd; 10 mM $[H_2O_2]_{initial}$ (50 μmol); 1 bar C_2H_6; 21 °C; 1–8 h; 1000 rpm. (d) Selectivities to EtOOH and CH_3COOH for reactions in (c).

product yields and selectivities, as well as the efficiency of H_2O_2 utilization in the oxidative C-H functionalization process. The selectivity to ethyl hydroperoxide (CH_3CH_2OOH, EtOOH) was 100% when the $[H_2O_2]_{initial}$ was lower than 30 mM. Given this remarkable result, the batch reaction with 10 mM $[H_2O_2]_{initial}$ was repeated seven times to verify that EtOOH was the sole product in these conditions. At higher $[H_2O_2]_{initial}$, acetaldehyde (CH_3CHO) and acetic acid (CH_3COOH) were observed (Figure 2.2a). Additionally, it was observed that the maximum amount of liquid oxygenates (7707 μmol gAuPd^{-1} h^{-1}) was obtained for 200 mM $[H_2O_2]_{initial}$ (Figure 2.2a and 2.7). The efficiency of H_2O_2 utilization was also quantified. The gain factor (defined as mol oxygenates/mol H_2O_2 consumed) [**4**] was highest for low-$[H_2O_2]_{initial}$ reactions (Table 2.4, entries 1–7). This phenomenon has been previously observed [**4**] and can be attributed to the fact that H_2O_2 adsorption and decomposition competes with C_2H_6 adsorption for surface sites. [**5**,**118**] When the reaction whose results are reported in Figure 2.2 c was studied with 10 bar C_2H_6 and the same

$[H_2O_2]_{initial}$, a much greater quantity of EtOOH was formed (Figure 2.8), which is consistent with the existence of a competition for reactant adsorption.

In the reactions above, the decomposition products (*OH and/or *OOH) of H_2O_2 [**136**] are the active oxidants of the dissolved alkanes (a more detailed discussion is later provided under Figure 2.4); the results above suggest the existence of competition and cooperativity between C_2H_6 oxidation and H_2O_2 decomposition. H_2O_2 is itself a valuable commodity chemical – it is desirable to generate this compound or its reactive fragments in situ from O_2 and H_2. To explore the efficacy of this approach to the partial oxidation of ethane at unsupported AuPd nanoparticles, ethane was co-fed with O_2 and H_2 to the reactor in the absence of H_2O_2. The righthand sides of Figure 2.2 a and b show the results of these experiments. It was observed that the distribution of products differs considerably from that obtained through external H_2O_2. Specifically, a much higher ratio of CH_3COOH to EtOOH was obtained through co-fed H_2 and O_2. It was also observed that ethanol (CH_3CH_2OH, EtOH) comprised a significant fraction of products, which was not observed through direct oxidation by H_2O_2.

Direct comparison of C_2H_6 oxidation rate resulting from in situ reaction of H_2 and O_2 and from a finite $[H_2O_2]_{initial}$ is difficult because the instantaneous concentration of H_2O_2 and its reactive fragments cannot be known. However, a reasonable approximation is possible by recognizing that in the catalytic synthesis of H_2O_2 at AuPd ($H_2 + O_2 \rightarrow H_2O_2$) in these conditions H_2 is the limiting reactant, which has been established in prior literature. [**39**, **40**] If all H_2 were consumed and converted transiently to H_2O_2, the initial partial pressure of H_2 in the experiment corresponds to 87 μmol H_2O_2 (17.4 mM) generated over the course of the batch reaction. The total quantity of oxygenates generated through reaction of co-fed H_2 and O_2 (ca. 4320 μmol h^{-1} $gcat^{-1}$) was 5–10 times greater than that was observed from reaction with H_2O_2 (425 and 934 μmol h^{-1} $gcat^{-1}$ for 10 and 30 mM $[H_2O_2]_{initial}$). It was considered that the presence of additional O_2 in the in situ experiments could influence product yields, but it was determined that this could be neglected: O_2 was also present in all experiments involving finite $[H_2O_2]_{initial}$ because it is a primary H_2O_2 decomposition product, and was quantified (Table 2.4).

Based on these observations, the most reasonable initial interpretation is that the positive effects on oxygenate yield and the change in product distributions resulting from co-fed H_2 and O_2 originate

from the presence of molecular H_2. Park et al. reported that molecular H_2 can be easily dissociated into atomic hydrogen (H*) over Pd atoms. [**76**] The H* could combine with molecular O_2 to produce H_2O_2. Most likely, intermediates generated during this process activate C_2H_6 and promote C_2H_6 oxidation. The observed EtOH could originate from direct C_2H_6 oxidation but also from EtOOH reduction by H*; this initial report of this catalysis does not facilitate direct determination of the mechanistic origin of EtOH in reactions with co-fed H_2 and O_2. Further dedicated mechanistic studies are underway to understand the distinguishing characteristics of catalysis driven by co-fed H_2 and O_2.

The 100% selectivity toward EtOOH observed at low $[H_2O_2]_{initial}$ (Fig. 2.2 a and b) motivated further time-online experiments of the reaction with fixed $[H_2O_2]$initial (10 mM) (Fig. 2.2 c and d). Both the total amount of liquid oxygenates and gain factor correlated positively with reaction time (2.4, entries 3, 8–10). With increasing reaction time, CH_3CHO and CH_3COOH were observed (Fig. 2.2 c), consistent with sequential oxidation of EtOOH to CH_3CHO and then CH_3COOH as proposed by Hutchings and coworkers. [**42**] Notably, EtOH was present at detected level at t = 8 h. Further C_2H_6 oxidation studies were performed at elevated temperature (50 °C) with multiple initial H_2O_2 concentrations. It was found that yields of EtOOH, CH_3CHO, and CH_3COOH increased with increasing $[H_2O_2]_{initial}$ from 100 mM to 200 mM, while the yield of EtOH decreased slightly (Table 2.5), indicating that increased initial quantities of H_2O_2 does not facilitate direct EtOH production. This is consistent with the results of the 21 °C reactions above (Fig. 2.2 a), which indicated that no EtOH was observed by increasing the initial amount of H_2O_2. To further explore the origin of EtOH observed in reactions occurring at 50 °C, product solution from a representative 50 °C reaction (with quantified amounts of EtOOH and EtOH) was stored in an NMR tube, in the absence of AuPd catalysts and of H_2O_2, and the products were analyzed after 6 days and after 12 days. As shown in Figure 2.9 EtOOH was found to spontaneously decompose to EtOH in time. These 50 °C reaction studies lead to the tentative conclusion that EtOH is first derived via EtOOH decomposition rather than C_2H_6 oxidation, and that increased temperature promotes EtOOH decomposition to EtOH. It is also possible that EtOOH can be reduced to EtOH by H* generated by H_2O_2 decomposition. [**76**] These studies indicate that in these conditions a competition

exists between EtOOH decomposition and EtOOH oxidation, with preference for EtOOH oxidation to CH_3CHO and CH_3COOH at relatively high H_2O_2 concentrations.

To generate a first approximation of operable reaction pathways, a series of direct oxidation studies were performed on the observed stable oxygenate products: EtOH, CH_3CHO, and CH_3COOH . An initial reactant concentration of 2 mM was selected because it is roughly the equivalent concentration of C_2H_6 in the conditions of the reactor studies above, as calculated based on known C_2H_6 solubility data. As shown in Figure 2.3 a, in the presence of 10 mM $[H_2O_2]_{initial}$, EtOH was oxidized primarily to CH_3CHO and CH_3COOH ; CH_3CHO was primarily converted to CH_3COOH . There is evidence for C–C bond breaking in these conditions: small amounts of the C_1 oxygenates CH_3OH (MeOH) and HCOOH were observed. C_1 products have been previously observed in aqueous C_2H_6 oxidation studies, where they were proposed to originate from methyl radicals resulting from C–C scission of C_2H_6 or C_2 reaction products. [**42**] No liquid- or gas-phase products were observed from oxidation of CH_3COOH with a 2 mM initial concentration (higher initial concentrations are considered below). Based on these observations, a high-level reaction pathway for aqueous C_2H_6 oxidation at colloidal AuPd was generated and is shown in Figure 2.3 b.

This study of ethane oxidation in mild conditions is motivated by the prospect that new modes of distributed chemical manufacturing can supplement or in some cases displace specific production operations in the chemical industry. In this context, H_2O_2 is also a notable commodity chemical whose production is a candidate for a transition to small-scale, distributed operations. H_2O_2 can be produced safely and with minimal environmental impact through electrochemical devices [**189**, **193**], (with air and water as reactants) and thermal catalytic microreactors [**111**] (with air and H_2 as reactants). Additionally, the expense of H_2O_2 production through the traditional anthraquinone process [**193**] and its subsequent transportation is expected to place additional cost burdens on any small-scale alkane conversion facility. Although source-dependent, the cost of H_2O_2 is approximately \$0.345 per lb (50% solution), and the cost of freight is estimated to be \$3.50 per mi, regardless of the volume required for the application.28 On-site production eliminates freight costs, and the H_2O_2 itself could be highly cost-competitive when produced in small-scale distributed facilities. For example, in a recent breakthrough in the area of distributed electrochemical H_2O_2

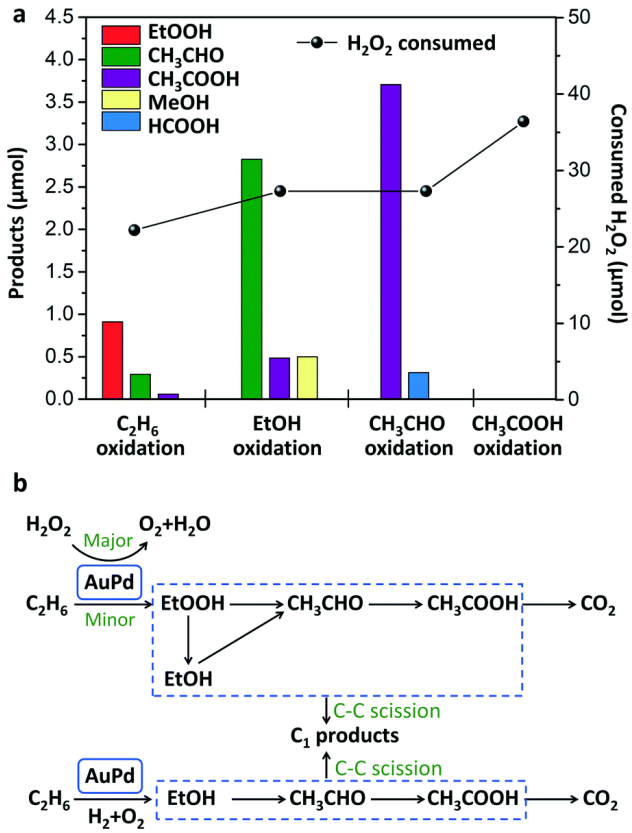

FIGURE 2.3. (a) Quantities of products and of H_2O_2 consumed for oxidation of C_2H_6, EtOH, CH_3CHO, and CH_3COOH over AuPd. Reaction conditions: 1 mg AuPd; 21 °C; 2 h; 50 μmol H_2O_2 (10 mM $[H_2O_2]_{initial}$); 1000 rpm. For C_2H_6 oxidation 1 bar C_2H_6 was used and for oxygenate oxidation 1 bar N_2 was used, with initial 10 μmol each of EtOH, CH_3CHO, or CH_3COOH (equivalent to 2 mM initial each). (b) Schematic of pathways deduced from results of reaction studies.

production, it was reported [**189**] that continuous streams of electrolyte-free H_2O_2 solutions, up to 20 wt%, could be produced. In that study, the cost of H_2O_2 was estimated to be \$0.07–0.15 per lb, depending on the anodic reaction employed in the system. [**189**]

Toward the goal of examining ethane oxidation in a distributed chemical manufacturing scenario where aqueous H_2O_2 is produced on-site at a continuous rate, additional experiments were conducted in a semi-batch configuration, wherein aqueous H_2O_2 is fed continuously during reaction. Results from the batch reactor studies shown above indicate that H_2O_2 is utilized most efficiently (highest gain factor) at low $[H_2O_2]_{initial}$. In the conditions of those experiments, 100% selectivity

to EtOOH was observed at initial H_2O_2 concentrations up to 10 mM. In the continuous-feed experiments, H_2O_2 was injected into the reactor through a gas-tight syringe pump at a concentration and rate that would maintain approximately 10 mM H_2O_2 throughout the experiment (based on the calculated average consumption rate of H_2O_2 from titration experiments and by adjusting the initial solvent volume). It is stressed that the real-time concentration of H_2O_2 in the reactor cannot be measured, and that no claim is made here that the steady-state concentration is exactly 10 mM. The experiment is intended to simulate generally the relevant scenario where a valuable oxidant is fed continuously and at low concentration.

In a typical continuous-feed semi-batch reactor experiment, dilute aqueous H_2O_2 solution was injected at a constant rate into the reactor for 50 h (details of these experiments are provided in the 2.2.5). Through this methodology, the oxidation of C_2H_6 at 1 bar headspace pressure was examined over Au, Pd, and AuPd catalysts (Fig. 2.4 a–c and Table 2.6). Under identical reaction conditions, reactor experiments with Au and Pd yielded 3.82 and 4.63 μmol of liquid oxygenates, respectively, whereas experiments with AuPd yielded 6.51 μmol oxygenates and therefore the highest H_2O_2 gain factor. It was observed that the distribution of products differed among the reactions with the three catalysts. Product distributions from C_2H_6 oxidation over Au were weighted toward less oxidized species (i.e. EtOOH/EtOH) whereas those from oxidation over Pd were weighted toward more oxidized species (i.e. CH_3COOH). In contrast, C_2H_6 oxidation over AuPd with 50 h continuous-H_2O_2-feed yielded a product distribution centered around a species resulting from an intermediate degree of oxidation (i.e. CH_3CHO). These observations are consistent with expectations – it is known that Pd is associated with strong binding of O-containing intermediates and Au is associated with comparably weak interaction with these species. The binding energy of O-containing species on AuPd surfaces is closer to optimum for reaction activity. That is, the binding energy exists at a peak of the volcano curve associated with the reactivity of these species according to the Sabatier principle. [**135**, **140**] It is logical therefore that Pd catalysts were observed to favor rapid decomposition of H_2O_2 and facilitate a greater degree of product oxidation. Use of Au catalysts is not expected to favor the formation and stable adsorption of *OH and/or *OOH, preventing high rates of C_2H_6 and oxygenate activation (here, * refers to adsorbed species). The higher total yield

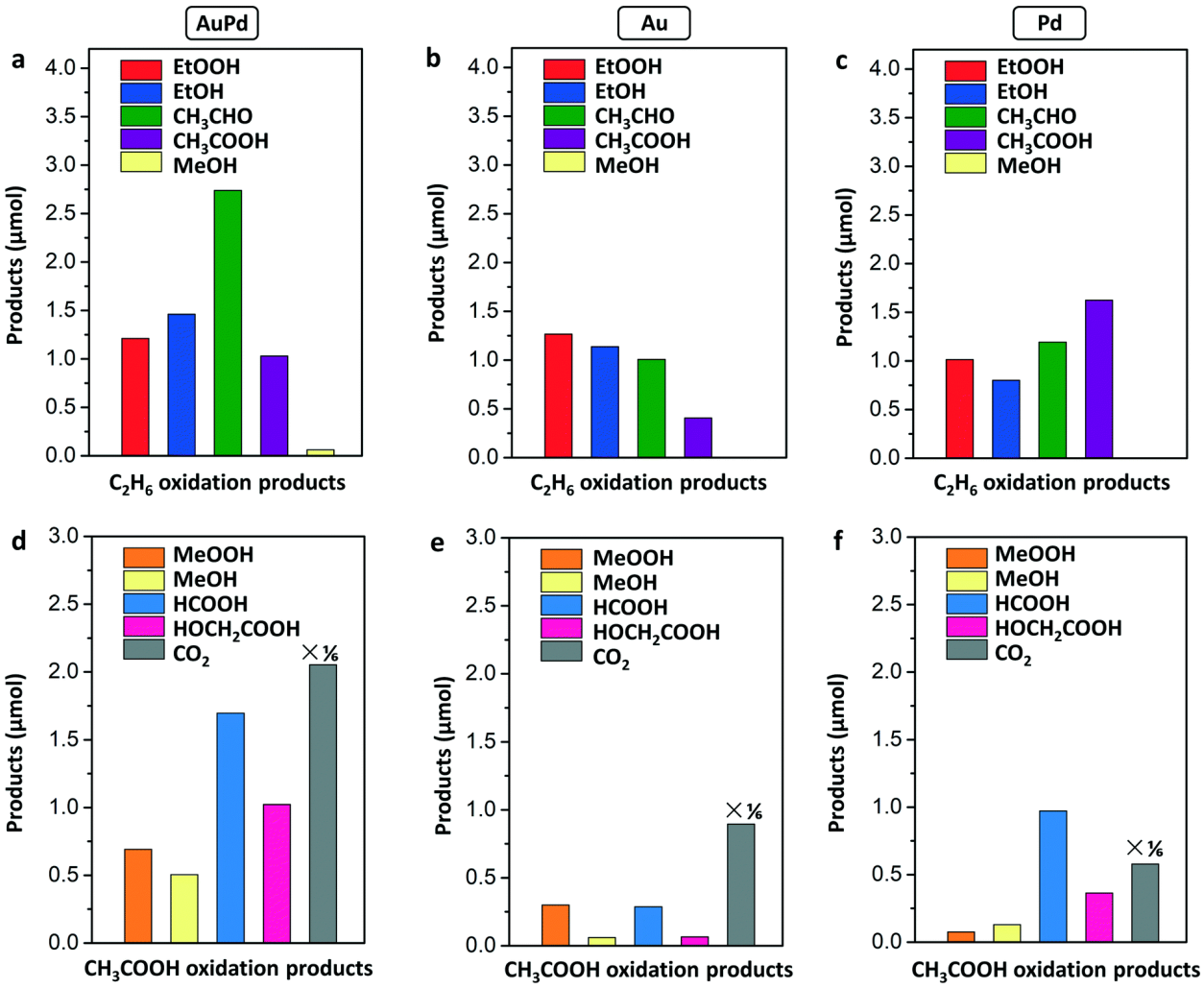

FIGURE 2.4. (a) (a–c) Products formed by C_2H_6 oxidation over AuPd, Au, and Pd catalysts for 50 h using the continuous-H_2O_2-feed configuration described in the main text. 1 bar C_2H_6 (d–f) CH_3COOH oxidation in the same system as (a–c). 500 μmol $[CH_3COOH]_{initial}$, 1 bar N_2. Reaction conditions: colloidal AuPd, Au, or Pd present with 6.6 μmol of metal; 21 °C; 50 h reaction time; 1000 rpm, 500 μmol H_2O_2 total injected over 50 h period.

of oxygenates over 50 h is consistent with the fact that AuPd is associated with an optimal *OH and/or *OOH binding energy for this reaction.

In the conditions of the batch reactor studies above, low $[H_2O_2]$initial resulted in 100% EtOOH-selective C_2H_6 oxidation over AuPd at reaction times on the order of 1 h. However, the H_2O_2-continuous-feed semi-batch studies indicate that even at low average steady-state H_2O_2 concentration, deeper oxygenate oxidations occur (Fig. 2.4 a). In these experiments, however, CO_2 was

only observed in the headspace in extremely small quantities (Fig. 2.10). This result suggested an attractive scenario could exist, wherein the most oxidized oxygenate product observed, CH_3COOH, could be stable in these catalytic conditions (room temperature and atmospheric pressure). Acetic acid, CH_3COOH, is an important compound for a number of industrial applications.

Given this interest, the oxidation of aqueous CH_3COOH in the presence of Au, Pd, and AuPd was directly investigated at higher initial concentration and in the milder oxidizing conditions associated with the continuous-H_2O_2-feed configuration. Figure 2.4 d–f and Table 2.6 provide quantified product distributions associated with this reaction with 100 mM initial CH_3COOH concentration (that is, the identical experiment whose results were reported in Figure 2.4 a–c for C_2H_6 oxidation, but with dissolved CH_3COOH as the reactant).

In these reaction conditions and in the presence of Au, Pd, or AuPd catalysts, CO_2 was found to be a prominent CH_3COOH oxidation product in the headspace. This indicates that when present in sufficient concentrations, CH_3COOH readily undergoes both C–H activation and C–C bond cleavage. CH_3COOH oxidation over AuPd yielded a greater overall quantity of products compared to Au and Pd, as was the case for C_2H_6 oxidation. It is clear from these results that in this reactor configuration (1 mg AuPd per 5 mL water), the combination of low temperature, low H_2O_2 concentration, and the stabilizing effect of water are insufficient to prevent overoxidation of oxygenates present in sufficiently high concentration. Specifically, at room temperature and with 100 mM initial concentration, reaction over AuPd yielded a CH_3COOH conversion of 3.25%.

The product quantities reported in Figure 2.4 for C_2H_6 oxidation and CH_3COOH oxidation are not directly comparable because the concentration of the reactants differed considerably. Given the general interest in a reaction system that produces C_2 oxygenates from C_2H_6, preliminary calculations using density functional theory (DFT) were performed to determine C-H activation of C_2H_6 and CH_3COOH. Previous studies have reported that $^{\cdot}OH$ or $^{\cdot}OOH$ obtained from the decomposition of H_2O_2 are the active species for the initial activation of these molecules. [**4**, **14**, **42**, **58**] Given these precedents, barriers were calculated for H abstraction from the molecules by *OH and by *OOH on the surface of AuPd (Fig. 2.11 and 2.12). The results, which represent a highly simplified first approximation of this reaction step, indicate H abstraction by *OH results in a lower barrier for both C_2H_6 and CH_3COOH. Recognizing that similar activation energies exist

for both molecules, it is necessary to design reaction systems capable of stabilizing the oxygenates and preventing overoxidation. [**141**]

More generally, these results show that at low concentrations, acetic acid is relatively unreactive even in this simple aqueous system (Fig. 2.3 a), and experiments are ongoing to determine the role of water in influencing reaction outcomes. The presence of water in similar catalytic systems – where both oxygenates and water bind to active sites through the oxygen atom – is known to effect the removal of adsorbed products, resulting in the accumulation of stable products in the solution. Encouraging results exist on this front – it has been reported that up to 0.5 M CH_3COOH produced by C_2H_6 oxidation can be stabilized in an aqueous system if H_2O_2 is produced concurrently (in tandem) at a slow and steady rate. [**102**]

2.2.4. Conclusions. This report has examined the aqueous partial oxidation of ethane over the surfaces of AuPd nanoparticle catalysts in mild conditions, with emphasis on outcomes for reactions occurring at 21 °C and 1 bar ethane (room temperature and atmospheric pressure). In these conditions, when H_2O_2 is used as an oxidant in a batch reactor, the maximum observed yield of oxygenates was 7707 μmol gAuPd^{-1} h^{-1}. It was observed that ethyl hydroperoxide, ethanol, acetaldehyde, acetic acid, and small quantities of C_1 products are generated from ethane oxidation over AuPd. Supplementary experiments were performed to elucidate the most probable reaction pathways operable for C_2 oxygenate generation and subsequent oxidation in this system. It was determined that ethyl hydroperoxide is the primary product resulting from the oxidative functionalization of ethane when H_2O_2 is used as the oxidant: it is produced with 100% selectivity at short reactions times and with low initial H_2O_2 concentrations. At longer times or in more oxidizing conditions (greater H_2O_2 concentration), ethyl hydroperoxide is subsequently oxidized to acetaldehyde, which can be further oxidized to acetic acid. Ethanol is observed as a product when H_2O_2 is used as oxidant, but results indicate it originates from the decomposition of ethyl hydroperoxide rather than from the direct product of ethane oxidation. Given these observations, and motivated by the prospect of distributed manufacturing of value-added chemicals from alkane feedstocks in mild conditions, this study also reported results simulating the utilization of H_2O_2 produced on-site at continuous rates. Through use of a pressure-tight semi-batch configuration with continuous dilute H_2O_2 feed, it was determined that H_2O_2 could be utilized much more efficiently

as an oxygenate-selective oxidant of ethane when low H_2O_2 concentrations are maintained for the duration of the reaction. The presented results indicate that aqueous catalytic ethane oxidation over unsupported AuPd produces a range of value-added C_2 products, but additional efforts are needed to stabilize these products from further oxidation. Given this need, a continuous process optimized for product stabilization could serve as the basis for effective distributed oxygenate synthesis in mild conditions from ethane.

2.2.5. Appendix. Catalyst Synthesis

AuPd nanoparticles were prepared through a modification of a method reported in the literature [**4**] 0.8775 mL $PdCl_2$ acidic solution (2 mg(Pd)/mL) and 1.625 mL $HAuCl_4$ solution (2 mg(Au)/mL) were added to a glass conical flask containing 207.2 mL deionized water. 1.65 mL of freshly prepared $NaBH_4$ aqueous solution (0.1 M) was injected into the solution under stirring (1000 rpm) as two 0.825 mL aliquots. The stirring speed of the produced dark brown colloidal suspension was kept at 1000 rpm for 30 minutes, and then the suspension was boiled vigorously (100 °C) under stirring (1000 rpm) until the suspension volume was between 20 and 25 mL. Of note, continuous stirring is critical to synthesize uniform colloids. After cooling down, the colloidal suspension was made up to 25 mL by adding deionized water. Finally, the as-prepared AuPd colloidal suspension (pH around 2.3) was stored in glass bottle. The suspension was sonicated uniformly prior to use. Au and Pd nanoparticles were prepared using similar processes as for AuPd. To maintain consistency across experiments, Pd nanoparticles were separated by centrifuge and dispersed in HCl aqueous solution (pH around 2.3) prior to use.

Catalyst Testing

A purpose-made PEEK reactor (see Figure 1.2), constructed from Swagelok fittings, was used for all experiments. The reactor has a total volume of 24.5 mL. A Teflon-coated K-type thermocouple was inserted into the reaction liquid to directly measure the reaction temperature. No metal components were in contact with the reaction liquid. For experiments with H_2O_2 oxidant, 5 mL of colloidal catalyst (1 mg AuPd) and a specific amount of H_2O_2 were added to the reactor. Prior to testing, PEEK reactor was sealed and purged with ethane (99.999%, Matheson) to remove air, and then the headspace of the reactor as represented in Figure 1.2 was pressurized with ethane to achieve the desired pressure, typically 1 bar. The total volume of the reactor is approximately

15 ml containing both liquid (∼5 ml) and gas (∼10 ml) volume in it. The reaction liquid was continuously stirred (1000 rpm) at room temperature (21 °C) using a magnetic stirrer for a specific period of time (usually 1 hour). For experiments at elevated temperatures, the reactor was heated and maintained at the desired reaction temperature. After the reaction, the reactor was cooled to a temperature below 15 °C in ice. The headspace gas was extracted using a gas-tight syringe for analysis. In a typical continuous-feed semi-batch reactor experiment, described in the main text to maintain a low and steady H_2O_2 concentration, catalysts and initial 30 μmol H_2O_2 (10 mM, 3 mL) were added to the reactor (initial 500 μmol acetic acid was added for the corresponding acetic acid oxidation reaction). Then the reactor was connected to a gas-tight syringe pump. Prior to testing, the reactor was purged with ethane (for the ethane oxidation reaction) or nitrogen (for the acetic acid oxidation reaction) for 15 mins. The reactor was then sealed and the pressure was steady at 1 bar. After 1 h of reaction, 470 μmol H_2O_2 in 2 mL of water was continuously added to the reactor by syringe pump during the following 49 h of reaction time.

Product Analysis

The gas phase products were analyzed by GC (Agilent GC7980) equipped with TCD and FID detectors (Helium as carrier gas). Residual H_2O_2 concentration was determined by titration with acidified $Ce(SO_4)_2$ solution using 8 μL ferroin indicator. [**37**, **183**] The liquid phase products were analyzed by 1H-NMR (Bruker 400 MHz NMR) using water suppression technique to decrease the dominant water signal. DMSO (1 mM) and phenol (8 mM) were used as internal standards. [**89**] Typically, 500 μL liquid product was mixed with 40 μL standards (DMSO and phenol) aqueous solution and 60 μL D_2O for the measurement. The measurements for ethanol, methanol, acetaldehyde, acetic acid, formic acid, and glycolic acid were calibrated from purchased standards following procedures reported in the literature (Fig. 2.6). [**89**] To quantify ethyl hydroperoxide, liquid solutions containing only ethyl hydroperoxide were reduced using prepared fresh 0.05 M $NaBH_4$ solution. After this, the reduced liquid products were analyzed by 1H-NMR. Considering that ethanol was the only reduction product, the amount of ethyl hydroperoxide was related directly to the total amount of ethanol. This procedure was robust and formed the basis of an ethyl hydroperoxide calibration curve (Fig. 2.6 b). Notably, considering both ethyl hydroperoxide and ethanol have three peaks located at around 1.07 ppm due to the signal of protons from C$\mathbf{H}_3$CH_2- in 1H NMR

spectrum, the areas of the peaks located at 3.96 ppm ($CH_3C\mathbf{H}_2$- of ethyl hydroperoxide) and 3.56 ppm ($CH_3C\mathbf{H}_2$- of ethanol) were calculated to quantify the amount of ethyl hydroperoxide and ethanol, respectively. Methyl hydroperoxide was quantified using analogous methods (Fig. 2.6 c).

Catalyst Characterization

X-ray diffraction (XRD) patterns were recorded on a Bruker D8 Advanced Diffractometer with Cu Kα radiation. X-ray photoelectron spectroscopy (XPS) data were collected on a Thermo ESCALAB 250Xi instrument equipped with a monochromatic Al Kα (1486.6 eV) source, and all XPS spectra were calibrated using C 1s peak at 284.8 eV as the reference. ICP-atomic emission spectroscopy (Agilent 725ES) was used for analysis Au/Pd molar ratio. Scanning electron microscopy (SEM) images and electron dispersive X-ray spectroscopy (EDXS) results were obtained on a JSM-5600 LV instrument. Scanning transmission electron microscopy (STEM) images were collected on a JEOL 2100-F-AC operated at 200 kV, and samples were prepared on copper grids coated with ultra-thin holey carbon films.

Computational Methods

Density Funcitonal Theory calculations (as implemented in the Vienna Ab-initio Simulation Package) [**55**] are used to study the C-H bond activation reaction. The AuPd(111) surface is modelled as a four-layer metal slab, consisting of a (4 x 4) fcc unit cells with 19 Å vacuum spacing between the periodic images. All calculations are performed using the RPBE functional [**57**] with Grimme's D3(BJ) [**51**] method to account for the dispersion interactions. The transition states are determined using the climbing-image nudged elastic band approach. [**63**] All calculations use a 400 eV plane-wave cutoff and (3 x 3 x 1) k-point grid. A force threshold of 0.03 eV/Å is used for the geometry optimizations.

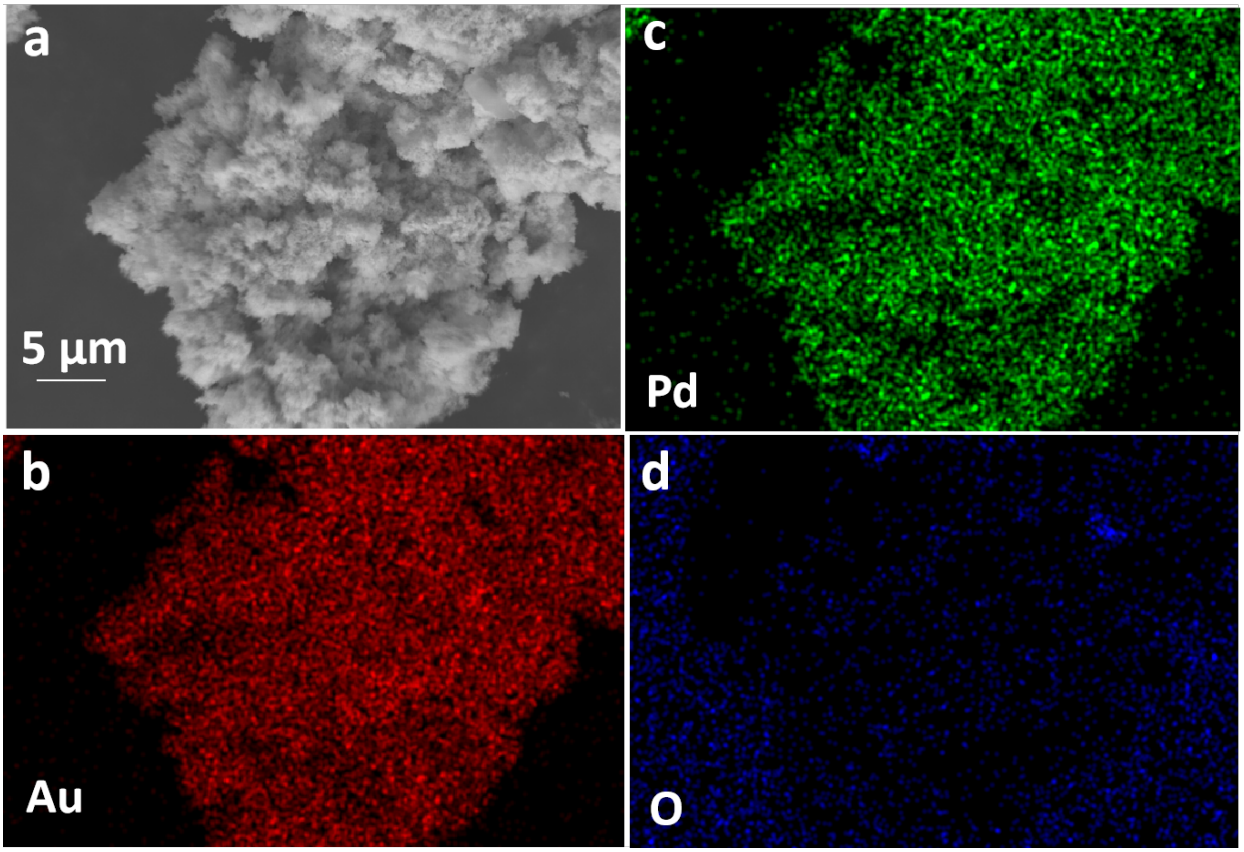

FIGURE 2.5. SEM-EDX elemental mapping of AuPd.

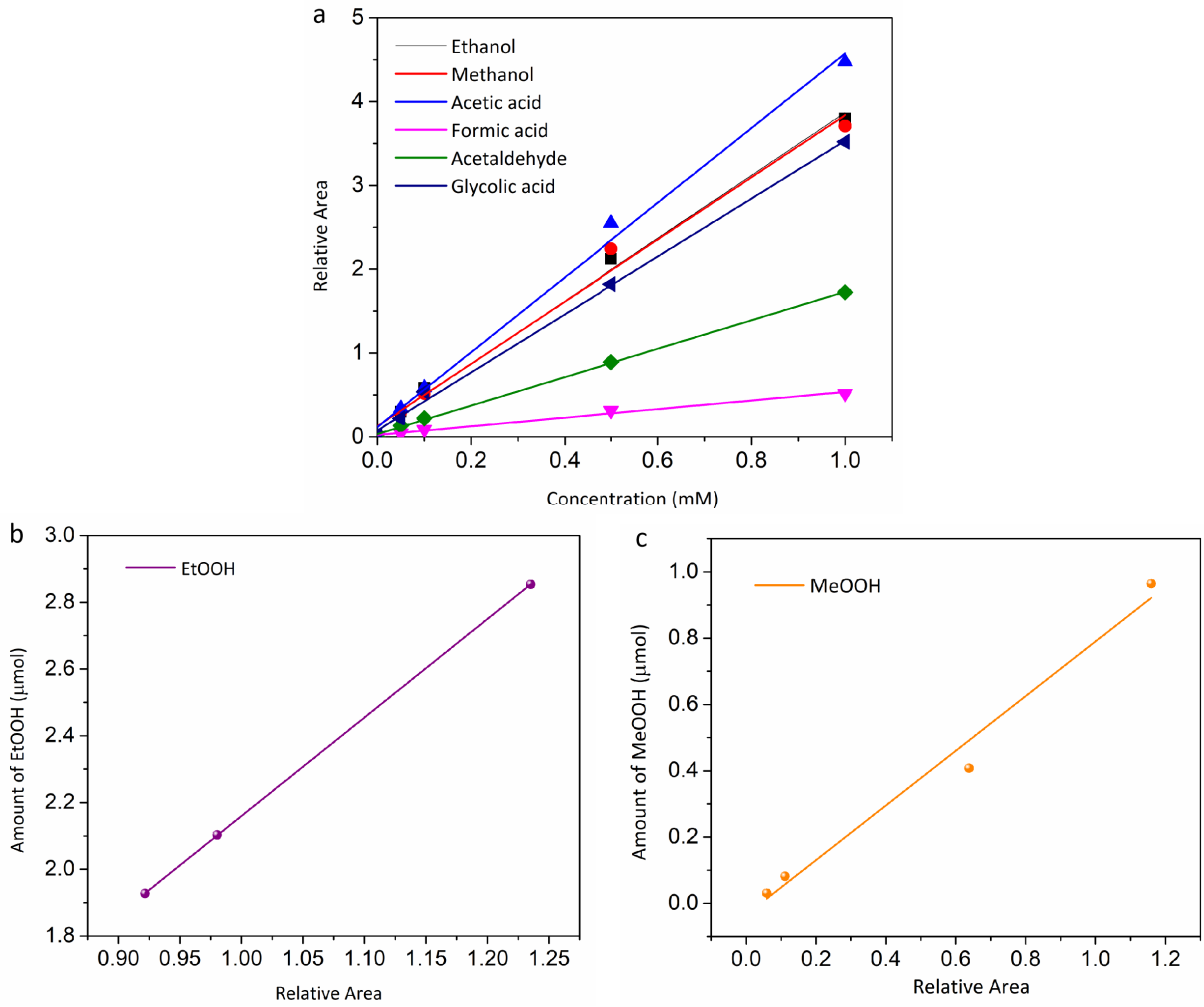

FIGURE 2.6. Standard calibration curves for products. (a) Ethanol, methanol, acetaldehyde, acetic acid, formic acid, glycolic acid; (b) ethyl hydroperoxide; (c) methyl hydroperoxide.

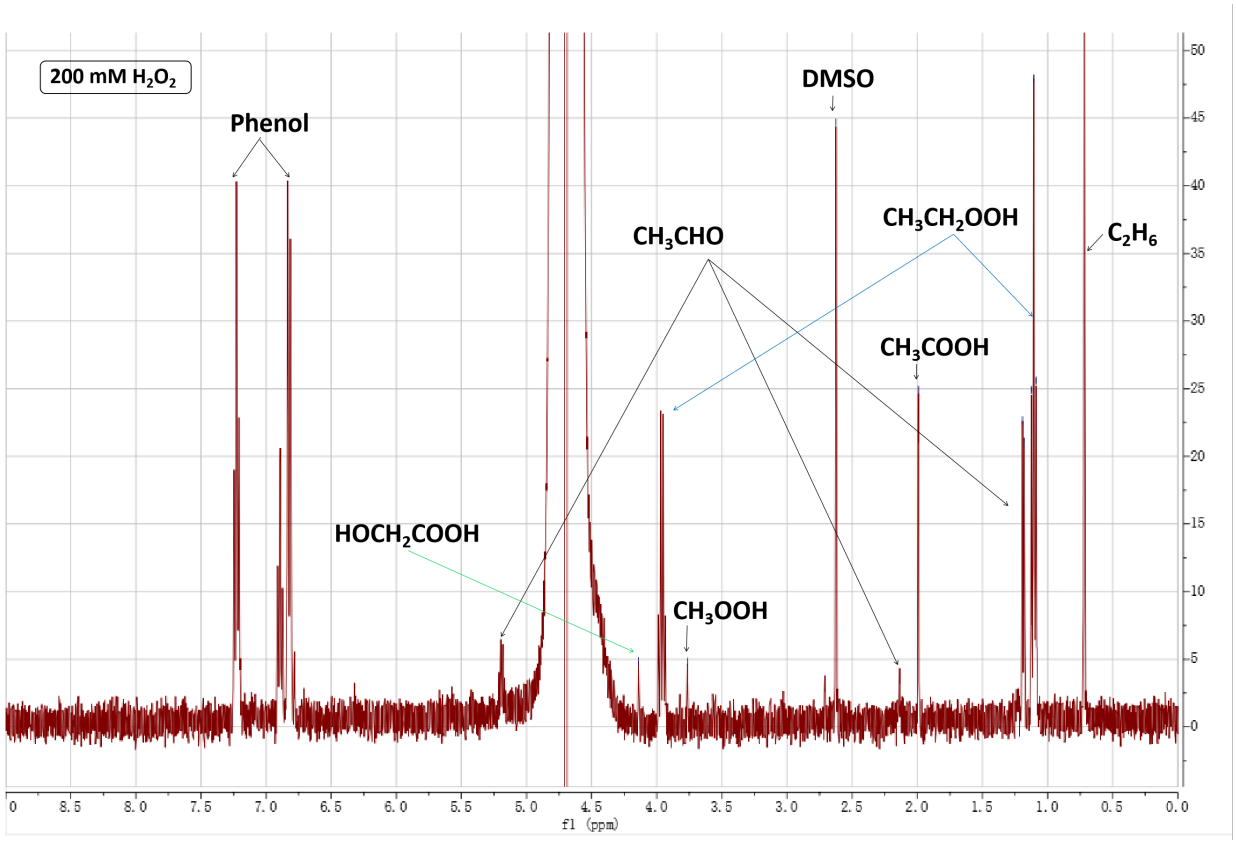

FIGURE 2.7. Typical 1H-NMR spectrum for liquid products. This spectrum corresponds to products of the oxidation of C_2H_6 using AuPd with $[H_2O_2]_{initial}$ = 200 mM. Reaction conditions: 5 mL; 1 mg AuPd; 1 bar C_2H_6; 21 °C; 1 h; 1000 rpm.

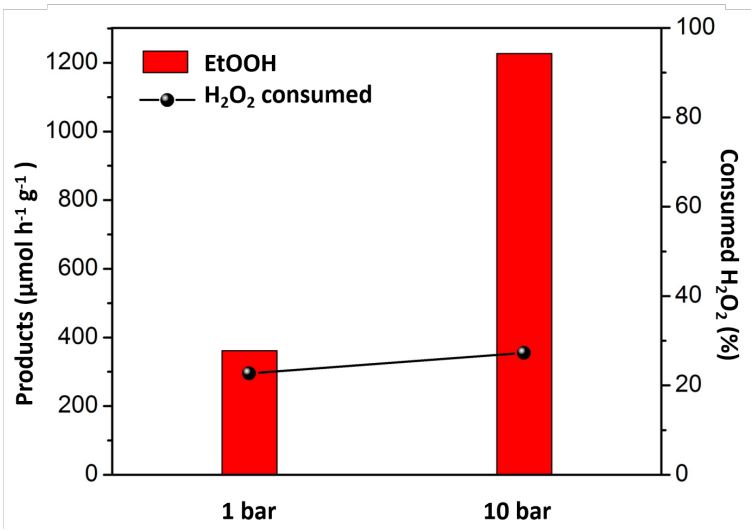

FIGURE 2.8. Comparison of catalytic activity of AuPd for C_2H_6 oxidation performed at 1 bar C_2H_6 (Gain factor = 0.0318) and 10 bar C_2H_6 (Gain factor = 0.0899). Gain factor is defined as mol oxygenates/mol H_2O_2 consumed. Reaction conditions: 5 mL; 1 mg AuPd; 1 bar or 10 bar C_2H_6; 21 °C; 1 h; 1000 rpm; $[H_2O_2]_{initial}$ = 10 mM.

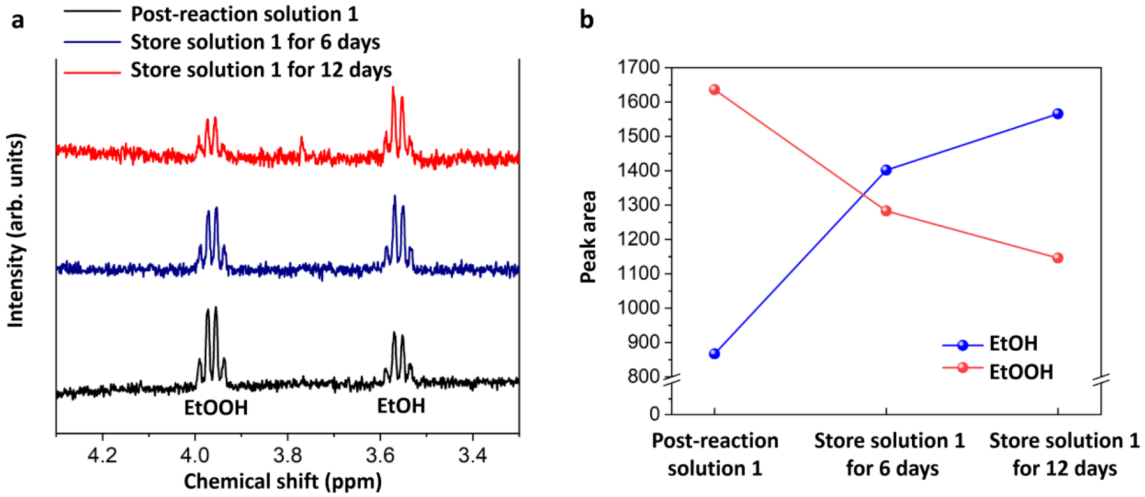

FIGURE 2.9. . (a) Typical 1H-NMR spectra for low concentrations of liquid products. Solution 1 results from C_2H_6 oxidation over AuPd at 50 °C with 100 mM $[H_2O_2]_{initial}$ for 1 h. (b) Normalized peak areas of EtOOH and EtOH associated with solution 1 after reaction and after storage of the solution for 6 and 12 days. The peak areas of products are normalized to peak area of the internal standard DMSO.

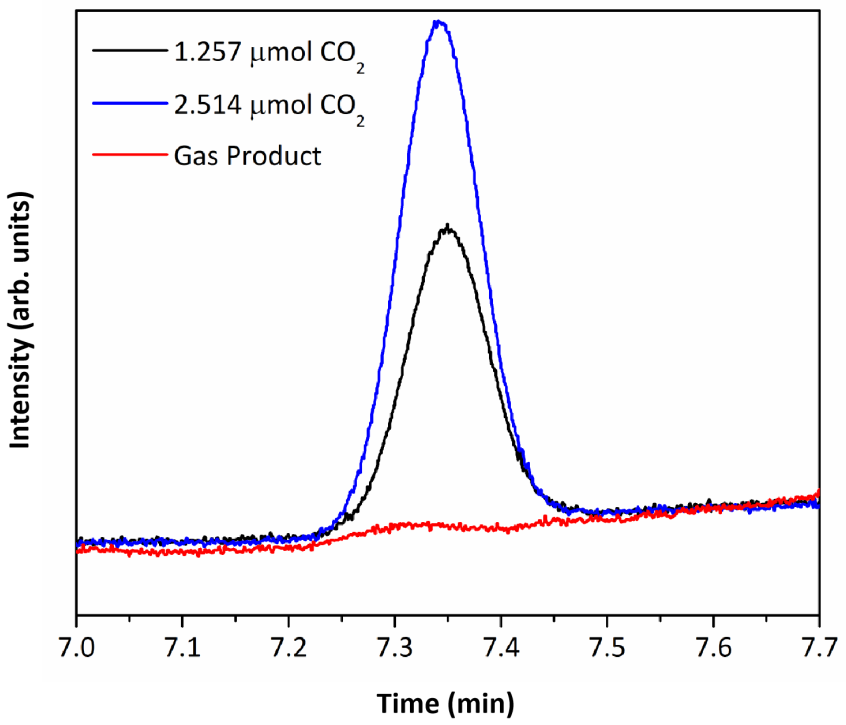

FIGURE 2.10. GC curve analyzing CO_2 in the gas phase after reaction over AuPd. CO_2 was nearly undetectable in the gas phase when compared with the calibration results for minute quantities of CO_2.

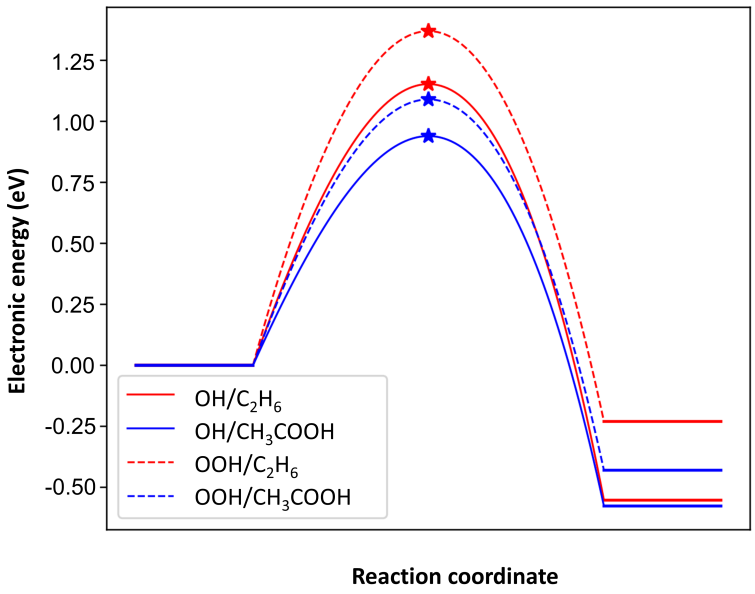

FIGURE 2.11. DFT calculations of activation barriers of C_2H_6 and CH_3COOH over AuPd surfaces.

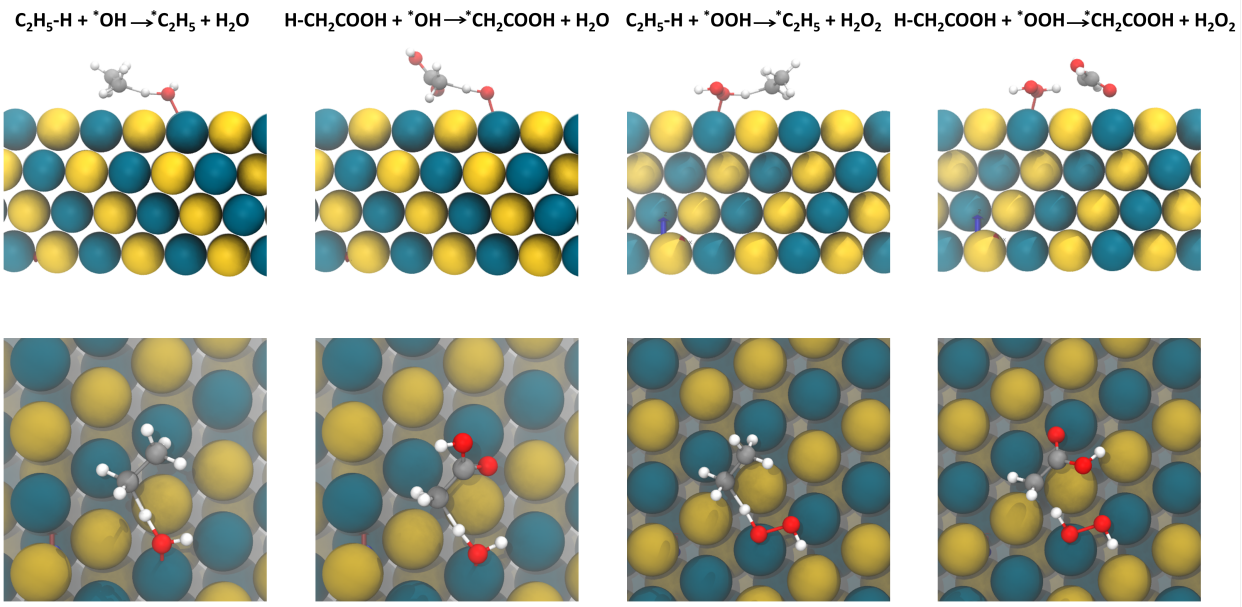

FIGURE 2.12. Front and top view for the structures of reaction intermediates and transition states (TS) involved in C_2H_6 and CHH_3COOH activation by *OH and *OOH, respectively, over AuPd surfaces. Yellow: Au; dark green: Pd; gray: C; white: H; red: O.

TABLE 2.1. Results of elemental analysis of AuPd.

EDX[a]

Elements	Unn.(ωt.%)	Norm.(ωt.%)	Atom (at.%)	Error (ωt.%)	ICP-AES (mg/L)[b]
O	1.60	2.25	18.07	0.4	n.d.
Pd	23.16	32.48	39.27	0.8	11
Au	46.56	65.28	42.65	1.8	21

XPS[c]

Elements	Au	Pd	C	O
Atom(at. %)	26.26	24.74	20.14	28.86

[a] The Au-Pd molar ratio is determined to be 1.086 by EDX analysis.

[b] The Au-Pd molar ratio is determined to be 1.027 by ICP-AES characterization. n.d. = not determined.

[c] The Au-Pd molar ratio is determined to be 1.061 by XPS analysis.

TABLE 2.2. Comparison of catalytic activity of Pd, Au and AuPd catalysts for ethane oxidation and acetic acid oxidation in semi-batch continuous-H_2O_2-feed reactions.[a]

Catalyst	Reaction conditions[a]	Initial H_2O_2 Concentration	Reference
AuPd	21 °C and 1 bar	0.001-0.5 M; *In situ* production[b]	This work
Fe and Cu containing ZSM-5	50 °C and 5-30 bar	0.1-1 M	*J. Am. Chem. Soc.*, 2013, **135**, 11087-11099
Fe/ZSM-5	30-60 °C and 20 bar; 50 °C and 1-30 bar	0.06-0.3 M	*J. Catal.*, 2015, **330**, 84–92
Fe/ZSM-5	30 °C and 5 bar	0.5 M or 1 M	*Chem. Sci.*, 2014, **5**, 3603–3616
H/ZSM-5	77-120 °C and 30-35.5 bar	0.1-0.4 M	*Appl. Catal. A: General*, 2013,**456**, 82–87
Rh_1O_5/ZSM-5	50-80 °C and 15 bar;50 °C and 1.5-15 bar	0.5-2.5 M	*ACS Sustainable Chem. Eng.*, 2019, **7**, 4707-4715
TS-1	60 °C and 30 bar	0.116 M	*Tetrahedron Lett.*, 2006, **47**, 3071–3075
Pd/C	70-110 °C and 34.5 bar	*In situ* production	*J. Am. Chem. Soc.*, 1992, **114**, 7308–7310
$(FePc)_2N/SiO_2$; $(FePctBu)_2N/SiO_2$	60 °C and 32 bar	0.339 M	*J. Organomet. Chem.*, 2015, **793**, 139–144

[a] Reaction temperature and initial ethane pressure.

[b] H_2O_2 generated *In situ*.

TABLE 2.3. Additional experiments for comparison with AuPd nanoparticle catalysts.[a]

Entry	Catalyst	H_2O_2 amount (μmol)	EtOOH	CH_3CHO	CH_3COOH	O_2 produced (μmol)	Total liquid products (μmol)	H_2O_2 consumed (%)
1	$PdCl_2/HAuCl_4$	50	0	0	0	0	0	0
2	AuPd	50	0.43	0	0	2.54	0.43	22.2

[a] Reaction conditions: 1 bar C_2H_6; 21 °C; 1 h; 1000 rpm.

[b] Entry 1: Homogeneous metal chloride precursor solutions (3.3 μmol of $PdCl_2$ and 3.3 μmol of $HAuCl_4$ in 5 mL of water).

[c] Entry 2: 5 mL; 1 mg AuPd (6.6 μmol of metals).

TABLE 2.4. Comparison of catalytic activity of AuPd catalyst for C_2H_6 oxidation.[a]

Entry	Oxidant	H_2O_2 concentration (mM)	Reaction time	O_2 produced (μmol)[c]	Total liquid products (μmol)	H_2O_2 consumed	Gain factor (%)[d]
1	H_2O_2	0	1	0	0	0	0
2	H_2O_2	1	1	n.d.	0.15	2.9	0.0525
3	H_2O_2	10	1	2.54	0.43	11.1	0.0383
4	H_2O_2	30	1	13.27	0.94	95.1	0.0098
5	H_2O_2	100	1	68.55	2.87	318.2	0.0090
6	H_2O_2	200	1	172.19	7.71	663.6	0.0116
7	H_2O_2	500	1	319.45	1.22	1609	0.0008
8	H_2O_2	10	2	5.65	1.26	22.2	0.0569
9	H_2O_2	10	4	5.99	2.06	33.3	0.0619
10	H_2O_2	10	8	10.51	2.83	43.3	0.0654
11[b]	H_2/O_2	n.d.	1	n.d.	4.32	n.d.[e]	n.d.

[a] Typical reaction conditions: 5 mL; 1 mg AuPd; 1 bar C_2H_6 for entries 1 to 10; 21 °C; 1000 rpm. For all entries, CO_2 in the gas phase is in trace amounts (¡1 μmol) and could not be quantified by GC-TCD.

[b] $P_{H2} = 0.1$ bar, $P_{N2} = 0.9$ bar, $P_{C2H6} = 1$ bar, $P_{O2} = 0.4$ bar.

[c] The amount of O_2 was determined by GC.

[d] Gain factor is defined as mol of total amount of oxygenates/mol of H_2O_2 consumed.

[e] After reaction, 3.4 μmol H_2O_2 left. n.d.=not determined.

TABLE 2.5. Product quantification for C_2H_6 oxidation over AuPd at 50 °C.[a]

Catalyst	H_2O_2 concentration (mM)	EtOOH	EtOH	CH_3CHO	CH_3COOH	O_2 produced (μmol)	Total liquid products (μmol)	H_2O_2 consumed (μmol)
AuPd	100	2.29	1.13	1.31	0.16	178	4.89	440
AuPd	200	3.00	0.91	2.09	0.29	274	6.29	800
AuPd	500	0.64	0.20	0.57	0.15	792	1.56	2140

[a] Reaction conditions: 5 mL; 1 mg AuPd; 2 bar C_2H_6; 50 °C; 1 h reaction time; 1000 rpm.

TABLE 2.6. Comparison of catalytic activity of Pd, Au and AuPd catalysts for ethane oxidation and acetic acid oxidation in semi-batch continuous-H_2O_2-feed reactions.[a]

Entry	Catalyst	Reactant[b]	Coversion (%)	CO_2 produced (μmol)	Total liquid products (μmol)	H_2O_2 consumed (μmol)	Gain Factor[c]
1	Pd	CH_3COOH	1.00	3.47	1.54	460	n.d.
2	Au	CH_3COOH	1.22	5.37	0.71	180	n.d.
3	AuPd	CH_3COOH	3.25	12.32	3.91	450	n.d.
4	Pd	C_2H_6	0.58	n.d.[f]	4.63	468	0.0099
5	Au	C_2H_6	0.48	n.d.	3.82	400	0.0096
6	AuPd	C_2H_6	0.82	n.d.	6.51	420	0.0155

[a] Reaction conditions: Pd, Au, or AuPd colloid (6.6 μmol of metals); 1 bar N_2 for entries 1 to 3, and 1 bar C_2H_6 for entries 4 to 6; 21 °C; 50 h; 1000 rpm; 500 μmol H_2O_2.

[b] 500 μmol CH_3COOH (100 mM) or 1 bar C_2H_6 (795 μmol) as reactant.

[c] Conversion = (mol of total amount of oxygenates + mol of CO_2 produced)/mol of reactant in the reactor.

[d] The amount of CO_2 produced was determined by GC.

[e] Gain factor is defined as mol of total amount of oxygenates/mol of H_2O_2 consumed.

[f] For entries 4 to 6, CO_2 in the gas phase is in trace amounts (¡1 μmol) and can not be quantified by GC-FID. n.d. = not determined.

CHAPTER 3

Electrocatalysis for light alkane upgrading*

Chapter 3.2 is partially adapted from a published work:

Y.L. Wang, S.M. Gurses, N. Felvey, A. Boubnov, S.S. Mao, C.X. Kronawitter*; In situ deposition of Pd during oxygen reduction yields highly selective and active electrocatalysts for direct H_2O_2 production, *ACS Catal.*, 2019, **9**, 8453-8463.

Reproduced with permission from *ACS Catal.*, 2019, **9**, 8453-8463.

&

Chapter 3.3 is fully adapted from a published work:

S. M. Gurses, C.X. Kronawitter; Electrochemistry of the Interaction of Methane with Platinum at Room Temperature Investigated through Operando FTIR Spectroscopy and Voltammetry *J. Phys. Chem. C*, 2021, **125**, 2944-2955.

Reproduced with permission from *J. Phys. Chem. C*, 2021, **125**, 2944-2955.

This work was funded by American Chemical Society Petroleum Research Fund (ACS PRF).

*The content of this chapter has previously been published in Ref. [**52**, **178**].

3.1. Overview of the chapter 3

As it is mentioned in the Chapter 1, this chapter investigates the electrochemical methods for the oxidation of light hydrocarbons. Chapter 2 portrayed the liquid-phase thermal methods by testing unsupported catalyst in a slurry with H_2O_2 as an oxidant. Although encouraging results were obtained from such system, an alternative way was needed for an effective conversion due to the high-cost of the oxidant (H_2O_2). Chapter 2 also simulated a semi-batch process by devising the delivery of H_2O_2 from an on-site production facility and suggested that the continuous flow of low concentrated H_2O_2 would facilitate the selective conversion for a long period of time. Therefore, Chapter 3.2 initially describes a newly-designed electrocatalyst might serve as a way to produce H_2O_2 continuously and sustainably which would later be fed into the semi-batch reactor as described above. At the same time, we aimed to understand the fundamentals of the interaction of light hydrocarbons, methane in this case, with a catalyst surface in an electrochemical cell. For this purpose, polycrystalline Pt was selected as the test catalyst and operando FTIR measurement coupled with cyclic voltammetry experiments was performed to gain mechanistic information into activation of C-H bond. Owing to these efforts, we managed to obtain promising results, which we believe contributed to the related research community, and tune our system for the ultimate goal of coupling light alkane utilization with H_2O_2 generated electrochemically. Accordingly, we have designed different reactors as briefly described in the Appendix 1.3 of Chapter 1. Further experiments were performed to replace the thermal energy input with electricity by utilizing the reactor illustrated in Figure 1.3. Our preliminary results were included in the Appendix 3.4 of this chapter. It should be noted that we also performed experiments on partial oxidation of methane with *in-situ* produced H_2O_2 over the same catalyst surface in a hybrid reactor (Figure 1.4). However, we were not yet able to observe any significant conversion of methane under mild conditions.

3.2. In situ deposition of Pd during oxygen reduction yields highly selective and active electrocatalysts for direct H_2O_2 production

3.2.1. Abstract. Hydrogen peroxide (H_2O_2) is a commodity chemical that serves as an oxidant and disinfectant for a number of historically important chemical end-use applications. Its synthesis can be made more sustainable, clean, and geographically distributed through technology enabled by the aqueous electrocatalytic two-electron reduction of O_2, which produces H_2O_2 using only air, water, and electricity as inputs. Herein results are presented establishing that Pd, which is widely known to catalyze the four-electron reduction of O_2 to H_2O, can be made highly selective toward H_2O_2 production when it is deposited in situ—that is, through electrochemical deposition from Pd ions during O_2 reduction. The resultant cathodes are found to be comprised of sub-5 nm amorphous Pd nanoparticles and are measured to facilitate H_2O_2 selectivities above 95% in the relevant potential range. In addition, the cathodes are highly active—they are associated with the second-highest partial kinetic current density for H_2O_2 production in acidic media reported in the known literature. It is observed that in situ synthesis of Pd catalysts enables dramatic gains in H_2O_2 yield for all inert, conductive supports studied (including glassy carbon, commercial activated carbon, graphene, and antimony-doped tin oxide). Further efforts to generalize these results to other systems establish that even Pt, the prototypical four-electron O_2 reduction catalyst, can be engineered to be highly selective to H_2O_2 when it is synthesized in situ under relevant conditions. These results and the comprehensive electrochemical and physical characterization presented, including synchrotron-based X-ray absorption spectroscopy, suggest that in situ synthesis is a promising approach to engineer O_2 reduction electrocatalysts with tunable product selectivity and activity.

3.2.2. Highlighted results. In this study, Pd was deposited by reduction of aqueous dissolved $PdCl_2$ at various concentrations during simultaneous reduction of O_2 onto a number of electrically conductive and electrochemically inert supports/substrates. For all results reported, prior to deposition, the ORR activities and selectivities of all bare supports/substrates were measured in O_2-saturated 0.1 M $HClO_4$ solution to ensure that the substrate (blank) electrode yielded no ORR activity. H_2O_2 generation was quantified during in situ deposition through rotating ring

disk electrochemistry (RRDE). In the RRDE configuration, the Pt ring potential was held potentiostatically at 1.28 V vs RHE, a potential where H_2O_2 is fully oxidized and the process is mass transport limited. [**135**] After deposition, the samples were removed from the $PdCl_2$-containing 0.1 M $HClO_4$ electrolyte and placed directly into pure 0.1 M $HClO_4$ for evaluation of ORR activity using RRDE.

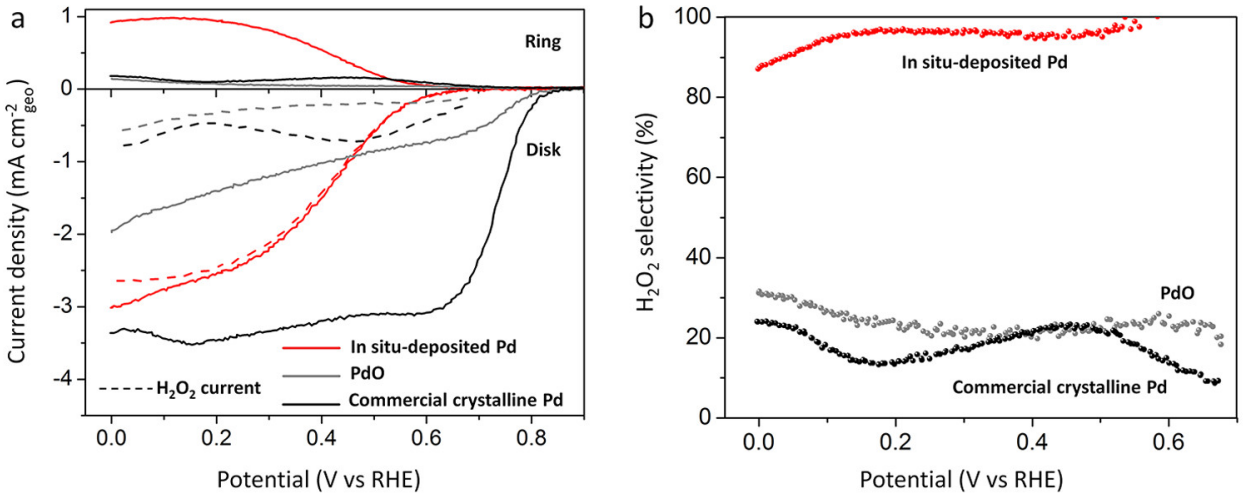

FIGURE 3.1. RRDE ORR results in pure 0.1 M $HClO_4$. (a) Linear sweep voltammograms of a representative in situ-deposited Pd sample (Pd 1.0 μM), PdO, and commercial crystalline Pd/C. (b) H_2O_2 selectivity calculated from the Pt ring current in (a). Conditions: 0.1 M $HClO_4$; 10 mV s^{-1}; 1600 rpm; Pt ring held at 1.28 V vs RHE for H_2O_2 detection.

Figure 3.1 shows, through linear sweep voltammograms in the RRDE configuration, the performance of a representative in situ-deposited Pd electrocatalyst for O_2 reduction. As has been observed previously in the literature, [**134**, **135**] the results show that Pd/C (crystalline Pd) primarily facilitates the four-electron reduction of O_2 to H_2O. It is associated with low activity for H_2O_2 production; the potential-averaged selectivity was 17.8%, and the highest selectivity recorded over the potential range of interest was 24%. PdO shows activity similar to that of Pd/C, yielding a potential-averaged selectivity of 22.6% and at high overpotential a maximum H_2O_2 selectivity of 32%. In contrast, the in situ-deposited Pd electrocatalyst yielded ORR activity with extremely high H_2O_2 selectivity—greater than 90% for the entire potential range of interest, with a potential-averaged selectivity of 95.1%. Nearly 100% selectivity was observed at low overpotential (at 0.55

V vs RHE, or 0.13 V overpotential with respect to $E_{O_2/H_2O_2}{}^0 = 0.68$ V). In addition, the in situ-deposited Pd electrocatalyst is highly active-it yields the second-highest reported kinetic current density for H_2O_2 production under acidic conditions.

3.3. Electrochemistry of the interaction of methane with platinum at room temperature investigated through operando FTIR spectroscopy and voltammetry

3.3.1. Abstract. Electrochemical processes show potential to enable new catalytic technologies that facilitate the conversion of light alkanes in more mild conditions than those traditionally employed in thermochemical reactions. Motivated by the prospect of these emerging technologies, this study investigates the aqueous electrochemistry of methane with Pt electrodes at room temperature and atmospheric pressure. The experimental approach is designed to elucidate the composition of surface-adsorbed C–H–O– containing molecular fragments resulting from the (electro)chemical interaction of methane and water with polycrystalline Pt surfaces. A combination of operando FTIR spectroscopy (surface-enhanced infrared absorption spectroscopy) and anodic stripping voltammetry techniques is employed. The influences of Pt polarization and the system bulk pH are assessed. In addition, the surface chemistry of the interaction of methane with Pt electrodes is contrasted with that of carbon monoxide and carbon dioxide interactions that produce similar surface-bound species but are associated with differing spectroscopic and voltammetric characteristics. Through analysis of experimental outcomes in the context of the comprehensive literature that exists on these related electrocatalytic systems, several insights into the aqueous surface chemistry of the methane–Pt interaction are generated. It is found that sites on the surface associated with reduced local Pt coordination, especially those at step edges, comprise the most likely rection centers for methane activation and decomposition to surface-bound C–H fragments. These fragments interact with surface-bound oxygen-containing species also likely generated at surface defect sites whose presence results from the interaction of water with the Pt surface and the composition of which is dependent on electrochemical potential and pH. These findings indicate that future studies on this system should emphasize developing a deeper understanding of the exact

nature of reaction centers on electrode surfaces, which will help guide electrochemical engineering efforts intended to enable the controlled oxidation of methane.

3.3.2. Introduction. Mechanistic details of processes involving C-H bond activation and functionalization are among the most persistent core interests of the catalysis research community. [**8**, **13**, **83**, **93**] The recent increase in availability of hydrocarbon feedstocks from shale gas resources has led to resurgent interest in new avenues for functionalization of the aliphatic C-H bonds of light alkanes. [**115**] In addition to the clear economic interest in increased natural gas utilization for chemical synthesis, environmental arguments have also been made to support the need for new conversion technologies: the hydrocarbon constituents of natural gas are more effective greenhouse gases than CO_2. [**29**] Consequently, natural gas obtained during oil extraction from remote reservoirs is flared to convert hydrocarbons to CO_2 before release. [**115**] A unique opportunity therefore exists for development of new techniques that enable the direct conversion of light alkanes in mild conditions. The ability to operate in mild conditions is expected to be a valued characteristic of any new catalytic technology that is designed to operate at reduced scale and at geographically distributed sites. Methane (CH_4) is the most abundant component of natural gas and while it is a valued resource for electricity generation in gas-fired power plants, it is particularly under-utilized as a chemical feedstock. Selective CH_4 partial oxidation to value-added chemicals is difficult to achieve at high conversions due to the inertness and uniformity of its C-H single bonds. In traditional thermal catalytic reactions, the high temperatures required to activate CH_4 result in deep oxidations to CO_x – products whose formation are thermodynamically favored over oxygenates. Electrochemical processes show potential to overcome this challenge because they facilitate greater precision in establishing operating conditions that optimize activity and selectivity in milder conditions. Aqueous electrocatalysis is widely used for chemical synthesis, especially in the context of renewal energy storage in the form of chemical bonds. [**49**] Recent studies have demonstrated that the generation of a diverse variety of oxygenates is possible through anodic electrocatalytic CH_4 conversion in aqueous electrolytes. [**81**, **110**, **129**] In order to engineer systems that enable the controlled electrocatalytic oxidation of CH_4, a more comprehensive understanding of the chemistry of CH_4 on simple, prototypical electrocatalyst surfaces is needed. Methane oxidation at mild temperature and pressure has been intensely studied for applications involving polymer electrolyte fuel

cells (PEFC). [**70**,**127**] To obtain information regarding electrocatalyst surface chemistry (often the chemistry of hydrocarbons on dispersed Pt particles), it is common for this application to analyze adsorbates through anodic stripping voltammetry. In a typical voltammetry sequence designed to probe adsorbates, the anode is held at a constant potential for a period of time, which results in an adlayer of reaction fragments. The presence of adsorbed species and often their interaction with the surface can be probed with a subsequent anodic scan that strips the adsorbates in an oxidative electrochemical reaction. These studies have shown that light hydrocarbons can be readily dehydrogenated and partially oxygenated while the electrode potential is held and the resulting fragments can be partially or fully oxidized in the anodic stripping event. [**70**, **133**] In aqueous conditions, other characterization techniques have been used to evaluate the chemistry of CH_4 on electrocatalyst surfaces, including operando FTIR [**56**] and computational approaches. [**8**] A wealth of information exists in the literature on the thermochemical steps of alkane dehydrogenation over Pt catalysts, [**82**,**149**] which also occur in electrochemical reactions, providing critical fundamental information toward understanding the surface chemistry of this system. Recently Jaramillo and coworkers [**22**] examined the interaction of CH_4 with Pt surfaces in aqueous electrolytes through a combination of anodic stripping voltammetry, calculations using Density Functional Theory, and kinetic modeling. In that study it was found that thermochemical CH_4 activation is the rate-determining step on Pt electrodes at room temperature and that $*CH_x$ (throughout this study, * denotes a surface-bound species) interact with adsorbed or near-surface water to generate *CO. [**22**] In this study, we provide new contributions toward understanding the (electro)chemistry of CH_4 at Pt electrode surfaces at room temperature. We report results from time- and potential-dependent attenuated total reflection surface-enhanced infrared absorption spectroscopy (ATR-SEIRAS) measurements in operando conditions to directly probe the chemical nature of surface-bound species resulting from the interaction of CH_4 with Pt. Findings from this approach are supplemented by systematic voltammetry experiments that examine the influence of electrode potential and pH on the generation of C-H-O-containing surface fragments from CH_4 and H_2O. Results from these approaches are interpreted through a comprehensive examination of available literature on this subject.

3.3.3. Experimental procedures. *Platinized Pt electrode preparation.* Electrochemical measurements were conducted in a standard three-electrode cell (Figure 3.16) with a platinized Pt coil working electrode, a silver-silver chloride (Ag/AgCl) reference electrode, and a graphite rod counter electrode that was separated from the main solution in a vial with a fine glass frit. The Pt coil was platinized via pulse electrodeposition [**22**] in a solution containing 10 mM potassium hexachloroplatinate (IV) ($\geq$ 99.9%, K_2PtCl_6, Sigma-Aldrich) in 0.1 M $HClO_4$ (70%, $HClO_4$, Sigma-Aldrich). The working electrode was held galvanostatically at -10 mA cm^{-2}, then at open circuit potential (OCP) (1 s reduction followed by 6 s at OCP). This process was repeated 100 times to generate a high-surface-area electrode. Platinized Pt was generated by cycling 100 times from 0 V to 1.6 V vs the RHE with scan rate 200 mV s^{-1} in 0.1 M $HClO_4$. After cycling, the electrochemically active surface area was determined from the hydrogen adsorption charge of 210 μC cm^{-2} assumed for monolayer adsorption of hydrogen. Scanning electron microscopy (SEM, The Thermo Fisher Quattro S) and cyclic voltammetry were used to characterize the surface of the electrode after platinization.

SEIRAS-active Pt electrode preparation. The SEIRAS-active Pt electrode was obtained by layer by layer deposition on hemi-cylindrical Si prism via electroless Au deposition followed by electrodeposition of Pt. The Si prism was polished with alumina slurries to obtain a mirror-like finish (the final alumina polish slurry contained 1 μm particles). The prism was then sonicated sequentially in acetone and water for 10 min each. Au nanoparticle films were deposited at 60 °C by introducing to the surface a gold plating solution using a micropipette. The plating solution was prepared as described elsewhere. [**9**] The resulting Au film was cleaned and activated by cycling 3 times from 0 V to 1.4 V RHE at 50 mV s^{-1} in 0.1 M $HClO_4$ before Pt was deposited. Galvanostatic deposition of Pt was performed at 400 μA for 600 s with a plating solution consisting of 4 mM K_2PtCl_6 and 0.7 M Na_2HPO_4. The Pt film obtained from this procedure was then cycled between 0 and 1 V vs RHE at 50 mV s^{-1} in a fresh electrolyte until stable steady-state cyclic voltammograms with the well-defined hydrogen adsorption and desorption features characteristic of Pt were obtained.

FTIR spectroscopy. FTIR spectroscopy measurements were performed with a Bruker VERTEX 70 FTIR spectrometer equipped with a liquid nitrogen cooled MCT detector. The instrument was operated at a resolution of 4 cm^{-1} with different acquisition times (depending on the measurement).

Spectra associated with the ATR-SEIRAS configuration were acquired with a VeeMax III ATR accessory (Pike Technologies) set to an incidence angle of 60°. All the spectra in this study are shown in absorbance units defined as -log (I/I0), where I and I0 represent the intensities of the reflected radiation at the sample and reference potentials, respectively. The roughness factor of Pt was approximately 5, obtained by assuming 210 μC cm^{-2} for monolayer adsorption of hydrogen. [**119**, **147**]

Methane, carbon monoxide, and carbon dioxide voltammetry

Voltammetry experiments were performed with platinized Pt as prepared above. The electrochemical cell sparged with N_2 for 1 h before saturating the solution with the reactant gases. Anodic stripping voltammetry was performed through a programmed sequence involving potentiostatic hold as indicated in the main text followed, without pause, by an anodic scan to 1.4 V vs RHE at 50 mV s^{-1} and a subsequent cyclic voltammogram to ensure all adsorbed species were absent. To quantify the charge accumulated in the oxidative stripping events, the integrated peak areas were divided by scan rate and were corrected by subtracting the charge obtained by an identical experiment in a N_2-saturated electrolyte, following convention. [**22**] The adsorbate coverages associated with the interaction of CH_4 with Pt are found to be small and assumed to not shift Pt oxidation features associated with the reaction with H_2O. When KOH electrolytes were utilized, they were first treated with a chelating agent (Chelex).

3.3.4. Results and discussion. Platinized platinum was used as the working electrode for all voltammetry investigations in this study. Its surface morphology was characterized by SEM (Figure 3.2a); the high degree of surface roughness evident in the SEM image is consistent with that expected for platinized Pt. Figure 3.81 provides a typical cyclic voltammogram (CV) recorded in N_2-purged 0.1 M $HClO_4$, which indicates the characteristic features of Pt CVs expected in these conditions. In anodic stripping voltammetry experiments, CH_4 was first allowed to interact with Pt under potentiostatic control, and adsorbed species originating from this interaction were then oxidized during an anodic sweep (Figure 3.2b). In the representative experiment whose results are shown in Figure 3.2b, the Pt electrode was held at 0.3 V vs RHE for 1 h, and the potential was then immediately swept anodically at a rate of 50 mV s^{-1}. In this case, the electro-oxidation of adsorbed species results in a positive current at ca. 0.7 V vs RHE. In this study, the charge

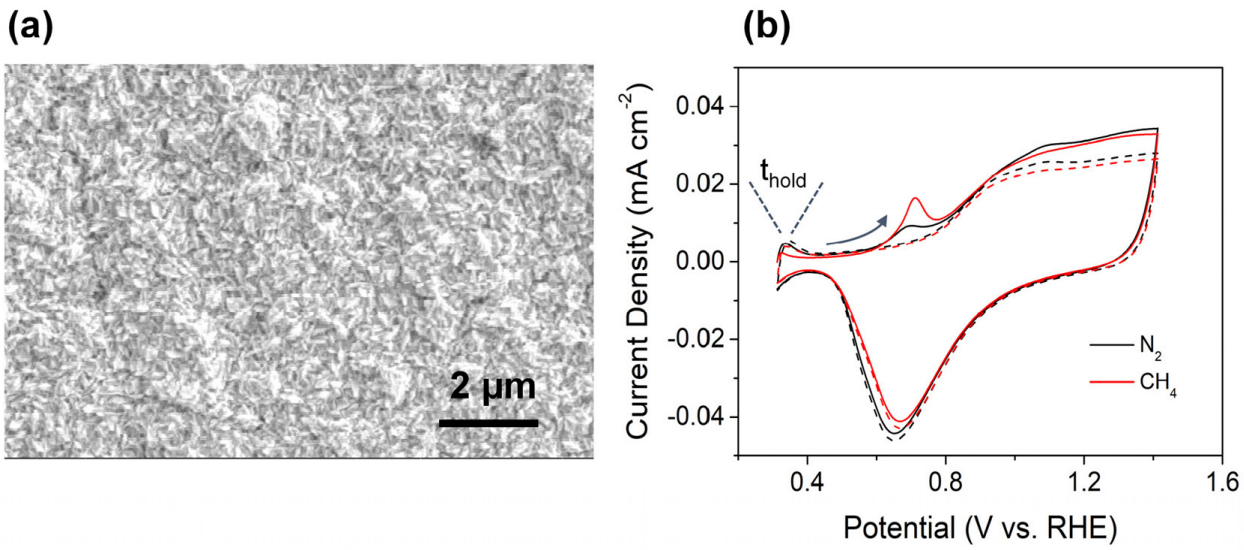

FIGURE 3.2. (a) SEM image of the platinized Pt electrode surface used for voltammetry investigations. (b) Representative results from application of the anodic stripping voltammetry procedure, corresponding to a 1 h hold at 0.3 V vs RHE followed by a 50 mV s^{-1} CV beginning with the anodic scan direction.

calculated from stripping peaks results from oxidation of adsorbed species that originate from the (electro)chemical interaction of CH_4 with the Pt surface. When charge associated with this reaction is reported, the background charge (obtained from identical potential-hold experiments in N_2-saturated electrolytes) is subtracted, following convention. [**22**] The background current associated with execution of this procedure in the inert-saturated electrolyte, which is absent from steady-state CVs, has been observed previously; its origins have been investigated in the context of possible carbon contamination. [**22**] The process of subtracting charge resulting from identical voltammetry procedures in inert-saturated electrolytes, in contrast to subtraction of data from a steady-state CV, is the most conservative approach available to isolate and assess charge associated with the reaction of CH_4.

Using this methodology, we investigated the chemical interaction of CH_4 with Pt and the subsequent anodic oxidation of the resulting adsorbed species at a fixed potential (0.3 V vs RHE) as a function of holding time (Figure 3.3). Figure 3.3a shows a magnified view of the irreversible oxidative stripping feature in a series of independent experiments wherein the Pt potential was held for durations between 1 and 60 min. The total charge associated with these stripping peaks as a function of holding time is provided in Figure 3.3b. These results show that the increase

in amount of charge decreases with longer holding times (i.e., the rate of increase decreases with time). However, the charge determined by anodic stripping voltammetry (Figure 3.3a,b) provides no information about the chemical nature of adsorbed species whose oxidation generates this charge in the external circuit.

To assess the nature of the chemical species, a spectroscopic technique must be applied. To this end, SEIRAS measurements, which provide the vibrational spectra associated with adsorbed species, [**119**, **163**] were recorded with Pt electrodes (Figure 3.3c). To match the conditions of the stripping experiments, the potential was held at 0.3 V vs RHE while simultaneously recording FTIR spectra. Spectra recorded at 10 min intervals during a 60 min hold are shown in the bottom of Figure 3.3c. The most distinct feature is the band at 2013 cm^{-1}, which is readily assigned to the stretching mode of surface-bound CO (ν(CO)) and is found to result directly from the chemical interaction of CH_4 with the Pt surface in the presence of water. Because of the low reactivity of CH_4, the signal intensities are weak relative to those commonly obtained in direct CO adsorption studies; despite this, the peaks are sufficiently resolved to facilitate analysis. Figure 3.3d provides the integrated intensities of the ν(CO) peak as a function of time held at 0.3 V vs RHE. These results show that when Pt is held at 0.3 V vs RHE in CH_4-saturated solution, *CO accumulates quickly on the surface in the first several minutes of applied potential and then coverage increases more gradually at longer times, consistent with the system approaching a saturation coverage.

Simultaneous consideration of Figures 3.3b and 3.3d indicates that the line shapes of the time dependences of the two independent measures of adsorption (charge from anodic stripping and FTIR integrated peak area) are consistent. This is true despite the fact that the two Pt working electrodes were required to be prepared differently. (This is obligatory given the special requirements for generation of SEIRAS-active Pt films [**163**] for operando FTIR; see the Experimental Procedures 3.3.3.)

Figure 3.4 provides outcomes from additional analyses of the SEIRAS results. Figure 3.4a shows a magnification of the time-dependent *CO peaks and Gaussian fits to their line shapes. By use of these fits, the center energies and FWHM of the peaks were determined and plotted as a function of time (Figure 3.4b). Although clearly attributable to the C–O stretching mode of Pt–CO, the observed frequency differs slightly from that of Pt–CO species obtained through other

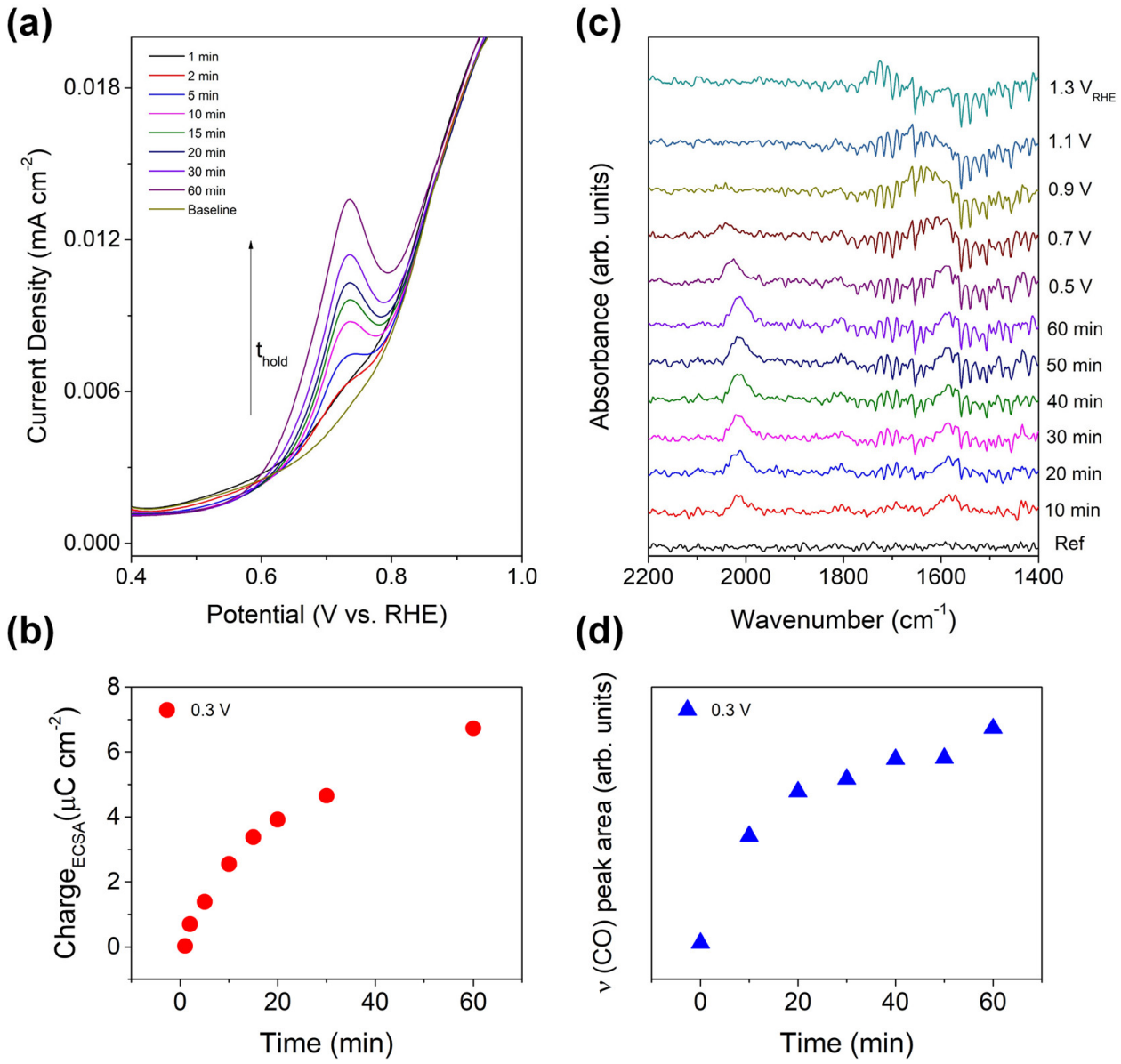

FIGURE 3.3. (a) Magnification of the oxidative stripping feature present in the anodic scans following potential holds between 1 and 60 min in CH_4-saturated electrolytes. (b) Time dependence of the charge density associated with the oxidative stripping feature in (a). (c) ATR-SEIRAS spectra of the Pt surface during CH_4 purging with potential held at 0.3 V vs RHE for 1 h followed by anodic scan to 1.3 V vs RHE (50 mV s^{-1}). (d) Integrated intensity of the ν(CO) peak centered near 2013 cm^{-1} as a function of holding time at 0.3 V vs RHE (0.1 M $HClO_4$, 1 atm of CH_4).

reactions. Specifically, linearly bonded *CO (*CO_L) on Pt surfaces is typically observed in the range 2050–2085 cm^{-1}. [**19**, **119**, **147**, **152**, **158**] To confirm that the shifted energy of this peak is not an artifact of our experimental setup, we performed SEIRAS studies at the Pt electrodes during the electroreduction of CO_2 (Figure 3.9). The electroreduction of CO_2 at the surfaces of Pt has been comprehensively examined; [**65**, **67**, **69**, **77**, **158**] the spectral signatures of the adsorbed species resulting from CO_2 reduction therefore provide a valuable benchmark for the experimental system. Pt–CO_L modes resulting from CO_2 reduction are observed at 2042 cm^{-1}, which is consistent with results in the literature for this species. [**67**, **158**]

Energy shifts among CO bands have been extensively discussed in the literature. [**32**, **60**, **79**, **80**, **90**, **148**, **180**, **191**] Early surface science investigations of Pt single crystals in ultrahigh vacuum (UHV) have attributed the observed differences in peak position to *CO adsorbed on different surface sites. [**60**, **61**, **191**] For instance, Hayden et al. investigated the adsorption of CO on Pt(553) by infrared reflection–adsorption spectroscopy (IRAS) and found that *CO at step sites is associated with a significantly lower wavenumber than *CO adsorbed on terrace sites. [**60**] Later studies on single crystal surfaces in electrochemical environments supported the results obtained by UHV studies. [**79**, **80**, **180**] Recently, in a study of methanol and ethanol electro-oxidation, Farias et al. observed a significant red-shift in the *CO_L band associated CO adsorbed on steps compared with that adsorbed on both terraces and steps. [**41**] CO band shifts and splitting were also observed during electro-oxidation of methanol on polycrystalline Pt surfaces. [**32**] Specifically, multiple distinct *CO_L bands centered at energies much greater than those associated with *CO_B were observed. The *CO_L peak centered at the lower wavenumber was assigned to linear *CO adsorbed on kinks or edge sites. [**32**] Lebedeva et al. investigated mechanisms of CO adlayer oxidation on Pt(553), Pt(554), and Pt(111) surfaces, and the results indicated that CO initially preferentially adsorbs at sites located on steps. [**96**] The recent findings over Pt(110) have also revealed that the potential required to strip off the CO adlayer is lower specifically for the CO bonded on the steps. [**41**] Sato et al. performed CO adsorption and oxidation experiments on highly dispersed Pt catalysts and concluded that the lower energies associated with ν(CO) that were observed at low *CO coverages resulted from the preferential adsorption of *CO at sites with reduced local Pt coordination. [**148**] Given these precedents and the observed low energy of the *CO_L band in Figure 3.4 (2013 cm^{-1}),

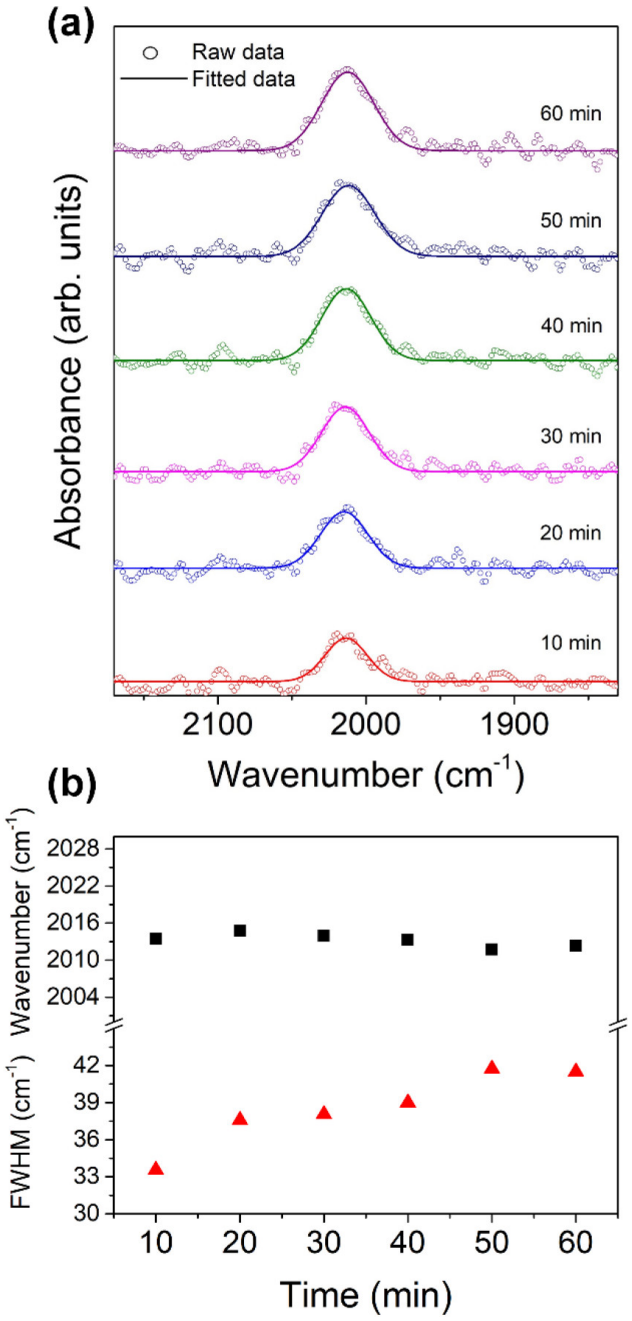

FIGURE 3.4. Time-dependent operando SEIRAS results with potential held at 0.3 V vs RHE for 1 h in CH_4-saturated 0.1 M $HClO_4$ (magnification of data in Figure 3.3c). (a) Gaussian fits to line shapes of CO peaks. (b) CO peak position and FWHM plotted with respect to time.

the results lead to the conclusion that the adsorbed species resulting from interaction with aqueous methane at 0.3 V vs RHE is *CO bound to Pt at step-edges or defects ($*CO_{L(edge)}$), which are expected to be abundant on the polycrystalline Pt surface. Similarly, the weak band at 1805 cm^{-1}, which is evident through magnification in Figure 3.10, has been attributed to bridge-bonded *CO ($*CO_{B(edge)}$) on the step-edge or defect sites. [**90**, **148**] This conclusion is consistent with the commonly observed intrinsically high catalytic activity of steps on Pt surfaces [**95**, **96**, **194**] as well as a number of studies that highlight the importance of steps, corners, and other sites with reduced local Pt coordination on the adsorption behavior of CH_4. [**46**, **54**, **131**, **142**, **175**, **198**] In a notable recent study specifically assessing the interaction of CH_4 with stepped Pt surfaces, Gutiérrez-González et al. showed that $*CH_3$ generation is much faster when dissociation occurs at step sites than when it occurs at terrace sites. [**54**] Both experimental and theoretical approaches were used to determine that dissociation barriers were lowest at step sites. [**54**] It is noteworthy that this study also considered that CH_4 could be initially activated at steps; we hypothesize later in this article that $*CH_x$ species resulting from CH_4 activation at step sites subsequently interact with oxygen-containing species also present at these sites, generating *CO. Although the high CH_4 activation barrier on terraces suggests step sites with reduced Pt coordination are the primary active sites, [**22**, **25**] we note that previous studies have shown that Pt terrace sites also activate CH_4. [**54**, **109**, **131**] The distinction among these activation pathways may be difficult to assess in steady-state experimental studies: the diffusion of $*CH_3$ from terraces to steps has been observed at low coverages. [**131**]

The characteristics of the $*CO_L$ peak provided in Figure 3.4 can also be interpreted in the context of prior operando FTIR spectroscopy studies of CO electro-oxidation at Pt electrodes. Blue-shifts in *CO absorption bands are typically explained by increased dipole–dipole coupling between adjacent *CO. [**64**, **174**, **192**] As the *CO adlayer is oxidized at anodic potentials, red-shifts are commonly observed, which can be attributed to the loss of these dipole moments. [**64**, **147**, **148**, **174**, **192**] The data in Figure 3.4 indicate that while holding at 0.3 V vs RHE, as time increases the ν(CO) band energy is stable while the peak FWHM increases. Prior literature has indicated that dipole–dipole coupling between adjacent *CO additionally results in decreased FWHM. [**192**] This indicates that although the coverage of *CO increases with time toward saturation in the CH_4/Pt system (Figure 3.3d), no significant dipole–dipole interactions are observed, as would be

expected for *CO saturation on Pt terraces. [**64**, **174**, **192**] Taken together, the SEIRAS results, interpreted through the prior literature of this and related systems, suggest that step-edge or defect sites, which are abundant on rough, polycrystalline Pt surfaces, are the dominant active sites for the (electro)chemical decomposition/oxidation of CH_4 observed in this study.

In addition to those associated with C-O stretching modes, weak absorption bands centered at 1695 cm^{-1} were detected (Figure 3.10a). The development of this band (which is distinct from the δ(HOH) band that is often present in the same spectral region in aqueous systems and which will be discussed further below) has previously been assigned to the stretching mode of the carbonyl group (C=O) of *CHO or *COOH. [**56**,**100**,**132**,**163**] It has been reported that *COOH is also associated with bands at 1300 and 1500 cm^{-1}, which are due to OH deformation in *COOH. [**69**, **154**, **201**] Results from infrared reflection–absorption spectroscopy (IRAS), which through dipole selection rules selectively detects modes oriented perpendicular to surfaces, indicate that the adsorption of carboxylic acid species on Pt yields a peak near 1750 cm^{-1} that is associated with the stretching mode of C=O in the carboxyl group. [**162**,**163**] A prior study of ethanol oxidation over Pt provides complementary information: the stretching mode of the carbonyl group in aldehyde components is present at lower vibrational frequencies than the carbonyl stretching modes of carboxylic acids. [**132**] Similarly, it has been reported that the stretching mode of carbonyl groups in formyl-like species exists near 1700 cm^{-1}. [**17**,**18**] Therefore, in the context of this prior literature, the absence of a vibrational feature associated with OH deformation and the relatively lower frequency of the detected band (1695 cm^{-1}) most likely indicate the additional presence of *CHO. [**15**,**17**,**18**,**75**,**105**] This observation also agrees well with previous studies that demonstrate that *CH is the most abundant and relatively stable *CH_x species resulting from CH_4 activation over step sites of Pt surfaces and that low-energy barriers exist for formation of *CHO and *CO. [**109**, **175**, **198**]

The SEIRAS absorbance results reported above were obtained with background scans collected at 0.3 V vs RHE, which is near the cathodic side of the double-layer regime. In acidic media, the surface state of Pt is traditionally understood to be metallic in this region. Additional experiments were performed with a background signal obtained at 1.1 V vs RHE, which is more anodic than the potential required for surface oxidation of Pt. Spectra were recorded at various potentials during a sweep in the cathodic direction. The resultant spectra (Figure 3.10b) indicate the clear presence

of a negative band at 1729 cm^{-1} that emerges at ~0.5 V vs RHE. The vibrational frequency of this observed feature is close to that reported for the carbonyl stretching mode within a surface carboxylic group (*COOH), as discussed above, [**100**, **132**, **162**] which differs from the *CHO-like feature obtained from the spectra recorded during anodic scans. Observation of *COOH could be rationalized by the contrasting initial state of Pt in this case: at 1.1 V vs RHE, a high coverage of *O/*OH exists. Methane's interaction with the Pt surface in this state could generate the more oxidized *COOH species, which is unstable at more cathodic potentials where it is observed to disappear. These SEIRAS measurements provide valuable information about the nature of adsorbed species associated with electrochemical CH_4 activation. However, more definitive conclusions regarding the surface chemistry of the CH_4/Pt system could potentially be made with additional data from supplementary techniques. In the following section, results from complementary voltammetry experiments are provided to further elucidate the nature of the interaction of $*CH_x$ with oxygen-containing species on the surface.

Prior investigations have shown that rates of CH_4 decomposition and oxidation at Pt surfaces are strongly dependent on applied potential [**22**,**70**,**126**,**127**,**170**] as well as the associated coverages of *H, *OH, and *O, which originate from the aqueous electrolyte. [**22**, **139**, **170**] To provide a new perspective on this observation, CO and CO_2, whose interactions with Pt are also well-known to be potential-dependent, were examined as reactants in addition to CH_4. Figure 3.5 provides anodic stripping features associated with the interaction of these molecules with the Pt surface at three different initial holding potentials.

Previous studies have shown the necessity of adsorbed hydrogen for electrocatalytic CO_2 reduction over Pt. [**23**, **65**, **157**, **158**] This prior result is confirmed in this study; the greatest amount of charge is obtained by oxidation of surface-bound species after holding the Pt electrode at 0.1 V vs RHE (Figure 3.11). This potential lies within the range associated with underpotential hydrogen adsorption (below ca. 0.35 V vs RHE). The magnitude of charge resulting from anodic stripping decreases at more anodic holding potentials, consistent with the role of adsorbed H in activating CO_2 over Pt.

The potential dependences of anodic stripping charge resulting from the CO/Pt and CH_4/Pt systems differ considerably from that of CO_2/Pt. Results in Figure 3.5 indicate that after a potential

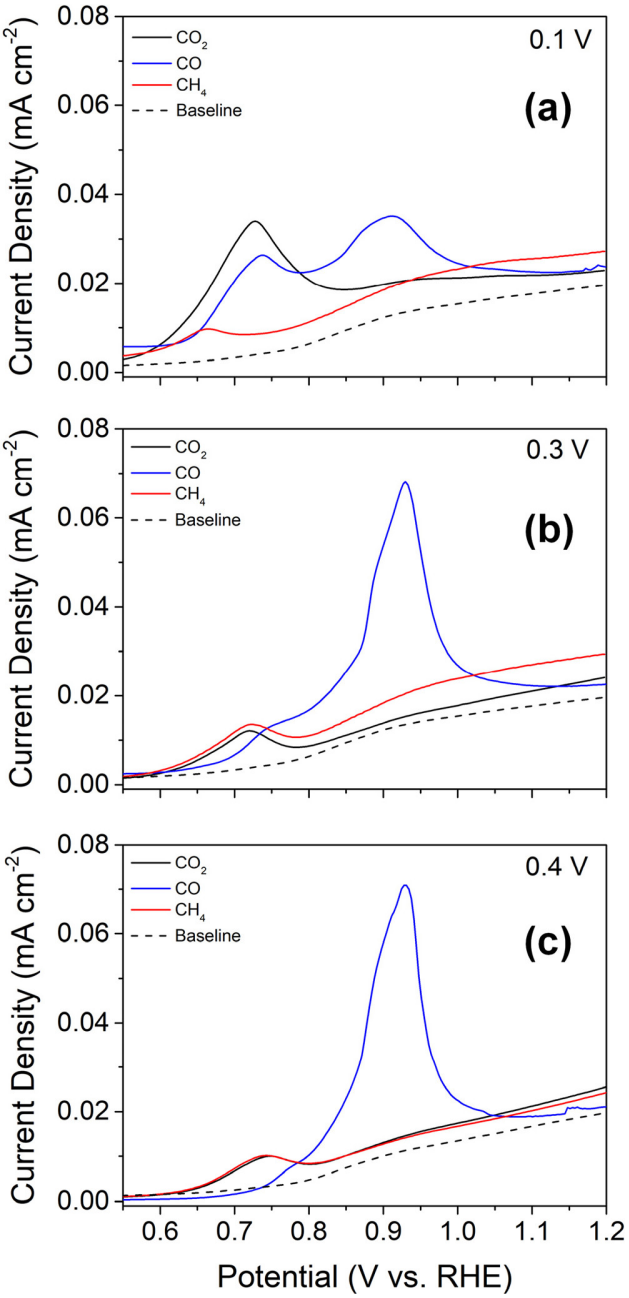

FIGURE 3.5. Oxidative stripping features associated with the interactions of CH_4, CO, and CO_2 with Pt after holding for 1 h at (a) 0.1 V vs RHE, (b) 0.3 V vs RHE, and (c) 0.4 V vs RHE (50 mV s^{-1}; 0.1 M $HClO_4$; 1 atm of CH_4, CO, or CO_2).

hold in a CO-saturated electrolyte the anodic sweep yields two oxidative stripping peaks, which are most pronounced after holds at 0.1 and 0.3 V vs RHE. These peaks are commonly termed the prepeak and main peak in the electrochemical CO oxidation literature and their origins have been

discussed extensively. [**50**,**96**,**106**,**147**,**192**] Figure 3.5 and Figure 3.15 show that the CO oxidation main peak is split into two peaks in these conditions. The splitting of the main peak has previously been attributed to the removal of *CO adsorbed on different facets of polycrystalline Pt, and the peak at less anodic potential was specifically assigned to *CO adsorbed on Pt(100) surfaces. [**35**] The data in Figure 3.5 indicate that the anodic stripping peak associated with the CH_4/Pt system begins near 0.7 V vs RHE, which is close to that of *CO oxidation over Pt(100). The similarity between these oxidation potentials suggests that perhaps the local chemical environment around *CO is similar for the two systems. This agrees well with previous observations indicating the high intrinsic activity of Pt(100) for electrochemical CH_4 oxidation. [**109**] The nature of the CO electro-oxidation prepeak (in the literature and Figure 3.5) could be helpful to further understand the electrochemical behavior of the CH_4/Pt system—especially results associated with the interaction of CH_4 with Pt at low holding potentials. Therefore, it is useful to briefly review the origins of the observed features in CO oxidation voltammograms.

Lebedeva et al. demonstrated that the potential for *CO adlayer oxidation is lower when greater step densities are present due to the lower *CO packing density possible on stepped surfaces. [**96**] Later, similar results were observed over Pt(111) that was air-cooled and found to possess larger amounts of crystalline defects. [**97**] Subsequently, Housmans et al. developed a model for mechanistic investigations of CO oxidation, results from which showed that the prepeak could be attributed to interaction of *OH on the step sites with adjacent *CO. [**66**] As was the case for the above interpretation of the CH_4–Pt interaction in the context of available FTIR literature, the CO electro-oxidation literature highlights the importance of step sites for anodic oxidation of *CO. Because the CO electro-oxidation prepeak has been interpreted to involve the coincident presence of *OH and *CO at steps, and its mechanism is potentially similar to that for oxidation of CH_4-derived *CO, this first notable aspect of the electro-oxidation results is consistent with the claim that step sites play a critical role in the activation of CH_4.

The potential dependence of the magnitude of the anodic stripping event (the charge passed) differs between the CO/Pt and CH_4/Pt systems. While the charge passed in the lower potential feature of the stripping main peak in the CO/Pt system is larger at the lower holding potentials examined (especially within the hydrogen underpotential deposition region ($H_{(upd)}$)), for CH_4/Pt

the largest stripping charge was obtained after holding at 0.3 V vs RHE. This can be explained by the fact that in a CO-saturated electrolyte CO adsorption is favored over hydrogen adsorption [**106**] (that is, the discharge of protons at the surface to form Pt–H). In contrast, within the $H_{(upd)}$ region, hydrogen adsorption is favored over CH_4 decomposition/oxidation. [**22**]

For all gases examined, the results in Figure 3.5 indicate a clear distinction in outcomes exists between stripping after potential holds within the $H_{(upd)}$ regime and holds within the double-layer region. To probe this observation further, the potential and holding-time dependence of the CH_4/Pt system were examined in greater depth. Figure 3.6 reports the time dependence of the oxidative stripping charge after holding times from 1 to 120 min. Interestingly, these results show the highest rates of reaction with CH_4 occur at 0.3 V vs RHE, with 0.4 and 0.5 V vs RHE yielding similar outcomes. To understand the possible origin of the higher reaction rate at 0.3 V vs RHE, we considered an aspect of the H_2O/Pt system that has not been previously discussed in the context of the electrochemistry of CH_4/Pt: the potential dependence of the structure of adsorbed H_2O. Our interest in this aspect of the system was motivated by a recent report on CO electro-oxidation, where the nature of anodic stripping prepeak was contrasted after potential holds in the $H_{(upd)}$ and double-layer regions. [**192**] It was determined in that study that the presence of Pt–H results in relaxation of the structure of the coadsorbed CO and H_2O layer and contributes to the origin of the prepeak.

Given that the disordered water structure has been evoked for explanations of the *CO stripping prepeak, it is logical that this near-surface H_2O layer originating from interactions with Pt–H (sometimes termed adsorbed H_2O) in some way uniquely influences the nature of the interaction of CH_4 with Pt and its subsequent chemical oxidation to *CO. In the framework of this hypothesis, the hydrophobic nature of an initial H_2O layer is interrupted by adsorbed hydrogen, which yields a hydrogen-bonding network with H_2O. Our SEIRAS results indicate a weak feature at 1595 cm^{-1} after holding the potential at 0.3 V vs RHE, which can be attributed to the δ(HOH) mode of adsorbed H_2O. This 1595 cm^{-1} δ(HOH) mode has previously been assigned in the H_2O/Pt system specifically to adsorbed H_2O whose oxygen lone pair interacts with the surface. [**130**] It is therefore possible that the presence of the disordered water structure contributes to the potential dependence of the charge generation rate in the CH_4/Pt system, as it does for CO/Pt. We

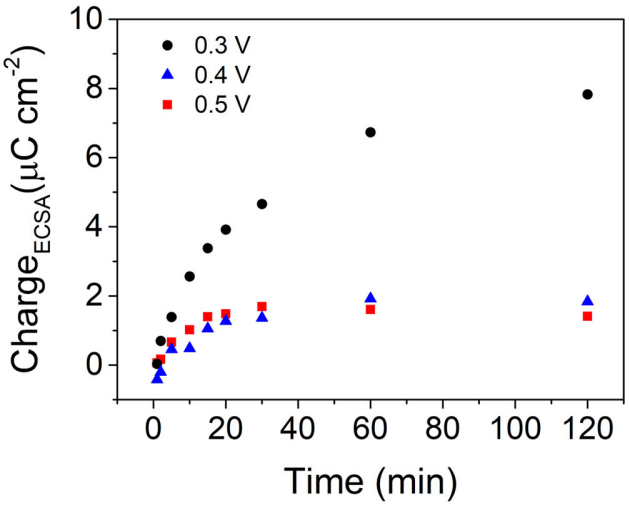

FIGURE 3.6. Time dependence of the total integrated charge (background-corrected) of the oxidative stripping feature after the interaction of CH_4 with Pt at 0.3, 0.4, and 0.5 V vs RHE for 1 h (0.1 M $HClO_4$; 1 atm of CH_4).

note that the stripping charge in the CH_4/Pt system was lower after holding at a potential deeper within the $H_{(upd)}$ region (Figure 3.5). This can be readily explained by the competition for Pt sites that exists between H^+ discharge and CH_4 decomposition/oxidation, since it is well-known that the density of underpotential-deposited hydrogen increases as the potential approaches 0 V vs RHE. [**91**, **125**] Therefore, taken together and interpreted in the context of the available literature, the results reported here imply that an optimum surface density of adsorbed H exists for CH_4 decomposition/oxidation at Pt electrodes.

The data in Figure 3.6 show that the total oxidative stripping charge resulting from the CH_4–Pt interaction is lower after holding Pt at potentials above 0.3 V RHE, which is consistent with results in early reports on CH_4 oxidation to CO_2 over Pt surfaces. [**126**, **127**, **170**] However, the fact that CH_4 decomposition/oxidation does occur above 0.3 V vs RHE indicates that a differing structure of the H_2O layer, which forms in the absence of Pt–H, cannot alone explain these observations on activity. In an early study of the electrochemistry of CH_4/Pt, Niedrach et al. briefly explained the decrease in oxidative stripping charge after holds at higher potentials through the existence of a competition between the rate of adsorption of CH_4 and the increasing rate of oxidation of adsorbates over the surface at potentials above 0.3 V. [**127**] This given interpretation is quite reasonable, but elaboration is required in this context. The argument, which proposes that hydrogen is not the

only adsorbate on the Pt surface in the $H_{(upd)}$ region, provides an explanation for the change in activity in the lowest potential region studied here. Van der Niet et al. found that as potential is increased within the $H_{(upd)}$ region, *H is replaced by *OH at step sites on the Pt surface. [**172**] In other words, *H and *OH species coexist at Pt steps in the $H_{(upd)}$ region. Therefore, considering the slight stabilizing effect of low *H coverage on CHx chemisorption, [**54**] we suggest that the balance between the *H and *OH is highly influential to $*CH_x$ conversion to *CO over Pt step sites. Single crystal electrode studies have demonstrated that hydrogen adsorption/desorption peaks are observed at different potentials depending on the exposed Pt facets. [**33**, **45**, **48**] Distinct voltammetry features observed in the $H_{(upd)}$ region of polycrystalline Pt were assigned to hydrogen adsorption/desorption on Pt(110) and Pt(100) steps. [**114**,**155**,**199**] The lower potential $H_{(upd)}$ peak was attributed to adsorption and desorption on Pt(110) due to the weak interaction of this surface with *H/*OH. [**172**] In contrast, Pt(100) is characterized by stronger interaction with *H/*OH, which facilitates the generation of *O at steps and was therefore correlated to the presence of the $H_{(upd)}$ peak at the higher potential. [**155**, **172**] These prior single crystal studies therefore raise the possibility that the lower activity observed here for the CH_4/Pt system at lower reaction potentials could be influenced by the identities of the exposed facets of the polycrystalline Pt examined, which are unknown. If this were true, results from these studies imply the less active Pt(110) surface would be exposed, since it is associated with a weaker interaction with *H/*OH. In a notable recent work, Ma et al. reported that Pt(100) is associated with high electrocatalytic activity for CH_4 oxidation. [**109**] The interaction strength of surface oxidants (*O/*OH) with the Pt surface was provided as a possible explanation for the intrinsic activity of Pt(100). These studies provide convincing additional evidence that the composition of adsorbates and their binding energies with Pt are influential aspects of electrocatalytic CH_4 oxidation to *CO, as would be expected.

The composition of the surface adsorbates layer is pH-dependent [**31**, **113**, **114**, **151**, **155**, **172**, **199**] (especially surface concentrations of *H, $*OH_2$, *OH, and *O); therefore, additional voltammetry experiments on the CH_4/Pt system were performed in electrolytes with differing bulk pH. Figure 3.13 provides steady-state CVs of platinized Pt in N_2-purged electrolytes at pH values of 0, 1, 3, and 13. We note that the pH range 3–12 was omitted from this study due to the associated required use of buffer solutions containing ions such as PO_4^{3-} and SO_4^{2-} which interact strongly

with the surface. [**47**,**130**,**163**] Small variations among the characteristic CV features of Pt were observed from pH 0 to 3. The reversible features associated with the $H_{(upd)}$ region shifted significantly in the anodic direction for pH 13, consistent with observations made in prior reports. [**31**,**113**,**155**] There are perhaps multiple phenomena that simultaneously contribute to the shift in H adsorption/desorption potentials when plotted on the RHE scale. [**31**,**114**,**151**,**155**,**172**,**199**] Sheng et al. have proposed that anodic shifts of these features result from an increase in hydrogen binding energies, [**155**] and Koper and co-workers have suggested additionally that OH adsorption contributes significantly to the features' shifts with increasing pH. [**31**, **172**]

Figure 6 provides outcomes of voltammetry experiments on the CH_4/Pt system in the acidic and alkaline electrolytes. Here, the holding-time dependences of the charge density associated with the oxidative stripping features are compared. The data indicate that the highest CH_4 decomposition/oxidation reaction rate is obtained at pH 3, with pH 0 and 1 yielding similar activities and pH 13 yielding high initial rates that decrease dramatically at longer holding times. The increased activity observed at pH 3 over that at pH 0 and 1 is not readily correlated to any adsorption-related feature of the steady-state CVs in N_2-purged electrolytes, so understanding the origin of this difference is difficult with the available data. We speculate that since the slight increase in pH is expected to increase the H binding energy, [**155**] this change could cause a subtle alteration of the local structure of the near-surface H_2O layer, induced by its interaction with Pt–H (discussed above in the context of the observed potential dependence of activity). In other words, just as the absence of *H was shown to affect CO adsorption/oxidation behavior through the nature of the adsorbed H_2O structure, [**192**] more strongly bound *H could influence outcomes in the CH_4/Pt system through a similar mechanism (although this claim has not been examined systematically to our knowledge). It is also known that ClO_4^- can weakly adsorb on the Pt surface, where it interacts with *OH. [**68**] This fact increases the complexity of the possible influence of pH on this system, since the lower concentrations of the ClO_4^- anion at lower pH values may alter *OH binding strength. Although these results and literature observations do not convey a clear explanation for the pH dependence of activity in acidic electrolytes, it is logical that the composition of adsorbates and their interactions on the surface influence activity in the CH_4/Pt system.

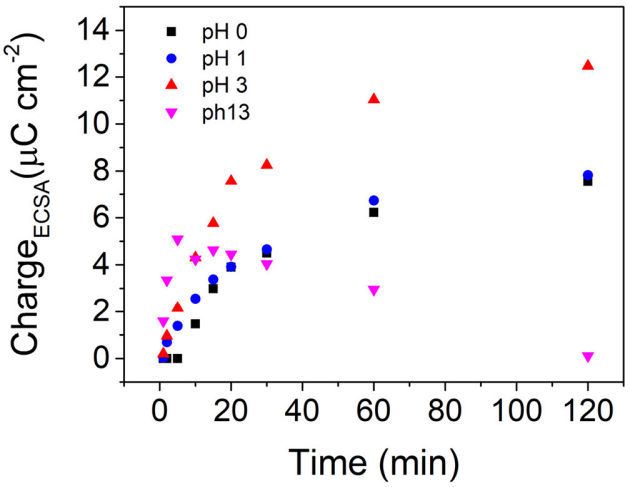

FIGURE 3.7. Time dependence of the charge density associated with the oxidative stripping feature in 0.001–1 M $HClO_4$ (for pH ¡ 3) (0.1 M KOH (for pH 13); 50 mV s^{-1} anodic scan; 1 atm of CH_4).

Voltammetry results at pH 13 show that the CH_4 decomposition/oxidation reaction rate increases over the first few minutes at 0.3 V vs RHE, after which there is a sudden decrease. Although we do not have a clear understanding of this behavior, it is likely related to both the increased amount of *OH [**172**] as well as the coadsorption of K+ in this condition. [**38**, **113**, **114**] It is unknown why the reaction rate should increase at early times. The result may imply that K^+ adsorption is also time-dependent in these conditions; the time dependence of CO adsorption on Pt electrodes has been shown to be influenced by the identity of the dissolved cations. [**38**] Although not fully understood, the pH dependence of activity generally is consistent with the claim made throughout this study-that *OH/*O adsorbed at sites with reduced Pt coordination is the most likely oxygen source for *CH_x conversion to *CO. These initial results suggest that a future detailed investigation that considers the coupled effects of pH and ion adsorption could yield interesting insights into the mechanism of CH_4 activation over Pt.

3.3.5. Conclusions. The electrochemistry of the interaction of CH_4 with Pt electrodes at room temperature and atmospheric pressure in aqueous electrolytes has been investigated through a combination of surface-sensitive operando FTIR spectroscopy and voltammetry techniques. The results indicate that CH_4 readily decomposes at the Pt electrode surface and forms *CO, with some additional minor indication of *CHO and *COOH, the presence of which is dependent on the potential history of the electrode. Anodic stripping voltammetry was used to further characterize the CH_4–Pt interaction with varying applied potentials and electrolyte bulk pH. These experiments were supplemented by voltammetry probing the adsorption and electro-oxidation of CO as well as CO_2 reduction and electro-oxidation of *CO resulting from this reaction. These reactions, which are known to produce similar surface-bound C–H–O–containing species, provided important contrast and facilitated interpretation of results on the CH_4/Pt system through comprehensive analysis of the larger literature that exists on the electrochemistry of these related systems. This analysis determined that the most likely reaction centers for CH_4 activation and decomposition to $*CH_x$ are sites with reduced local Pt coordination, especially those at step edges. These fragments readily interact with nearby surface-bound O-containing species, the composition of which is dependent on electrochemical potential and pH. Voltammetry characteristics interpreted through the comprehensive literature available on the aqueous electrochemistry of Pt suggest that the oxidizing species are most likely *OH and *O, which originate from the chemical decomposition of water at highly active defect sites. These findings indicate that even for simple, prototypical electrocatalysts such as Pt, the surface electrochemistry of CH_4 in the presence of H_2O is complex and therefore that future studies on aqueous electrochemical CH_4 conversion would benefit from emphasis on developing an understanding of the nature of reaction centers present on the electrode surface.

3.3.6. Appendix - supporting information for electrochemistry of the interaction of methane with platinum. This appendix covers the supporting data driven from the electrochemical methane oxidation.

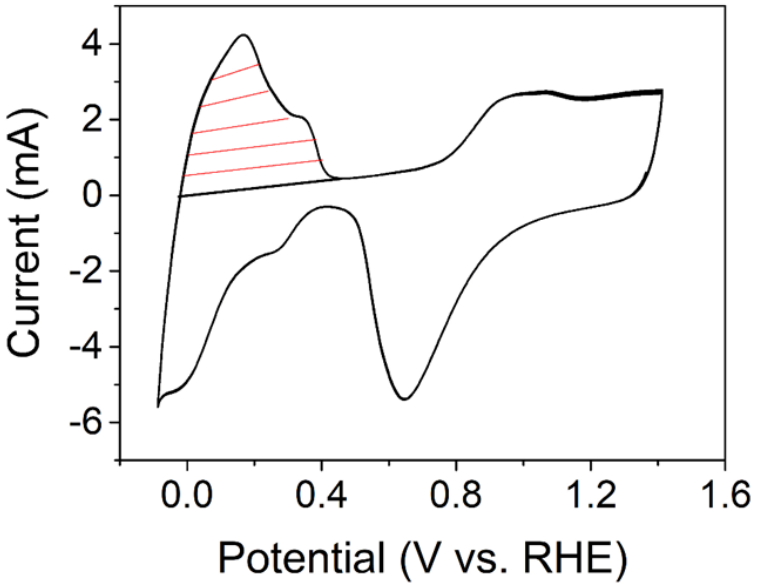

FIGURE 3.8. Representative cyclic voltammetry result for platinized Pt. The dashed area represents the integrated region for determination of electrochemically active surface area (ECSA). 50 mV s^{-1}. N_2-saturated 0.1 M $HClO_4$. 1 atm N_2.

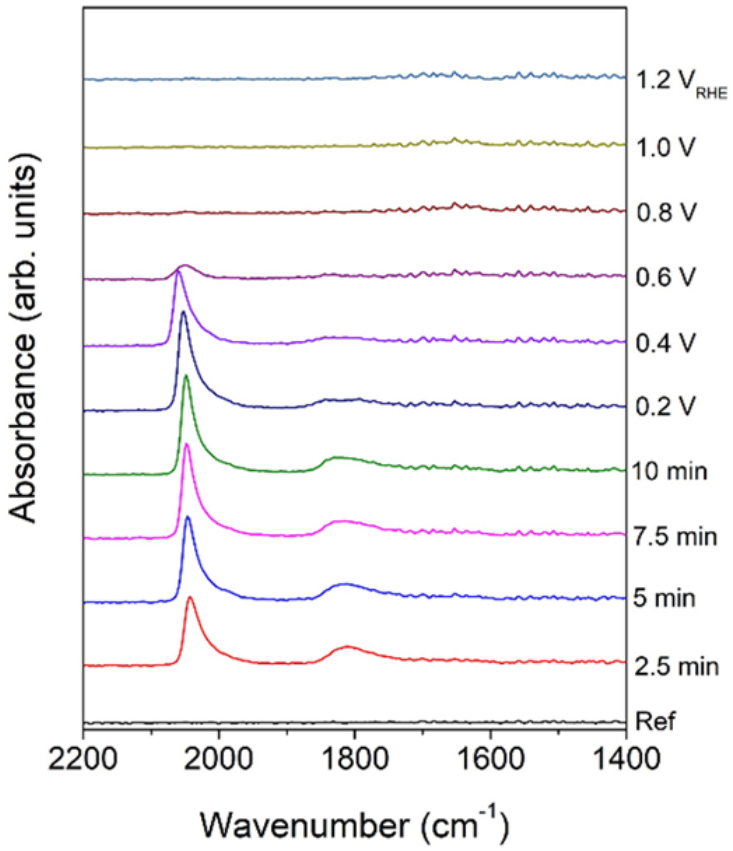

FIGURE 3.9. Operando ATR-SEIRAS spectra associated with electrocatalytic CO_2 reduction at Pt electrodes during CO_2 purging for 10 min with potential held at 0.1 V vs RHE followed by anodic scan to 1.2 V vs RHE. 50 mV s^{-1}. CO_2-saturated 0.1 M $HClO_4$; 1 atm CO_2.

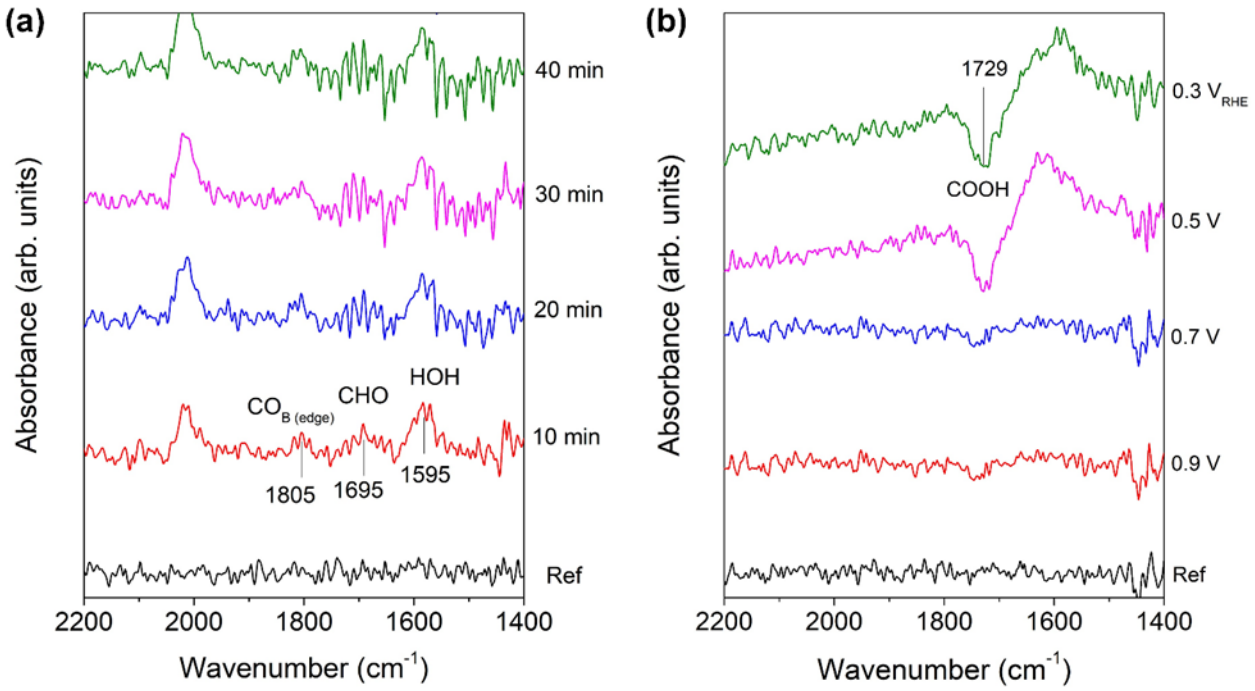

FIGURE 3.10. Additional operando ATR-SEIRAS results associated with the interaction CH_4 with the Pt surface. (a) Magnification of the 1400-2200 cm^{-1} spectral range indicating the growth of additional features with increasing time at 0.3 V vs RHE. Reference spectrum corresponds to the initial scan recorded at 0.3 V vs RHE at t = 0. (b) Spectra associated with a cathodic scan from 1.1 to 0.3 V vs RHE, with the reference spectrum corresponding to the initial scan recorded at 1.1 V vs RHE. 50 mV s^{-1}. CH_4-saturated 0.1 M $HClO_4$; 1 atm CH_4.

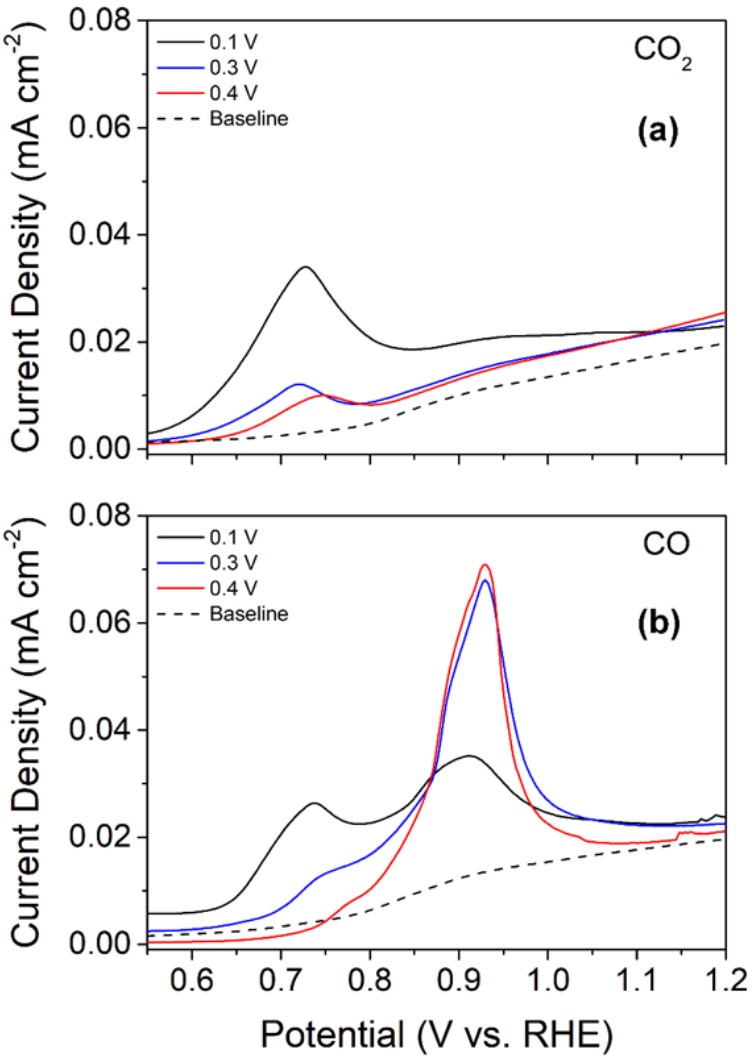

FIGURE 3.11. Anodic stripping of (a) CO_2 and (b) CO at different holding potentials. Magnification of the oxidative stripping feature present in the anodic scans following potential holds at 0.1, 0.3, and 0.4 V vs RHE in (a) CO_2-saturated 0.1 M $HClO_4$ and (b) CO-saturated 0.1 M $HClO_4$. 50 mV s^{-1}; 1 atm CO_2 or CO.

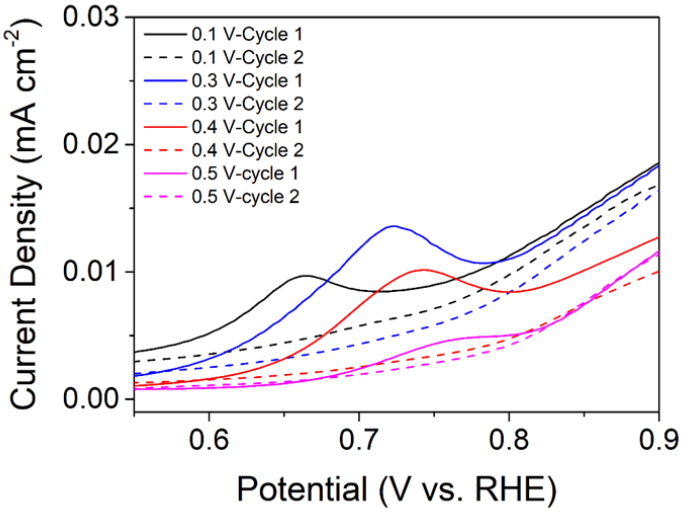

FIGURE 3.12. Magnification of the oxidative stripping feature present in the anodic scans following potential holds at 0.1, 0.3, and 0.4 V vs RHE in CH_4-saturated 0.1 M $HClO_4$ (a) 50 mV s^{-1}; 1 atm CH_4.

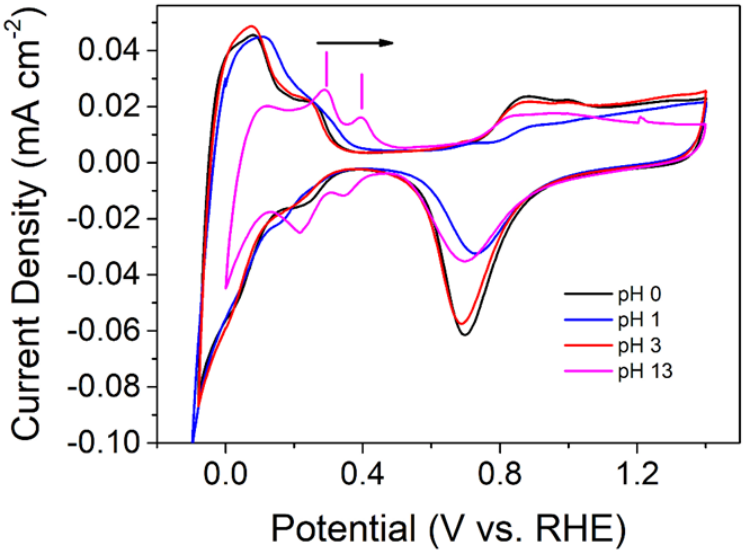

FIGURE 3.13. Cyclic voltammetry result for platinized Pt in N_2-saturated electrolytes with varying pH. 50 mV s^{-1}. 0.01 to 1 M $HClO_4$ (for pH ¡ 3); 0.1 M KOH (for pH 13); 1 atm N_2.

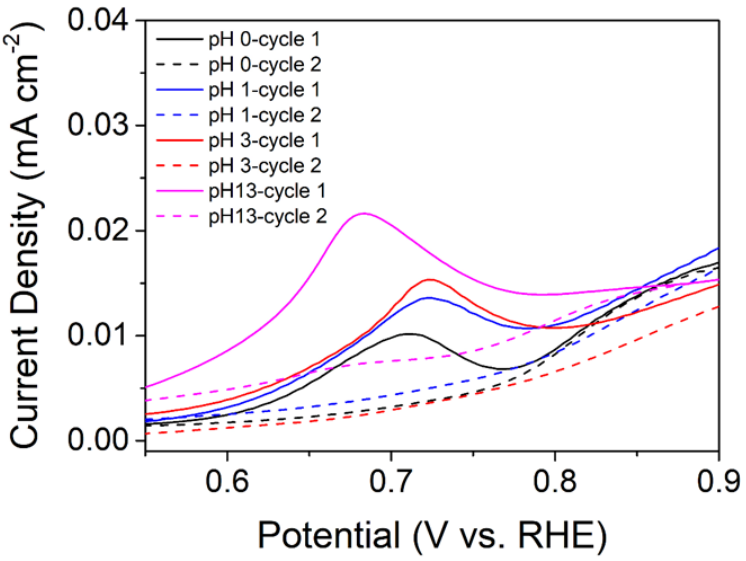

FIGURE 3.14. Magnification of the oxidative stripping feature present in anodic scans following potential holds at 0.3 V vs RHE in CH_4-saturated electrolytes with varying pH. 50 mV s^{-1}. 0.01 to 1 M $HClO_4$ (for pH ¡ 3); 0.1 M KOH (for pH 13); 1 atm CH_4.

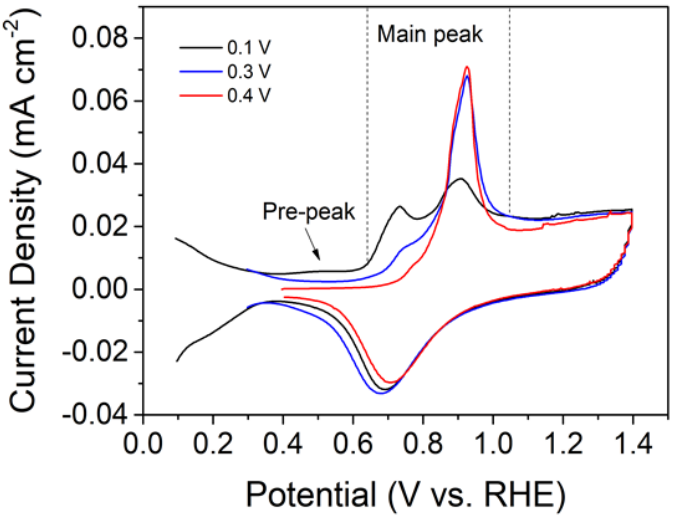

FIGURE 3.15. The oxidative stripping features associated with the interaction of CO with Pt after holding for 1 h at 0.1, 0.3, and 0.4 V vs RHE. 50 mV s^{-1}; 0.1 M $HClO_4$; 1 atm CO.

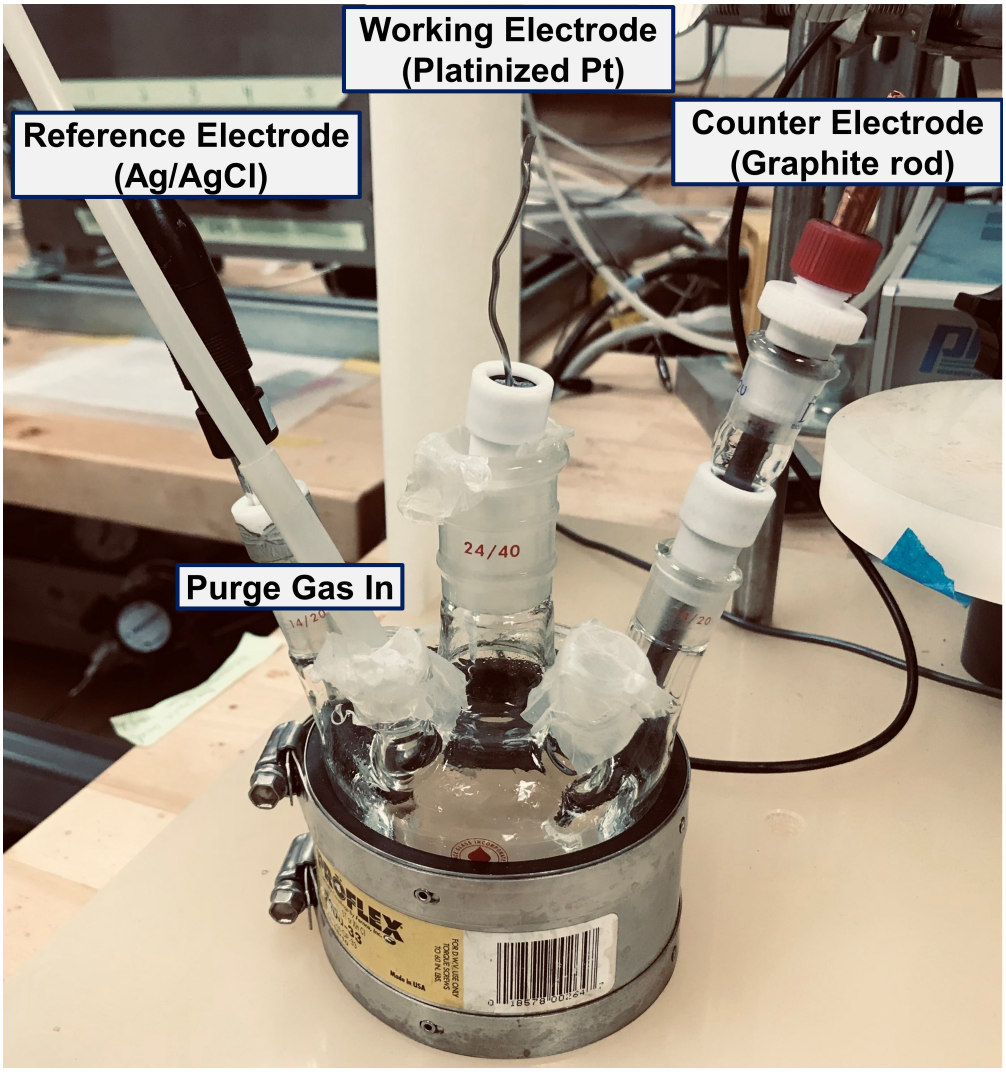

FIGURE 3.16. a standard three-electrode cell with a platinized Pt coil working electrode, a silver-silver chloride (Ag/AgCl) reference electrode, and a graphite rod counter electrode.

3.4. Appendix

3.4.1. Utilization of electricity instead of temperature for the light alkane oxidation over AuPd catalyst in the presence of H_2O_2. Electrochemical processes are a significant alternative for thermal catalysis because they facilitate direct modulation of catalyst surface in establishing optimized operating conditions. Therefore, we investigated the influence of potentiostatic control on a liquid-phase thermal catalytic system very close to that examined in Chapter 2. Figure 3.17 shows the effect of applied potential over the products' distribution obtained from the partial oxidation of methane with the presence of H_2O_2 as the oxidant. Different potentials (Figure 3.17b) were applied and a significant improvement was observed only at 1.3 V vs RHE (Figure 3.17a). Figure 3.17a compares the integrated NMR signals for different products under various reaction conditions. The measurement conducted at 25 °C with an open circuit potential generated only methylhydroperoxide with a small quantity with respect to other conditions as expected. A slight temperature change enhanced the activity in terms of products' distribution and quantity significantly. Electrochemical potential applied at 1.3 V vs RHE, on the other hand, also increased the amount of product generated and indicated that it could be an alternative solution for using less amount of H_2O_2. In fact, the NMR signals obtained at relatively higher pressure (3 bar) and H_2O_2 concentration are very similar to those under the electrochemical potential. This also shows that electrochemical potential could replace the effect of the pressure by promoting the optimized operating conditions as mentioned before.

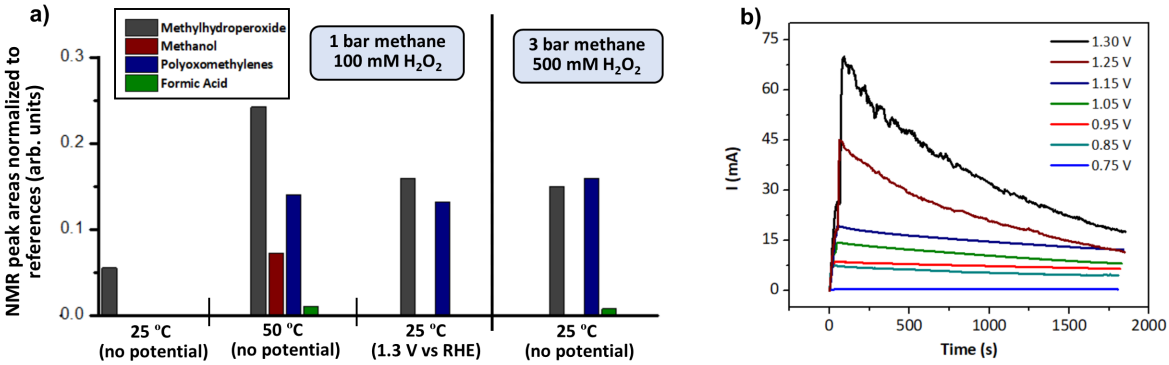

FIGURE 3.17. a) Integrated NMR signals obtained from partial oxidation of methane under various reaction conditions on AuPd catalyst. b) The currents generated at different potentials from methane oxidation in the presence of H_2O_2 oxidant.

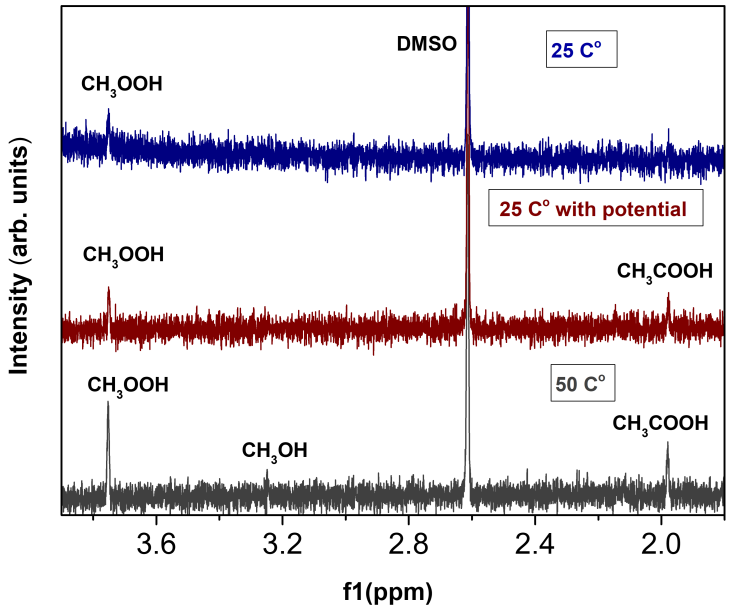

FIGURE 3.18. NMR spectrum of the oxygenates generated from partial oxidation of methane under various reaction conditions on AuPd catalyst. 0.1 M $HClO_4$; 1 bar CH_4; 100 mM H_2O_2.

CHAPTER 4

Investigating the near-surface gas phase during thermal catalysis*

Chapter 4.2 is partially adapted from a published work:

B. Zhou, E. Huang, R. Almeida, S.M. Gurses, A. Ungar, J. Zetterberg, A.R. Kulkarni, C.X. Kronawitter, D.L. Osborn, N. Hansen, J.H. Frank*; Near-surface imaging of the multi-component gas phase above a silver catalyst during partial oxidation of methanol, *ACS Catal.*, 2021, **11**, 155-168.

&

Chapter 4.3 is fully adapted from a published work:

S.M. Gurses, T. Price, A. Zhang, J.H. Frank, N. Hansen, D.L. Osborn*, A.R. Kulkarni*, C.X. Kronawitter*; Near-Surface Gas-Phase Methoxymethanol Is Generated by Methanol Oxidation over Pd-Based Catalysts, *J. Phys. Chem. Lett.*, 2021, **12**, 11252-11258.

These works were supported by the U.S. Department of Energy (DOE), Office of Basic Energy Sciences (BES), Division of Chemical Sciences, Geosciences and Biosciences (CSGB) under Grant DE-SC0020320. Most of the experimental work was performed at Sandia National Laboratories, Livermore.

*The content of this chapter has previously been published in Ref. [**53**, **200**].

4.1. Overview of the chapter 4

Chapter 2 and 3 described the aqueous-phase thermal and electrochemical systems extensively. In Chapter 4, we shifted our direction to the gas-phase conversion routes mainly focusing on oxidative coupling of methane (OCM) reaction. Near-surface gas-phase diagnostic techniques were proposed to examine this complex reaction to elucidate the interaction of surface of the catalyst with the gas-phase collisions and their impact on overall activity. However, the complicated nature of OCM involving multiple phases led us to benchmark our system over a relatively simple reaction. An industrially viable and comprehensively studied reaction, methanol oxidation, was selected due to resembling reaction pathway with OCM for the formaldehyde production. Both OCM and methanol partial oxidation to formaldehyde involve as a primary step the dehydrogenation of a C–H bond, resulting in the formation of organic substrates with a single carbon atom. [**123**] Therefore, Chapter 4.2 initially introduces the near surface measurement techniques for methanol oxidation above silver catalyst. The diverse product distribution detected above the silver surface by molecular beam mass spectrometry (MBMS) encouraged us to work on other catalyst surfaces including Pd, AuPd, $AuPd_2$, Au_2Pd. Chapter 4.3 demonstrates our studies on methanol oxidation mainly over Pd film catalyst. Methoxymethanol, an obscure intermediate, is observed above Pd, Au_xPd_y alloys, Ag and oxide-supported Pd. We utilized a heatable sample holder for thin film metal catalysts in our initial studies over Ag and Pd thin films. Later, we modified our sample holder for powder catalysts, e.q. oxide-supported Pd measurements, with the integration of a ceramic heater. Further experiments coupled with diffuse reflectance infrared Fourier transform spectroscopy (FTIR-DRIFTS) were also performed on oxide-supported Pd but the current results were not included in this dissertation. Modified sample holder and heater in near-surface gas-phase detection techniques for mounting the powder catalyst and reaching the elevated temperatures, respectively enabled us to conduct initial experiments for OCM. Preliminary results on OCM diagnosed by MBMS are briefly covered in the Appendix 4.4 of this chapter.

4.2. Near-surface imaging of the multicomponent gas phase above a silver catalyst during partial oxidation of methanol

4.2.1. Abstract. Fundamental chemistry in heterogeneous catalysis is increasingly explored using operando techniques in order to address the pressure gap between ultrahigh vacuum studies and practical operating pressures. Because most operando experiments focus on the surface and surface-bound species, there is a knowledge gap of the near-surface gas phase and the fundamental information the properties of this region convey about catalytic mechanisms. We demonstrate *in situ* visualization and measurement of gas-phase species and temperature distributions in operando catalysis experiments using complementary near-surface optical and mass spectrometry techniques. The partial oxidation of methanol over a silver catalyst demonstrates the value of these diagnostic techniques at 600 Torr (800 mbar) pressure and temperatures from 150 to 410 °C. Planar laser-induced fluorescence provides two-dimensional images of the formaldehyde product distribution that show the development of the boundary layer above the catalyst under different flow conditions. Raman scattering imaging provides measurements of a wide range of major species, such as methanol, oxygen, nitrogen, formaldehyde, and water vapor. Near-surface molecular beam mass spectrometry enables simultaneous detection of all species using a gas sampling probe. Detection of gas-phase free radicals, such as CH_3 and CH_3O, and of minor products, such as acetaldehyde, dimethyl ether, and methyl formate, provides insights into catalytic mechanisms of the partial oxidation of methanol. The combination of these techniques provides a detailed picture of the coupling between the gas phase and surface in heterogeneous catalysis and enables parametric studies under different operating conditions, which will enhance our ability to constrain microkinetic models of heterogeneous catalysis.

4.2.2. Introduction of Near-Surface Gas-Phase Diagnostic Techniques.

Optical Diagnostic

Understanding the interaction of near gas-phase chemistry with surface chemistry is essential for elucidating the fundamentals of heterogeneous catalysis. However, probing these interactions under reaction conditions is challenging both experimentally and theoretically. Therefore, we created

an optical spectroscopy apparatus to characterize gas-surface interactions. Specifically, 2-D laser-induced fluorescence (LIF) was optimized for imaging formaldehyde produced from methanol above the Ag surface. We were able to observe the effect of different flow conditions on the developed boundary layer above the catalyst surface. The obtained LIF images are beyond the scope of this thesis and therefore not included. To complement this optical approach, we also performed MBMS measurements to map out the local view of the species. We were able to provide multiple views of the reaction taking place on the Ag surface with the help of these two complementary techniques.

Near-Surface Mass Spectrometry

MBMS measurements were performed in a separate chamber from the optical diagnostics, and a schematic of the experimental setup is shown in Figure 4.1. The apparatus consists of a reactor chamber that is connected via a quartz sampling probe to a high-resolution reflectron time-of-flight mass spectrometer (RTOF-MS). The quartz nozzle has an opening cone angle of 40° and a ~ 50 μm orifice diameter. The chamber consists of a two-stage, differentially pumped vacuum system, which ensures a rapid pressure drop from 600 Torr (800 mbar) in the reactor chamber to 10^{-6} Torr in the ionization region of the mass spectrometer. This pressure reduction leads to the formation of a molecular beam in which further interactions between the molecules are prevented. This "freezing" of the chemistry in the molecular beam ensures that the mass spectra report on the gas composition immediately upstream of the orifice and enables the detection of highly reactive species, such as free radicals, which cannot be detected in traditional mass spectrometry monitoring of reactor effluent gases.

4.2.3. Highlighted results from MBMS measurement motivating further studies on different metal surfaces. Catalytic processes consist gas-phase interactions and the dynamic exchange of species between the gas phase and surface. Therefore, observing the spatially resolved gas-phase species could promote the knowledge in catalysis research. To detect near-surface gas-phase species generated during methanol oxidation, we implemented MBMS measurements 500 μm above the Ag surface. This technique provides unique advantages in different ways with respect to conventional mass spectrometry available in our laboratory at UC Davis. One of the most significant advantages is managing to probe right above the catalyst surface (500 μ). This is not possible by utilizing a conventional mass spectrometry whose effluent gas detection probe is located

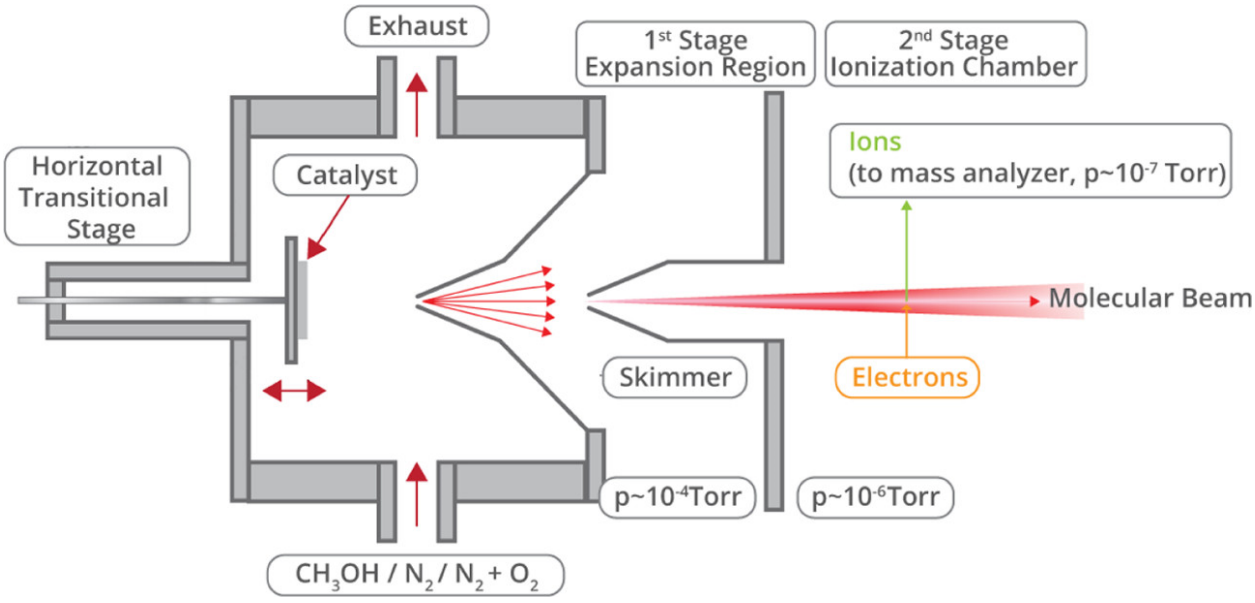

FIGURE 4.1. Schematic experimental setup for the near-surface MBMS experiments. The distance between the catalytic surface and the sampling probe is varied between 0 and 5 mm.

far away from the catalyst surface. MBMS approach also enables us to observe changes in gas-phase neutral molecule profiles as a function of surface temperature, which results in species-specific light-off curves. Here we obtained light of curves of various species detected with MBMS under a flow of CH_3OH , O_2, and N_2. Methanol vapor was introduced by flowing nitrogen through a bubbler filled with liquid methanol. The reactant flows (CH_3OH/O_2, 2.5/1) were regulated using calibrated mass flow controllers and a laminar boundary layer flow across the catalyst was created. Light-off curves for additional species detected with MBMS are shown in Figure 4.2 for surface temperatures from 180 to 282 °C. These plots show integrated signals for the reactants CH_3OH and O_2 (Figure 4.2a) and the products and intermediates H_2O, CO_2, CH_2O, C_2H_4O (Figure 4.2b), $C_2H_6O_2$, C_2H_6O, $C_2H_4O_2$, and CH_2O_2 (Figure 4.2c). The light off is clearly visible near 235 °C, with the appearance of multiple products discussed above. All product signals light off at the same temperature near 235 °C. Species-resolved temperature dependences such as these will provide important inputs to the construction and constraint of microkinetic models. We anticipate that such combined experimental and theoretical approaches will convey mechanistic information about the creation and consumption of species both on the surface and in the gas phase.

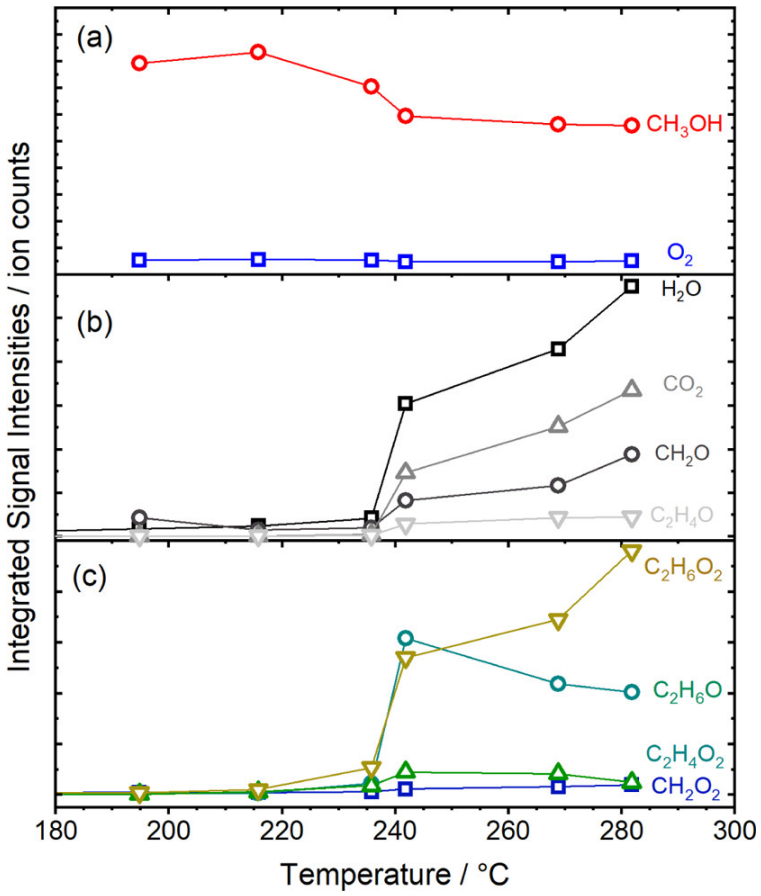

FIGURE 4.2. Integrated mass spectral signal as a function of the surface temperature for (a) reactants CH_3OH and O_2 and the products and intermediates (b) H_2O, CO_2, CH_2O, C_2H_4O, and (c) $C_2H_6O_2$, C_2H_6O, $C_2H_4O_2$, and CH_2O_2.

4.3. Near-surface gas-phase methoxymethanol is generated by methanol oxidation over Pd-based catalysts

4.3.1. Abstract. Catalytic conversion of alcohols underlies many commodity and fine chemical syntheses, but a complete mechanistic understanding is lacking. We examined catalytic oxidative conversion of methanol near atmospheric pressure using operando small-aperture molecular beam time-of-flight mass spectrometry, interrogating the gas phase 500 μm above Pd-based catalyst surfaces. In addition to a variety of stable C_{1-3} species, we detected methoxymethanol (CH_3OCH_2OH)–a rarely observed and reactive C_2 oxygenate that has been proposed to be a critical intermediate in methyl formate production. Methoxymethanol is observed above Pd, Au_xPd_y alloys, and oxide-supported Pd (common methanol oxidation catalysts). Experiments establish

temperature and reactant feed ratio dependences of methoxymethanol generation, and calculations using density functional theory are used to examine the energetics of its likely formation pathway. These results suggest that future development of catalysts and microkinetic models for methanol oxidation should be augmented and constrained to accommodate the formation, desorption, adsorption, and surface reactions involving methoxymethanol.

4.3.2. Introduction. Catalytic transformations of alcohols enable the production of a variety of commodity chemicals, [**12**,**28**,**121**] and methanol specifically serves as an important C_1 platform molecule for the synthesis of $C_2{}^+$ organics, which can occur through oxidation in mild conditions. [**27**,**59**,**159**,**190**] One notable target product is methyl formate (MF; $C_2H_4O_2$; CH_3OCHO), which can be produced in high yields from methanol oxidation and has been determined [**99**] to possess many favorable physicochemical characteristics that make it an effective C_2 building block for chemical synthesis (e.g., dimethylformamide, acetic acid, and ethylene glycol). [**107**] Similarly, dimethoxymethane (DMM; $C_3H_8O_2$; $CH_3OCH_2OCH_3$) can be produced from methanol through a number of pathways and is valuable both as a chemical precursor and as an oxygenated synthetic fuel. [**161**]

The existing literature establishes that the nature of the catalyst surface strongly influences the molecular-level mechanisms operable for oxidative coupling of methanol-derived oxygenates. [**12**, **168**] Heterogeneous catalytic formation of $C_2{}^+$ esters (e.g., MF) and ethers (e.g., DMM) requires surface C–O–C coupling events that involve the primary C_1 products of methanol partial oxidation–formaldehyde or formic acid. [**161**] For the case of MF generation, three oxidative pathways are primarily discussed: (1) surface coupling of adsorbed methoxy (CH_3O^*) and formaldehyde ($HCHO^*$); [**166**,**190**] (2) surface $HCHO^*$ dimerization [**120**] (Tishchenko reaction); and (3) CH_3OH reactions with adsorbed formate ($HCOO^{-*}$). [**145**] While the mechanism of MF formation for a given catalytic system has occasionally been deduced from product distributions, kinetic analyses, or outcomes of probe reactions, generally the intermediate species resulting from the initial C–O–C coupling event itself is not experimentally observed.

In this Letter, we use molecular beam mass spectrometry (MBMS) to invesigate, during methanol oxidation catalysis, the near-surface gas phase (within ca. 500 μm) using Pd-based catalysts, which are among the most commonly examined materials for selective methanol conversions.

[**21**, **26**, **28**, **30**, **34**, **74**, **101**, **150**, **171**, **177**, **182**, **184**, **185**, **186**, **187**, **188**] Our most important observation is that methoxymethanol (CH_3OCH_2OH), a rarely observed C_2 ether-alcohol that is highly reactive in conditions of heterogeneous catalysis, [**103**] is a primary product present in the near-surface gas phase for all systems and conditions examined. This observation provides strong evidence that surface coupling of methoxy and formaldehyde (pathway (1) above) occurs for these examined systems (Pd, Au_xPd_y alloys, and MgO-supported Pd).

Speciation in the Near-Surface Gas Phase during Oxidative Methanol Conversion. The details of the near-surface MBMS system employed here have been described in a recent publication. [**200**] Briefly, through use of a small-aperture differentially pumped sampling nozzle, MBMS effectively "freezes" the local composition in the gas phase by rapid gas expansion, which transports near-surface species to the mass analyzer (a high-resolution reflectron time-of-flight mass spectrometer (RTOF-MS)). The rapid transition to a collision-less molecular beam isolates all species from further interactions, preserving free radicals and reactive intermediates. Additional details are provided in the Appendix 4.3.5. Through use of this technique and its ability to characterize even highly reactive species from the gas phase, we investigate the near-surface product species during methanol oxidation catalysis.

4.3.3. Results and Discussion. Figure 4.3 shows representative near-surface MBMS results of methanol oxidation over polycrystalline Pd (see Appendix 4.3.5 for synthesis details). Figure 4.3a provides a typical mass spectrum recorded during a steady-state reaction at 160 °C, which shows a variety of oxygenates and CO_2 in the near-surface region. Chemical species were assigned by consideration of both parent ions and fragments from dissociative ionization of products. Figure 4.3b provides a magnification of the spectrum at nominal m/z of 44 and 45. The high resolution of MBMS measurements ($m/\Delta m = 3500$) facilitates identification of secondary products, their isotopologues, as well as fragment ions that provide additional "fingerprints" of neutral species. Here, the use of "soft" ionization [**24**] at electron kinetic energy of 17 eV, instead of traditional 70 eV ionization, minimizes fragmentation and resulting ambiguities in assignments. For example, C_2H5O^+ ($m/z = 45$) and $C_3H_7O_2{}^+$ ($m/z = 75$) are known fragments of DMM ($C_3H_8O_2$), [**167**,**200**] and the magnitudes of their associated signals can be measured for specific electron energies (Figure 4.7). Throughout this study, reported DMM signals correspond to those of $C_3H_7O_2{}^+$. Similarly,

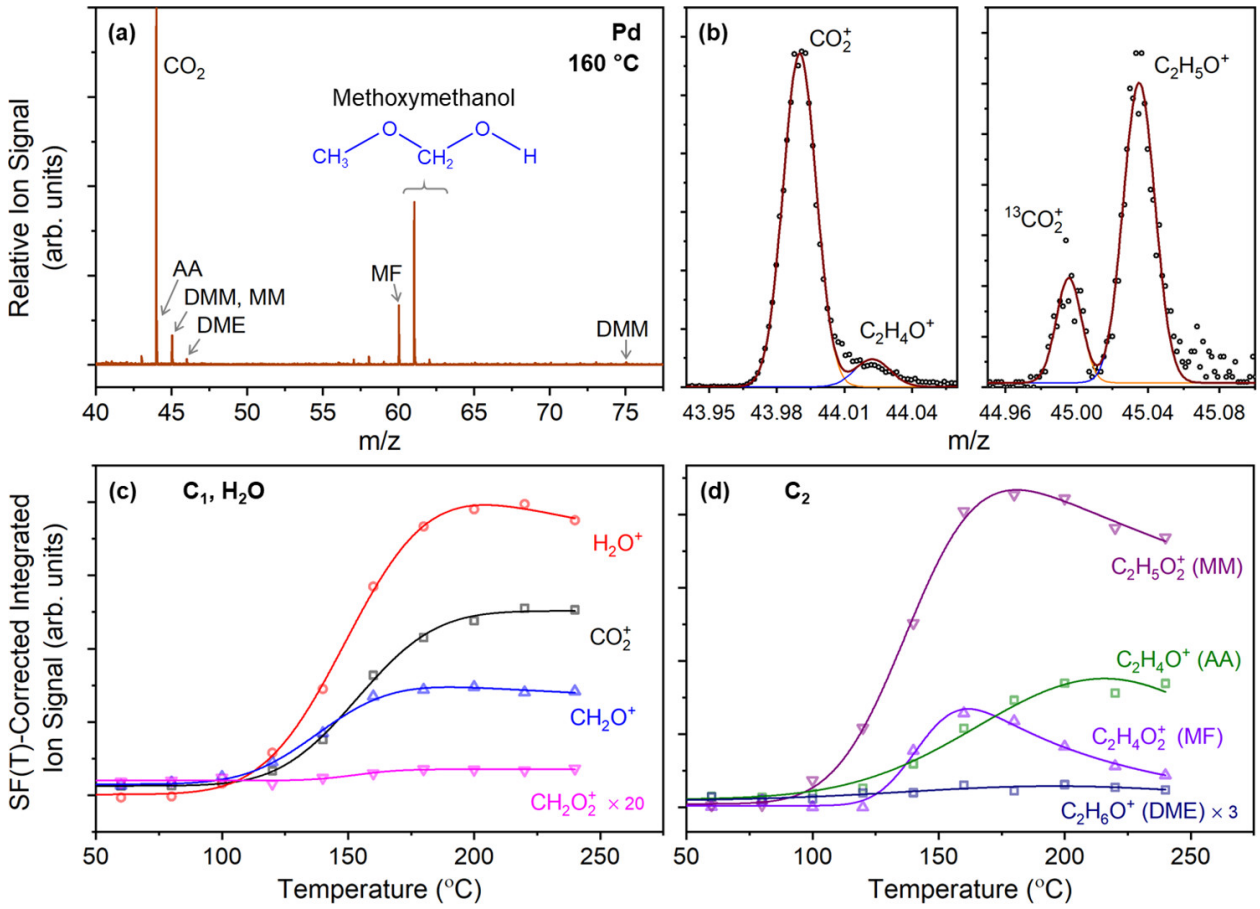

FIGURE 4.3. Near-surface molecular beam mass spectrometry results associated with methanol oxidation over polycrystalline Pd. P = 600 Torr; reactant feed ratio $CH_3OH/O_2 = 0.07$; sampling nozzle located 500 μm above the surface; 17 eV electron energy. (a) Representative mass spectrum (m/z = 40–77.5) and corresponding neutral species recorded during catalysis at 160 °C. (b) Magnification of the spectrum from (a) at nominal m/z = 44, 45. Peaks are deconvolved to resolve CO_2^+, $C_2H_4O^+$, $^{13}CO_2^+$ (natural abundance), and $C_2H_5O^+$. (c) Temperature dependence of the integrated signals of characteristic peaks associated with C_1 products and H_2O. (d) Temperature dependence of C_2 product signals.

$C_2H_4O^+$ (m/z 44) is a known fragment ion of MF when it is ionized at 70 eV, but the signal at m/z 44 is negligible in our experiments when pure MF is measured with an electron energy of 17 eV (not shown).

A variety of closed-shell, stable species were detected during reaction over unsupported Pd film catalysts, with signal intensities dependent on reaction conditions: carbon dioxide (CO_2), formaldehyde (HCHO), formic acid (HCOOH), dimethyl ether (DME, CH_3OCH_3), acetaldehyde

(CH_3CHO), MF (CH_3OCHO), and DMM ($CH_3OCH_2OCH_3$). Although most of these products–especially CO_2, HCHO, and MF–are commonly reported products of methanol oxidation over Pd-based catalysts, to our knowledge, DMM and acetaldehyde have not been reported previously. The detection of this large variety of products results from both the extremely high sensitivity of this MBMS tool (∼1 ppm for neutral species detected as mass-analyzed cations [**143**]) and the near-surface sampling position, which enables detection of products before they are able to further react elsewhere in the reactor or at the catalyst surface.

In Figure 4.3a, a small signal at m/z = 62 corresponds to the molecular formula of methoxymethanol (CH_3OCH_2OH). However, the conspicuously large signal at m/z = 61 corresponds to $C_2H5O_2{}^+$, a known fragment ion from dissociative ionization of methoxymethanol. [**73**, **112**] The observed high ratio of m/z 61 to 62 (methoxymethanol parent ion) serves as an additional fingerprint for this species. [**73**, **112**] The only species observed in this study whose associated parent ion m/z value exceeds 62 (DMM) produces no fragment ions at 61 or 62 when ionized with an electron energy of 17 eV (Figure 4.7). Methoxymethanol has been described as "elusive" [**73**] and has been identified by infrared spectroscopy and mass spectrometry following 10.6 μm infrared irradiation of gas-phase CH_3OH [**73**] or electron radiolysis of solid CH_3OH. [**112**] It has been identified and studied perhaps most rigorously in the context of chemical formation in interstellar ices. [**116**] To our knowledge, methoxymethanol has previously been experimentally observed as a product of continuous methanol oxidation in only a few reports. These studies, [**144**, **146**, **169**] wherein methoxymethanol was referred to as hemimethylal, exclusively involved V_2O_5. In this study, we observe this species in the near-surface gas phase during methanol oxidation over all Pd-based catalysts examined, for multiple CH_3OH/O_2 feed ratios, and over wide ranges of temperature.

Figure 4.3c,d provides the temperature dependences of the integrated signals of H_2O and C_1 and C_2 products of methanol oxidation over polycrystalline Pd. Here, the species' integrated signal intensities were corrected by the temperature-dependent sampling function, SF, (factor $SF(T^g)$ in eq 4.1), which eliminates the effect of temperature on the density of the gas detected by the spectrometry system. [**200**] The reported intensities are proportional to species mole fraction. However, the relative intensities between species in Figure 4.3c,d do not reflect mole fraction ratios;

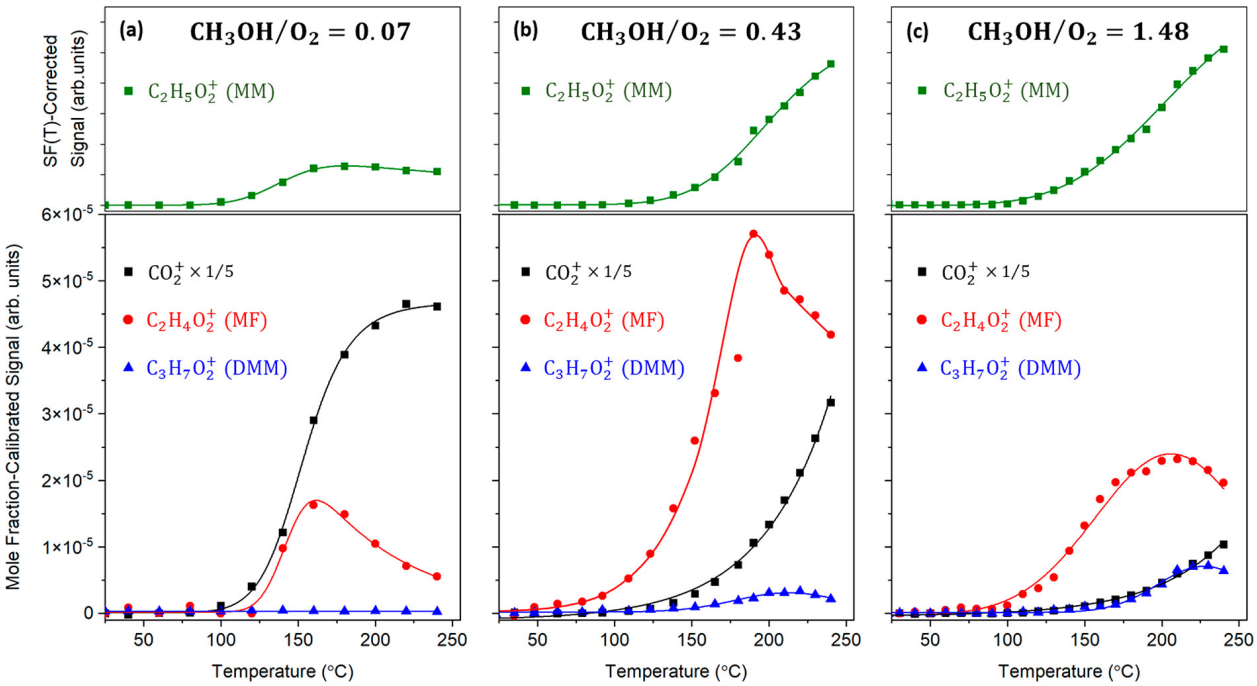

FIGURE 4.4. Temperature dependences of signals for methoxymethanol, CO_2, MF, and DMM during oxidative conversion of methanol over Pd. P = 600 Torr; sampling nozzle located 500 μm above the surface. Results for three reactant feed ratios (CH_3OH/O_2) are provided: (a) 0.07, (b) 0.43, and (c) 1.48. See main text for descriptions of axes labels.

this quantification is possible with further calibration and correction for key species (to be discussed below; Figure 4.4).

The measurements reported in Figure 1 were performed in highly O_2-rich conditions (CH_3OH/O_2 = 0.07). It is known that feed composition has a strong impact on methanol oxidation reaction outcomes; [**171**] we extended our investigation to include two additional feed ratios (CH_3OH/O_2 = 0.43, 1.48). Figure 4.4 compares the temperature dependences of integrated ion signals associated with methoxymethanol, CO_2, MF, and DMM formation over Pd at these three CH_3OH/O_2 feed ratios. A more quantitative analysis of products is possible with this presentation of the data; here, we have calibrated the system's detection sensitivity for each species for which one can obtain a pure reference sample (CO_2, MF, and DMM). These calibrated species are in quantitative ratio to one another–i.e., ratios represent product mole fraction ratios. Unfortunately, no reference sample of methoxymethanol is available, and therefore methoxymethanol signals cannot be calibrated in this way. However, relative changes of methoxymethanol signals with temperature and feed ratio

are meaningful. See Appendix 4.3.5 and Figure 4.8 for details on the calibration procedure. In the future, we intend to measure and quantify methoxymethanol in this system using synchrotron photoionization mass spectrometry, where established methods may be used for estimating photoionization cross sections of species. [**20**]

As expected, the greatest relative amount of CO_2 is generated in the system when the highest O_2 concentration is used (Figure 4.4a). When the concentration of methanol in the feed is increased ($CH_3OH/O_2 = 0.43$; Figure 4.4b), the relative amount of CO_2 decreases and that of MF increases. Further increasing the feed ratio ($CH_3OH/O_2 = 1.48$; Figure 4.4c) results in a decrease in yields of both CO_2 and MF. Interestingly, for both cases associated with increased methanol in the feed (Figure 4.4b,c), a measurable temperature-dependent DMM signal is present (reflected by $C_3H_7O_2^+$), which is not the case for the O_2-rich case ($CH_3OH/O_2 = 0.07$). For both of these cases, the amount of methoxymethanol produced in the near-surface region is very similar.

These general observations regarding the impact of the CH_3OH/O_2 feed ratio appear to be consistent with the known fact that the outcomes of methanol oxidation reactions over Pd are sensitive to the relative concentrations of chemisorbed oxygen versus vacant Pd sites. For example, it has been determined that with Pd clusters, sites with chemisorbed oxygen adjacent to bare Pd activate CH_3OH with lower barriers than sites comprised of pairs of chemisorbed oxygens. [**171**]

On the Role of Methoxymethanol as a Reactive Intermediate during Oxidative Conversion of Methanol. Scheme 4.1 provides an overview of the chemical species observed in the near-surface region (Figures 4.3 and 4.4, placed in the context of the primary chemical steps likely applicable to this catalytic system. At steady state, the near-surface gas-phase composition measured by MBMS reflects the local adsorption/desorption equilibrium of species to/from the surface. That is, for surface-generated species, a higher near-surface gas-phase concentration implies its higher surface concentration at the measured temperature. Scheme 4.1 is useful to highlight the fact that methoxymethanol can serve as a key intermediate in the formation of C_2^+ chemicals.

[a] Methoxymethanol is emphasized at the center. H_2O generated by oxidative dehydrogenation and condensation reactions is omitted for simplicity. The highlighted steps are the subject of the computational analysis in Figure 4.5.

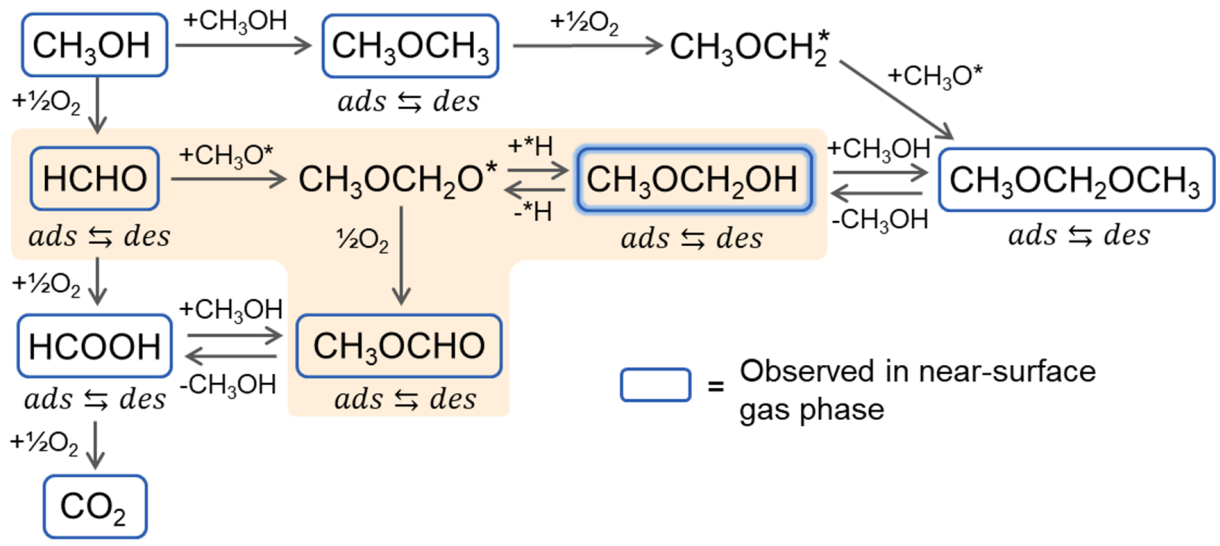

SCHEME 4.1. Overview of Species Observed in the near-Surface Gas Phase over Pd Catalysts, Shown in the Context of a Feasible Reaction Network Motivated by Prior Studies [**168**],[a].

As mentioned above, the reactivity of methoxymethanol has precluded its direct measurement in almost all prior methanol oxidation studies. However, both methoxymethanol and its dehydrogenated form as an alkoxy-hemiacetal adsorbate ($CH_3OCH_2O^*$) have been inferred to be critical intermediate species involved in formation of C_2^+ products over a variety of catalysts with very dissimilar surface chemical properties. For example, a report on methanol oxidation on Ag(110) [**176**] described a reaction path that invoked the hemiacetal adsorbate as an intermediate toward the generation of MF. Later studies utilizing oxide-supported polyoxometalate catalysts suggested a similar role, where $CH_3OCH_2O^*$ or methoxymethanol serve as a precursor for both MF and DMM formation (with reaction paths dictated in part by the acid–base properties of the catalyst surfaces). [**104**] Methoxymethanol has also been inferred to be a critical surface-bound intermediate during methanol oxidation over Al_2O_3-supported Pd catalysts, a system that was associated with near-100% selectivity toward MF. [**101**] Although these studies interpreted MF production as evidence of methoxymethanol or $CH_3OCH_2O^*$ formation, neither species was observed experimentally. Our observations add evidence for the generation of $CH_3OCH_2O^*$ and for the competition between

its oxidation to MF and its hydrogenation to methoxymethanol, where the latter pathway gains flux at the expense of the former with increasing methanol concentration.

Motivated by our operando observations of the near-surface gas-phase composition, along with previous work suggesting that methoxymethanol and hemiacetal are central to the selective generation of methyl formate, [**101**, **160**] we performed calculations using density functional theory to examine the energetic feasibility of these steps on Pd(111) surfaces. Details of the computational methods used are provided in the Appendix 4.3.5. X-ray diffractograms indicate that the polycrystalline Pd films used here were highly (111)-oriented (Figure 4.9), and (111) is the lowest-energy facet of Pd.

In prior accounts that infer its role in methanol oxidation reaction pathways, methoxymethanol formation first requires the generation of surface-bound formaldehyde (HCHO*). Pd-rich surfaces are known to have low energy barriers to O_2 dissociation. [**28**, **128**, **195**] On metal surfaces, chemisorbed oxygen (O*) is commonly suggested to facilitate both methanol activation to CH_3O* and the generation of HCHO* through H elimination of CH_3O*. [**190**] Figure 4.5 depicts the change in Gibbs free energy over the reaction coordinate for the steps described above from the initial state of a Pd(111) surface with adsorbed HCHO* and CH_3O*. Surface coupling occurs through interaction of the electron-dense oxygen in CH_3O* and the electron-deficient carbon in HCHO*, which results in CH_3OCH_2O*. Dehydrogenation of both CH_3OCH_2O* [**160**] and methoxymethanol [**101**] has been invoked for the production of MF. Dehydrogenation of CH_3OCH_2O* to MF is presumed to occur here oxidatively through abstraction by O* because it has been shown that chemisorbed oxygen plays a crucial role in MF generation over supported [**185**] and unsupported [**74**] Pd. We presume the formation of methoxymethanol from CH_3OCH_2O* originates from hydrogenation by nearby H* species; other hydrogenation pathways may be possible but were not considered in this study. Overall, these results imply that desorption of methoxymethanol is feasible in the experimental conditions. The known sensitivity of these reactions to coverage of chemisorbed species suggests that further insights could be generated by a detailed microkinetic model, which is beyond the scope of this Letter.

Extension to Additional Catalytic Systems and Conclusions. As discussed above, Pd-based catalysts, including oxide-supported Pd nanoparticles, [**21**, **30**, **34**, **101**, **150**, **171**, **184**, **186**, **187**] are

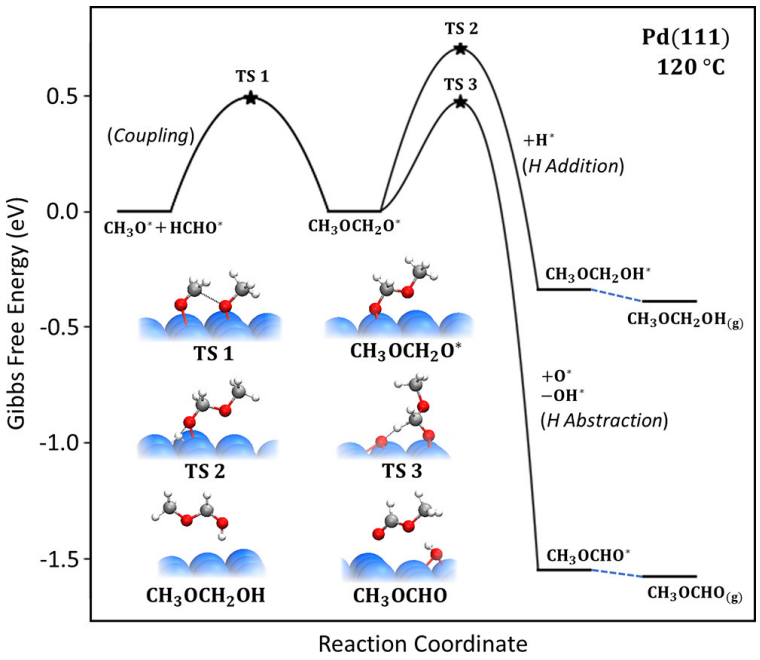

FIGURE 4.5. DFT-calculated Gibbs free energy change over the reaction coordinate for formation of methoxymethanol and methyl formate through coupling of adsorbed methoxy and formaldehyde. See Appendix 4.3.5 for details.

among the most commonly investigated materials for selective methanol oxidation. Au_xPd_y alloys are also frequently employed as active components in catalysts for this reaction [**28**, **36**, **177**, **182**, **188**] because the high miscibility of Au and Pd yields a wide composition space that can be used to control the binding strengths/interactions of adsorbates–through both ligand and ensemble effects [**44**]–which can be leveraged to optimize yields of desired products. Motivated by these prior reports, and to ensure that our observation of methoxymethanol extends to systems consistent with those used in the literature, we performed a series of isothermal catalysis experiments on additional Pd-containing catalysts: AuPd, $AuPd_2$, Au_2Pd, and MgO-supported Pd. Using MBMS to probe the near-surface region during reaction, these experiments confirmed that methoxymethanol is formed when each of these catalysts is used (Figure 4.10). Figure 4.10 also includes a representative spectrum recorded with use of Ag, a catalytic system we recently investigated using near-surface MBMS, [**200**] which shows clearly the formation of near-surface methoxymethanol. These observations reinforce the finding that methoxymethanol is a universal product of methanol

oxidation when Pd-based catalysts are used, and suggest that this species is produced with use of other material systems as well.

To highlight the important relationship between catalyst composition and the generation of methoxymethanol and other C_2^+ products, we performed temperature-dependent MBMS studies on AuPd and $AuPd_2$. Figure 4.6 provides the resulting signals associated with methoxymethanol and MF, represented as a bar chart, for Pd, $AuPd_2$, and AuPd catalysts. In this chart, the integrated product peaks were SF(T)-corrected and divided by the integrated signal for CO_2 to normalize for selectivity with respect to the competing side reaction of complete methanol oxidation, in both a low local methanol conversion regime (1–3%) and moderate local conversion regime (10–12%). Here, local conversion (η_{local}) is adapted from a definition used previously [**117**] to represent the percent decrease in methanol concentration resulting from its consumption by reaction at the position of the sampling nozzle (see Appendix 4.3.5 for definition). Within each panel (i.e., for the indicated species–methoxymethanol or MF), ratios of product signals among catalysts and between local conversion regimes can be quantitatively analyzed. Temperature dependences of ion signals associated with use of AuPd and $AuPd_2$ are provided in Figure 4.11.

Analysis of product speciation in the low-temperature (low conversion) regime shows a tendency toward greater selectivities toward oxygenates (reflected by greater oxygenate/CO_2 ratio) than at higher temperatures, which facilitate deeper oxidation toward CO_2, as expected. Interestingly, the amounts of methoxymethanol and MF produced with respect to CO_2 follow the same trend across the catalysts examined ($AuPd_2$ > AuPd > Pd). This greater selectivity toward oxygenates versus CO_2 associated with $AuPd_2$ catalysts is notable, and we will explore the mechanism behind this observation in the future. Overall, these similar trends over different catalyst surfaces provide some additional evidence that methoxymethanol and MF production are related through the mechanistic steps described throughout this Letter.

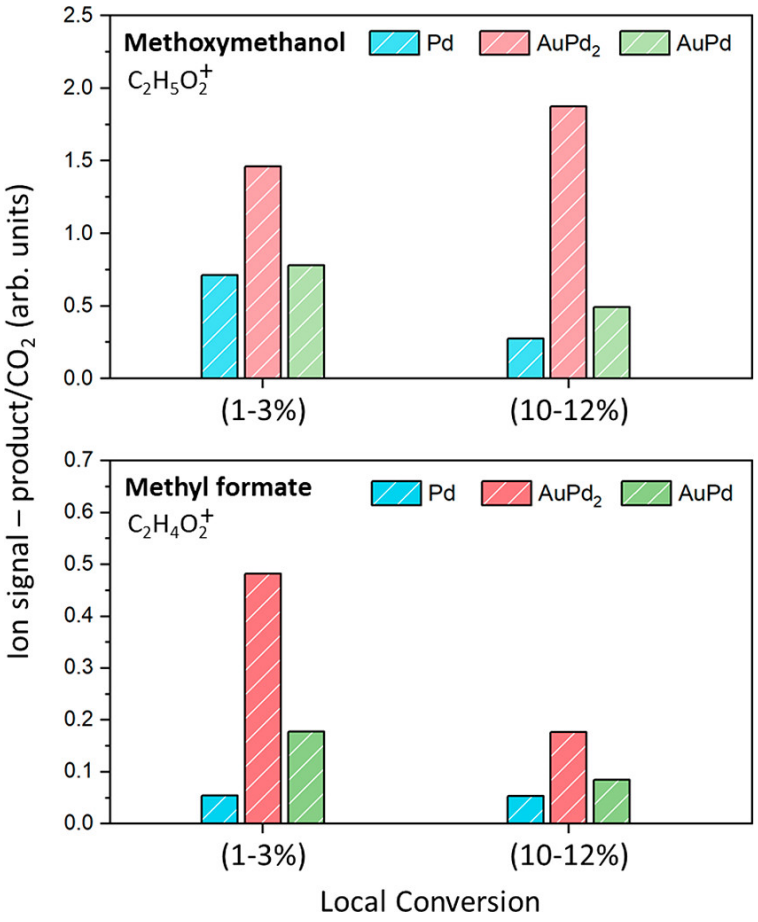

FIGURE 4.6. Ion signals associated with near-surface gas-phase methoxymethanol (top) and methyl formate (bottom) during methanol oxidation over Pd, $AuPd_2$, and AuPd, represented by respective integrated SF-corrected species signals divided by that of CO_2. Results from analyses of both the low-temperature regime (120–140 °C), associated with a local methanol conversion range of 1–3%, and from a higher temperature regime (180–200 °C), associated with a local conversion range of 10–12%, are included. P = 600 Torr; reactant feed ratio CH_3OH/O_2 = 0.07; sampling nozzle located 500 μm above the surface; 17 eV electron energy.

4.3.4. Conclusions. The findings in this Letter motivate future studies to investigate the role of catalyst composition and structure on methoxymethanol yields, as well as more in-depth analyses of the role of this intermediate within the methanol oxidation reaction network. More generally, the presented results imply that the primary products of oxygenate coupling events during methanol oxidation catalysis may not be reflected in the compositions of reactor effluents analyzed through conventional methods. Efforts to design new methanol oxidation catalysts and to develop microkinetic models describing the reaction network should account for the formation,

desorption, adsorption, and surface reactions of methoxymethanol. These insights will contribute to ongoing efforts to optimize catalytic systems for conversion of methanol to targeted chemicals with improved selectivity and yield.

4.3.5. Appendix.

4.3.5.1. *Experimental Methods.* **Molecular-beam time-of-flight mass spectrometry**

A schematic representation and details of the MBMS system used for near-surface species detection have been provided in previous publications. [**122**, **200**]

Briefly, the instrument consists of a reactor chamber that is connected to a high-resolution reflectron time-of-flight mass spectrometer (RTOF-MS) via a quartz sampling probe. A molecular beam is obtained by a two-stage pumped vacuum system providing a sudden pressure drop from near-atmospheric pressure in the reactor to high vacuum conditions (10^{-6} Torr) in the ionization chamber. This molecular beam, which prevents any further interactions among molecules, improves the detection capabilities of the local measurement to such a level that even highly reactive species, such as free radicals, can be detected.

The temperature-corrected integrated ion signal is a function of the partial pressure of the feed gases at a certain position, d, and can be formulated as:

$$S_i[E, d, T^s, T^g(d, T^s)] = const \times SF(T^g) \times x_i(d, T^s, T^g) \times SW \times D_i \times \phi \times \int \sigma \times f(E - E^{'})\mathrm{d}E^{'} \quad (4.1)$$

where $x_i(d, T^s, T^g)$ is the mole fraction of species i, SW is the number of sweeps, D_i is the mass discrimination factor, ϕ is the number of ionizing electrons per unit time, E is the most probable energy of the ionizing electrons, d is the distance of the probe from the surface, T^s is the surface temperature, T^g (d,T^s) the gas-phase temperature, const and SF(T^g) are an instrument and a gas-phase temperature-dependent sampling function, respectively. σ_i (E) is the ionization cross section, and f(E-$E^{'}$) is the energy distribution function of the ionizing electrons.

Reactor conditions

Conditions were described in a recent publication. [**200**] Catalysts were secured to boron nitride electric heaters in the reactor chamber. A thermocouple was attached to the surface of the film to record temperature. The pressure of the reactor chamber was kept at 600 Torr and methanol vapor was flowed through the reactor by bubbling N_2 through liquid methanol maintained at room

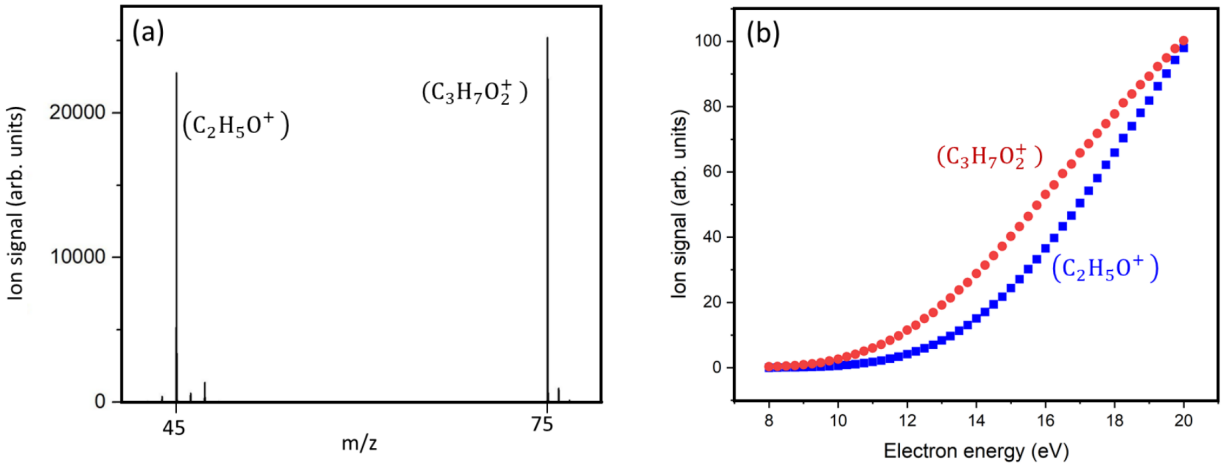

FIGURE 4.7. Representative mass spectrometry results during flow of dimethoxymethane. (a) Spectrum recorded with 17 eV electron energy; (b) Electron energy dependence of signals of m/z 45 and 75.

temperature. The value of η_{local} was calculated by of $\eta_{local}=((X_{M,RT}-X_{M,T}))/X_{M,RT}$, where X_M is the integrated temperature-corrected ion signal of methanol, and RT and T refer to measurements made with the sample at room temperature (at which no reaction occurs) and the sample at reaction temperatures, respectively.

Representative energy-dependent ion signals: dimethoxymethane

Figure 4.7 provides representative mass spectrometry results during flow of dimethoxymethane showing fragment ions from dissociative ionization at electron kinetic energy 17 eV (Fig. 4.7a) and the electron kinetic energy dependences of the signals for these primary fragment ions (Fig. 4.7b).

Correction of ion signals

Gas calibration facilitates determination of the quantity $const \times SF(T^g) \times x_i(d, T^s, T^g) \times SW \times D_i \times \phi \times \int \sigma \times f(E-E')\mathrm{d}E'$ with a pre-set number of sweeps. Equation 4.1 can be simplified to Equation 4.2 below by comparing the signals to those of a reference species j:

$$\frac{S_i}{S_j} = \frac{x_i}{x_j} \times \frac{D_i}{D_j} \times \frac{\int \sigma_i \times f(E-E')\mathrm{d}E'}{\int \sigma_j \times f(E-E')\mathrm{d}E'} = \frac{x_i}{x_j} \times k_{\frac{i}{j}}(E) = \frac{n_i}{n_j} \times k_{\frac{i}{j}}(E) \tag{4.2}$$

Where $_{\frac{i}{j}}(E)$ in 4.2 is an energy-dependent calibration factor that can be used to compare the signal to that of a reference species quantitively. Figure 4.8 provides representative results from experiments with known species compositions that have been referenced to an inert gas (N_2)

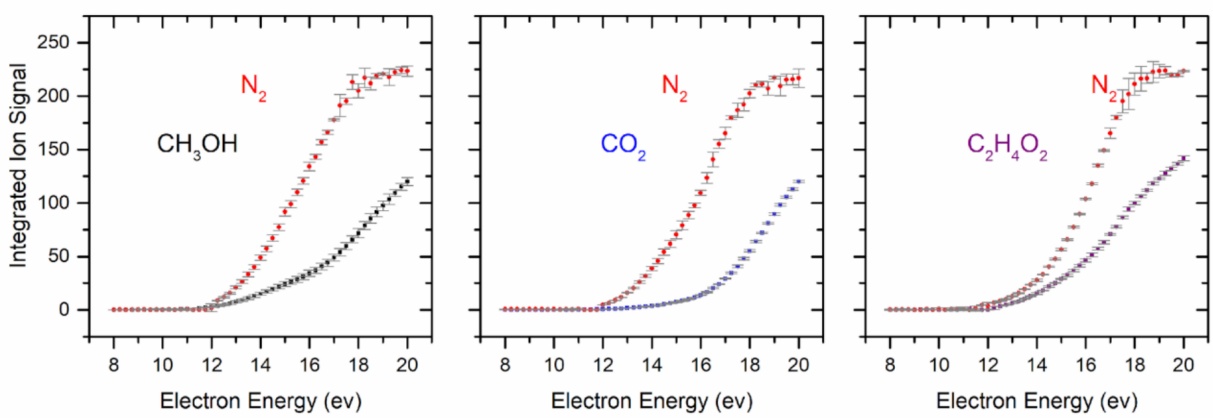

FIGURE 4.8. Cold gas calibrations. Integrated ion signals as a function of electron energy for different gases referenced to an inert gas (N_2).

to calculate the calibration factors for each of the indicated species. Independent measurements were performed for electron energies between 8-20 eV. The energy-dependent calibration factor was obtained by dividing each of the product signals to that of the reference species N_2.

Catalyst synthesis and reaction conditions

The metal and metal alloy films were sputtered using a commercial magnetron sputtering system (AJA International) onto single-crystal Si (001) (University Wafer) held at 200 °C. Prior to deposition, a 500-micron thick silicon disk was cut into 7×30 mm pieces. The pieces were sequentially rinsed with Milli-Q water and acetone and air-dried. Pd and Au targets (AJA International, Inc.; 99.99%) were used for the deposition of polycrystalline metal layers. Films with a thickness of 150 nm were deposited by DC magnetron co-sputtering. The deposition rate was measured through control experiments by placing a quartz crystal microbalance in the exact position of the sample holder, with deposition occurring in identical conditions. The compositions of the metal films were controlled by varying the DC power and the deposition time. To enhance the adhesion of the metal layer, the Si substrate was lightly sputtered with Ar^+ to remove the native Si oxide and a 5 nm Ti underlayer was deposited prior to catalyst deposition. The deposition was performed in an Ar atmosphere with pressure controlled at 5 × 10-3 torr. Pd/MgO (1 wt%) was prepared by wet impregnation, adapting a procedure described in a previous report. [**10**] Briefly, acidified $PdCl_2$ solution (with dilute HCl) was injected and stirred into a solution of containing MgO nanoparticles

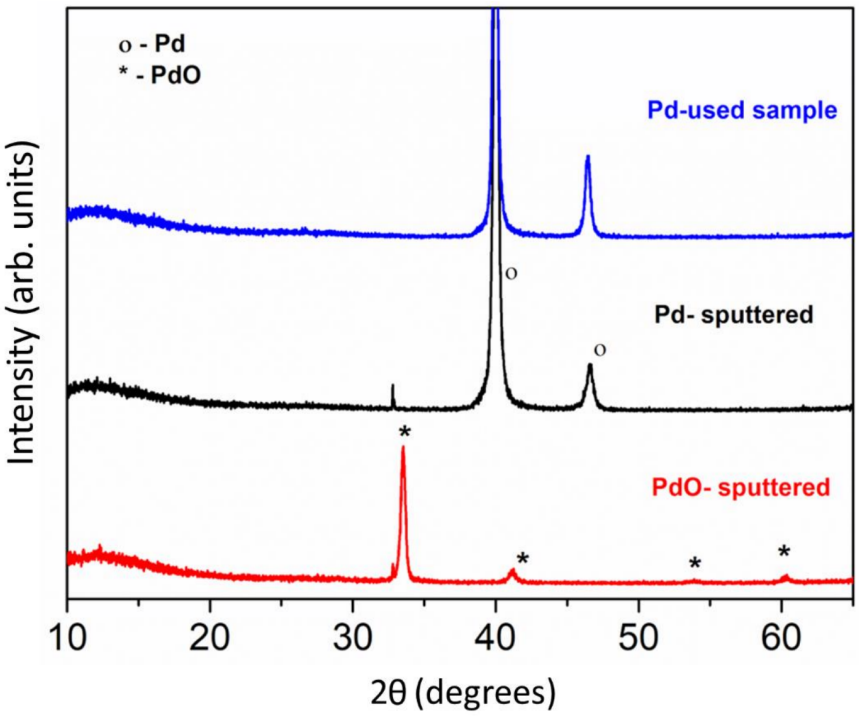

FIGURE 4.9. X-ray diffractograms associated with Pd films deposited on Si(001) used in this study, compared to a reference PdO film deposited with reactive O_2 in the background.

(100 nm) at 50 °C for 5 h. The resulting catalyst paste was dried in an oven overnight. The catalyst later was calcined at 700 °C for 6 h under O_2/N_2 (1/4) flow.

4.3.6. Additional Results.

4.3.6.1. *X-ray diffraction.* Figure 4.9 provides X-Ray diffractograms for Pd films utilized in this study.

4.3.6.2. *Mass spectrometry.* Figure 4.10 provides representative mass spectra associated with methanol oxidation in experiments using the other catalysts considered in this report. The presence of methoxymethanol is evident.

Figure 4.11 provides the temperature dependences of the integrated ion signals associated with the reaction over AuPd and $AuPd_2$ catalysts.

4.3.6.3. *Calculations Using Density Functional Theory.* Periodic DFT calculations were performed using the Vienna Ab-initio Simulation Package (VASP) using a plane-wave cut-off of 400 eV, a $4 \times 4 \times 1$ Monkhorst-Pack k-point mesh, and the revised Perdew-Burke-Ernzerhof (RPBE)

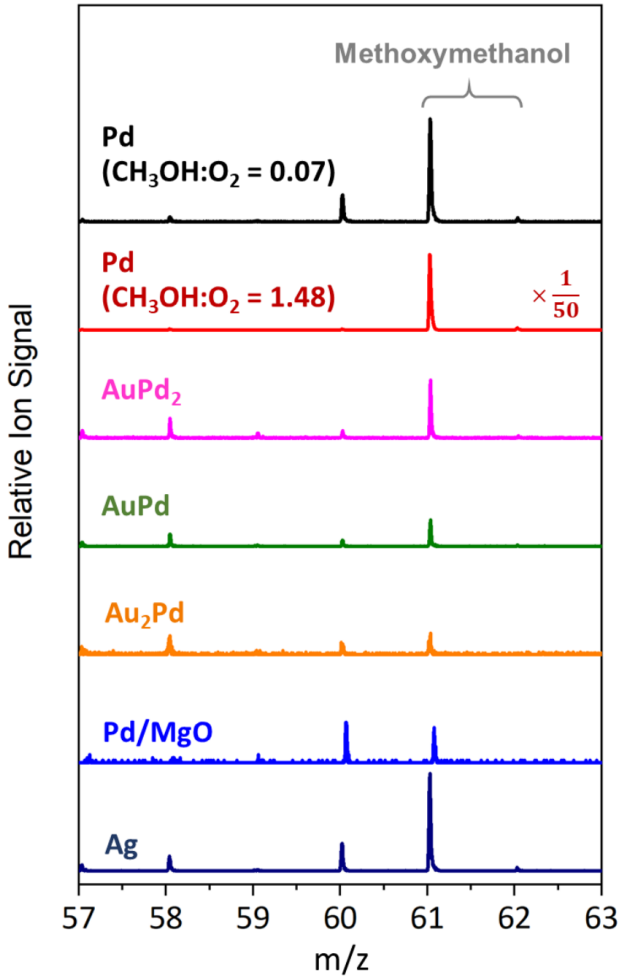

FIGURE 4.10. Representative mass spectra between m/z = 55-65 recorded in the near-surface region above other catalysts considered in this report, in conditions similar to those presented in the main text. Ag is included for reference and is associated our previously published results. [**200**]

functional. [**84**,**85**,**86**,**87**,**153**] The Atomic Simulation Environment [**94**] code was used in combination with VASP. Electronic cores were represented with PAW PBE pseudopotentials. [**88**] Geometry optimizations were performed until the force on each atom was < 0.05 eV Å^{-1} and the energy convergence criterion of 1×10^{-6} eV was reached. A Pd(111) surface was modeled using a $3 \times 3 \times 4$ slab; the bottom two layers of the slab were constrained while the top two layers were allowed to relax. A vacuum of 12 Å was utilized to prevent spurious interaction between periodic images of the structures. Transition states were determined using a combination of the climbing nudged elastic

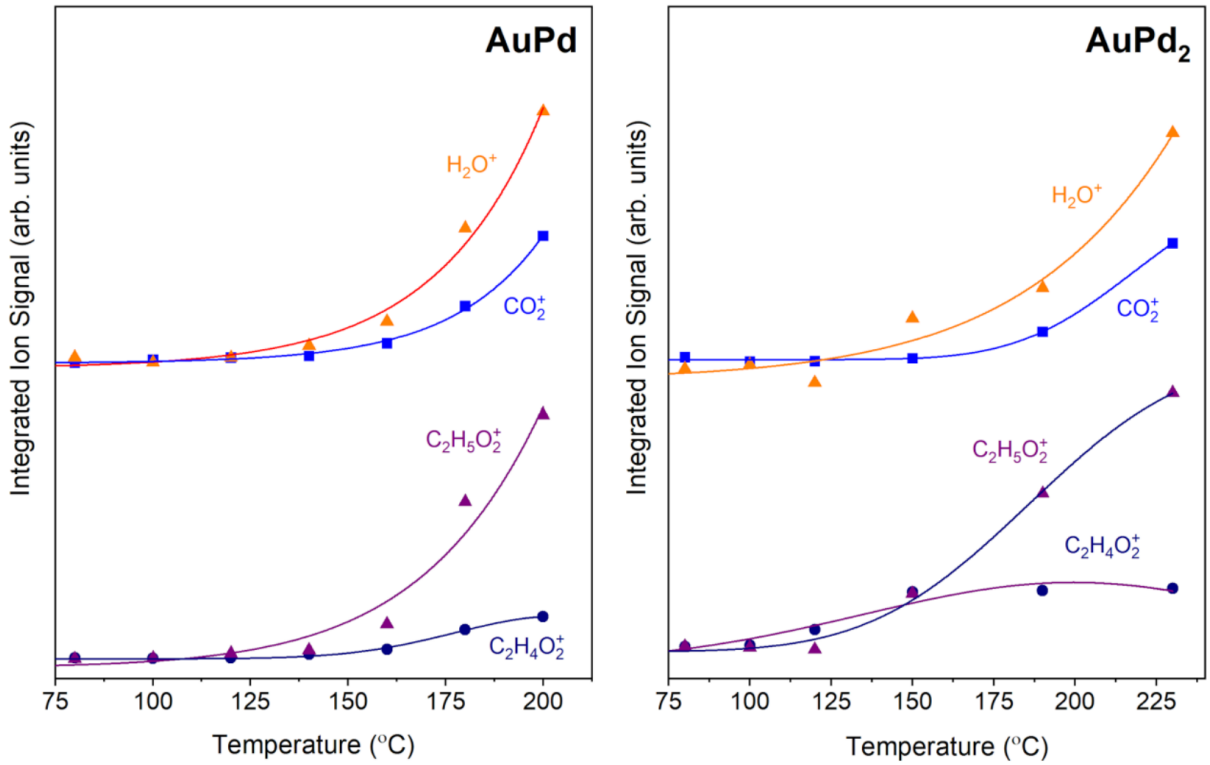

FIGURE 4.11. Temperature dependences of integrated ion signals of CO_2^+, H_2O^+, $C_2H_4O_2^+$, $C_2H5O_2^+$ associated with oxidative methanol conversion over (a) AuPd and (b) AuPd2. P = 600 torr; reactant feed ratio $CH_3OH/O_2 = 0.07$; inlet nozzle located 500 μm above the surface.

band [**63**] and dimer methods. [**62**] Vibrational modes and frequencies were determined using the finite difference method to calculate the Hessian matrix. Vibrational calculations were performed until the force on each atom was < 0.05 eV Å^{-1} and the energy convergence criterion of 1×10^{-7} eV was reached. Free energies were calculated using the harmonic approximation. Key DFT-optimized geometries of atomistic models are shown in Figure 4.5 in the main text. Reaction barriers and the free energy differences are displayed in Table 4.1.

TABLE 4.1. Reaction barriers and the free energy differences associated with Figure 3 in the main text.

	Mechanism	$\Delta E^{\ddagger}_{DFT}$	ΔE^{tot}_{DFT}	$\Delta G^{\ddagger}_{120^{\circ}C}$	$\Delta G^{tot}_{120^{\circ}C}$
Methoxymethanol formation	$CH_3O^* + CH_2O^* \leftrightarrow CH_3OCH_2O^*$	0.23	-0.42	0.49	0.00
	$CH_3OCH_2O^* + H^* \leftrightarrow CH_3OCH_2OH^*$	0.67	-0.52	0.70	-0.34
	$CH_3OCH_2OH^* \leftrightarrow CH_3OCH_2OH + *$	-	0.03	-	-0.05
Methyl formate (MF) formation	$CH_3OCH_2O^* + * \leftrightarrow CH_3OCHO^* + H^*$	0.15	-1.17	0.06	-1.64
	$CH_3OCH_2O^* + O^* \leftrightarrow CH_3OCHO^* + OH^*$	0.59	-1.31	0.47	-1.55
	$CH_3OCH_2O^* + OH^* \leftrightarrow CH_3OCHO^* + H_2O^*$	0.37	-1.63	0.30	-2.08
	$CH_3OCHO^* \leftrightarrow CH_3OCHO + *$	-	0.05	-	-0.02

* Indicates a surface-bound species or a bare Pd site $\Delta E^{\ddagger}_{DFT}$ = transition state – initial state (calculated at 0 K with no ZPE correction) ΔE^{tot}_{DFT} = final state – initial state (calculated at 0 K with no ZPE correction) $\Delta G^{\ddagger}_{120^{\circ}C}$ = transition state – initial state (calculated using the harmonic approximation) $\Delta G^{tot}_{120^{\circ}C}$ = final state – initial state (calculated using harmonic approximation)

4.4. Appendix

4.4.1. Oxidative coupling of methane. After adapting the near surface gas-phase diagnostic techniques to oxidative coupling of methane reaction, we tested our system with a well-studied OCM catalyst, Li/MgO, to contrast MBMS data (at Sandia) with the data collected in a tubular reactor coupled to a gas chromatography (at UC Davis). Reaction conditions involving feed ratio, temperature and space velocity was aimed to be consistent for a reasonable comparison. Figure 4.12 shows the MBMS spectrums at different total flow rates of methane-oxygen mixtures.

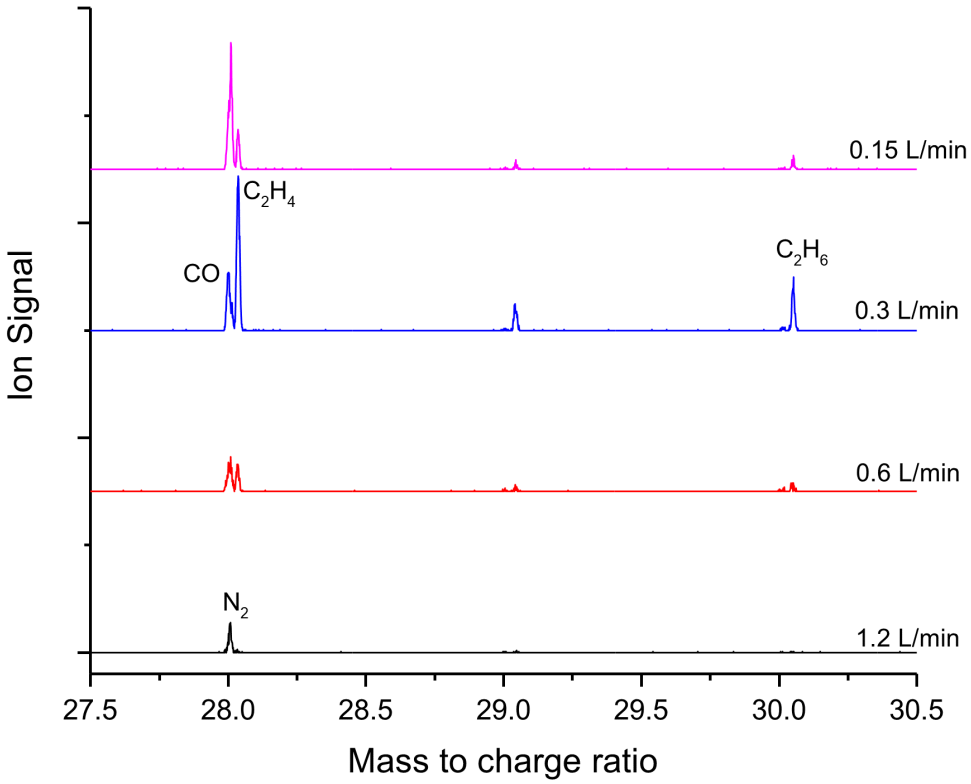

FIGURE 4.12. Representative mass spectra between m/z = 27-30 recorded at different flow rates in the near-surface region above Li/MgO. P = 600 torr; T = 700 °C; Reactant feed = Ar (85%), CH_4 (10%), O_2 (5%); inlet nozzle located 500 μm above the surface.

An optimum total flow rate (0.3 L/min) was determined and the further experiments were performed at this flow rate. Figure 4.13 demonstrates the temperature dependence of OCM reaction for methane coupling and oxidation products. Preliminary data collected here well agreed with the data obtained with in a tubular reactor which indicates the competence of modified MBMS

technique for the OCM reaction. Yet, future studies are needed for gaining more mechanistic information regarding the OCM reaction including detecting the radicals and more exotic species. The experiments are still in progress and promising results are expected to be produced soon.

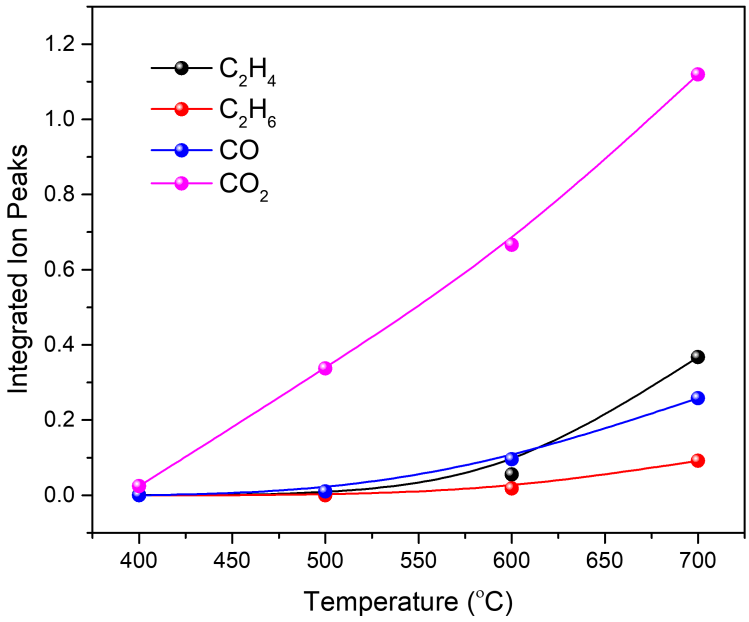

FIGURE 4.13. The surface temperature dependence of the integrated mass spectral signal for methane oxidation products CO and CO_2 and methane coupling products C_2H_4 and C_2H_6.

CHAPTER 5

Conclusion

The need for developing technologies to utilize the natural gas sources more efficiently has accelerated the researches on the direct conversion methods of light alkanes. Three different catalysis systems that consist liquid-phase thermal (homogeneous), electrochemical (heterogeneous) and gas-phase thermal (homogeneous and heterogeneous) catalysis have been proposed as the direct conversion routes for upgrading light alkanes presence in natural gas. Here in this dissertation, we have explored various light alkane activation systems by engineering the required experimental set-ups which contributed to the content of this thesis and will potentially contribute to the future success of upcoming studies in our laboratory. We first started with a relatively simple system, which requires a catalyst slurry (AuPd) and a strong oxidant (H_2O_2), is well covered in Chapter 2. Derived from the main results, we proposed that the continuous supply of low concentrated H_2O_2 to the reactor system might be able to make the overall process of direct light alkane upgrading industrially viable. As a follow up study, at the beginning of Chapter 3, a highly H_2O_2 selective electrocatalyst was designed to serve the purpose of efficient H_2O_2 production. The requirement of a well designed reactor for coupling H_2O_2 production and light alkane oxidation inspired us to benchmark our abilities for the fundamental analysis of electrochemical methane oxidation which later helped the design of hybrid (thermal and electrochemical) reactor (1.4) as mentioned above. Chapter 3.3 presents the results obtained from the investigation of Pt suface with methane under an electrochemical potential. Our Operando SEIRAS and cyclic voltammetry experiments revealed that the defects or step-edges over the polycrystalline Pt surface are the active sites for the initial C-H bond activation. This hypothesis was supported by investigating the effect of various potentials and pHs on the oxidation of methane. The studies performed in Chapter 2 and 3 could serve as the basis for experimental approaches to develop optimized the conditions for the liquid-phase light alkane upgrading and accordingly might benefit the future studies.

In Chapter 4, we proposed to investigate a rather complex system named as oxidative coupling of methane. To fill the fundamental knowledge gap in the field of OCM, we have collaborated Sandia National Laboratories. 2-D laser-induced fluorescence (LIF) and molecular beam mass spectrometry (MBMS) were employed for the near-surface gas-phase analysis over a catalyst surface. First, these two techniques were optimized and tested for partial methanol oxidation on Ag surface. The output of this study motivated us to investigate the same reaction on different metal surfaces. Accordingly, a magnetron sputtered Pd was prepared and investigated for methanol oxidation. A significant intermediate, methoxymethanol, was probed by the MBMS measurement. The effects of different temperatures and feed ratio were also investigated to further understand the role of methoxymethanol in the overall reaction network. We believe that these insights will contribute to ongoing efforts to optimize catalytic systems for partial oxidation of methanol. Further studies on partial oxidation of methanol were also performed on supported catalyst but the current results were not included in this dissertation. As stated before, the overall system was tested and prepared to perform experiments for oxidative coupling of methane. Our initial results on OCM showed the applicability of these near-surface diagnostic techniques on a complex reaction as OCM. We are currently tuning our system for the detection of radicals and more interesting intermediates presence in the near-surface gas region during OCM. These insights would significantly improve the understanding of the fundamentals of OCM reaction and serve a great value for engineering new catalysts.

Bibliography

[1] *Natural gas explained, use of natural gas.* https://www.eia.gov/energyexplained/natural-gas/use-of-natural-gas.php#:~:text=The%20United%20States%20used%20about,of%20U.S.%20total%20energy%20consumption., Dec. 2021.

[2] *Annual energy outlook 2022 eia.* https://www.eia.gov/outlooks/aeo/narrative/production/sub-topic-01.php, May 2022.

[3] *Where our natural gas comes from.* https://www.eia.gov/energyexplained/natural-gas/where-our-natural-gas-comes-from.php, 2022.

[4] N. Agarwal, S. J. Freakley, R. U. McVicker, S. M. Althahban, N. Dimitratos, Q. He, D. J. Morgan, R. L. Jenkins, D. J. Willock, S. H. Taylor, et al., *Aqueous au-pd colloids catalyze selective ch4 oxidation to ch3oh with o2 under mild conditions*, Science, 358 (2017), pp. 223–227.

[5] S. Al-Shihri, C. J. Richard, and D. Chadwick, *Selective oxidation of methane to methanol over zsm-5 catalysts in aqueous hydrogen peroxide: Role of formaldehyde*, ChemCatChem, 9 (2017), pp. 1276–1283.

[6] R. D. Armstrong, S. J. Freakley, M. M. Forde, V. Peneau, R. L. Jenkins, S. H. Taylor, J. A. Moulijn, D. J. Morgan, and G. J. Hutchings, *Low temperature catalytic partial oxidation of ethane to oxygenates by fe–and cu–zsm-5 in a continuous flow reactor*, Journal of Catalysis, 330 (2015), pp. 84–92.

[7] R. D. Armstrong, G. J. Hutchings, and S. H. Taylor, *An overview of recent advances of the catalytic selective oxidation of ethane to oxygenates*, Catalysts, 6 (2016), p. 71.

[8] L. Arnarson, P. S. Schmidt, M. Pandey, A. Bagger, K. S. Thygesen, I. E. Stephens, and J. Rossmeisl, *Fundamental limitation of electrocatalytic methane conversion to methanol*, Physical Chemistry Chemical Physics, 20 (2018), pp. 11152–11159.

[9] O. Ayemoba and A. Cuesta, *Spectroscopic evidence of size-dependent buffering of interfacial ph by cation hydrolysis during co2 electroreduction*, ACS applied materials & interfaces, 9 (2017), pp. 27377–27382.

[10] H. P. Aytam, V. Akula, K. Janmanchi, S. R. R. Kamaraju, K. R. Panja, K. Gurram, and J. Niemantsverdriet, *Characterization and reactivity of pd/mgo and pd/γ-al2o3 catalysts in the selective hydrogenolysis of ccl2f2*, The Journal of Physical Chemistry B, 106 (2002), pp. 1024–1031.

[11] T. Baba and A. Miyaji, *Catalysis and the Mechanism of Methane Conversion to Chemicals*, Springer, 2020.

[12] M. Badlani and I. E. Wachs, *Methanol: a "smart" chemical probe molecule*, Catalysis Letters, 75 (2001), pp. 137–149.

[13] V. Bagotzky, Y. B. Vassiliev, and O. Khazova, *Generalized scheme of chemisorption, electrooxidation and electroreduction of simple organic compounds on platinum group metals*, Journal of Electroanalytical Chemistry and Interfacial Electrochemistry, 81 (1977), pp. 229–238.

[14] S. Bai, F. Liu, B. Huang, F. Li, H. Lin, T. Wu, M. Sun, J. Wu, Q. Shao, Y. Xu, et al., *High-efficiency direct methane conversion to oxygenates on a cerium dioxide nanowires supported rhodium single-atom catalyst*, Nature communications, 11 (2020), pp. 1–9.

[15] P. B. Balbuena and V. R. Subramanian, *Theory and experiment in electrocatalysis*, Springer, 2010.

[16] M. Baldea, T. F. Edgar, B. L. Stanley, and A. A. Kiss, *Modular manufacturing processes: Status, challenges, and opportunities*, AIChE journal, 63 (2017), pp. 4262–4272.

[17] B. Beden, F. Hahn, J.-M. Leger, C. Lamy, and M. I. dos Santos Lopes, *"in situ" infrared reflectance spectroscopic study of the adsorbed species resulting from ch3oh adsorption on polycrystalline pt in acid solution*, Journal of electroanalytical chemistry and interfacial electrochemistry, 258 (1989), pp. 463–467.

[18] B. Beden, C. Lamy, N. De Tacconi, and A. J. Arvia, *The electrooxidation of co: a test reaction in electrocatalysis*, Electrochimica acta, 35 (1990), pp. 691–704.

[19] A. E. Bjerke, P. R. Griffiths, and W. Theiss, *Surface-enhanced infrared absorption of co on platinized platinum*, Analytical Chemistry, 71 (1999), pp. 1967–1974.

[20] M. Bobeldijk, W. Van der Zande, and P. Kistemaker, *Simple models for the calculation of photoionization and electron impact ionization cross sections of polyatomic molecules*, Chemical physics, 179 (1994), pp. 125–130.

[21] M. Borasio, O. Rodríguez de la Fuente, G. Rupprechter, and H.-J. Freund, *In situ studies of methanol decomposition and oxidation on pd (111) by pm-iras and xps spectroscopy*, The Journal of Physical Chemistry B, 109 (2005), pp. 17791–17794.

[22] M. J. Boyd, A. A. Latimer, C. F. Dickens, A. C. Nielander, C. Hahn, J. K. Nørskov, D. C. Higgins, and T. F. Jaramillo, *Electro-oxidation of methane on platinum under ambient conditions*, ACS Catalysis, 9 (2019), pp. 7578–7587.

[23] M. Breiter, *On the nature of reduced carbon dioxide*, Electrochimica Acta, 12 (1967), pp. 1213–1218.

[24] P. Casavecchia, F. Leonori, N. Balucani, R. Petrucci, G. Capozza, and E. Segoloni, *Probing the dynamics of polyatomic multichannel elementary reactions by crossed molecular beam experiments with soft electron-ionization mass spectrometric detection*, Physical Chemistry Chemical Physics, 11 (2009), pp. 46–65.

[25] H. Chadwick, H. Guo, A. Gutiérrez-González, J. P. Menzel, B. Jackson, and R. D. Beck, *Methane dissociation on the steps and terraces of pt (211) resolved by quantum state and impact site*, The Journal of Chemical Physics, 148 (2018), p. 014701.

[26] H. Y. H. Chan, C. T. Williams, M. J. Weaver, and C. G. Takoudis, *Methanol oxidation on palladium compared to rhodium at ambient pressures as probed by surface-enhanced raman and mass spectroscopies*, Journal of Catalysis, 174 (1998), pp. 191–200.

[27] C. D. Chang, *Hydrocarbons from methanol*, Catalysis Reviews Science and Engineering, 25 (1983), pp. 1–118.

[28] C.-R. Chang, B. Long, X.-F. Yang, and J. Li, *Theoretical studies on the synergetic effects of au–pd bimetallic catalysts in the selective oxidation of methanol*, The Journal of Physical Chemistry C, 119 (2015), pp. 16072–16081.

[29] I. P. O. C. Change, *Climate change 2007: the physical science basis*, Agenda, 6 (2007), p. 333.

[30] X. Chen, Y. Liu, M. Guo, et al., *Effects of support on performance of methanol oxidation over palladium-only catalysts*, Water, Air, & Soil Pollution, 231 (2020), pp. 1–12.

[31] X. Chen, I. T. McCrum, K. A. Schwarz, M. J. Janik, and M. T. Koper, *Co-adsorption of cations as the cause of the apparent ph dependence of hydrogen adsorption on a stepped platinum single-crystal electrode*, Angewandte Chemie, 129 (2017), pp. 15221–15225.

[32] P. Christensen, A. Hamnett, J. Munk, and G. Troughton, *An in situ ftir study of the electrochemical oxidation of methanol at small platinum particles*, Journal of Electroanalytical Chemistry, 370 (1994), pp. 251–258.

[33] M. A. Climent, M. J. Valls, J. M. Feliu, A. Aldaz, and J. Clavilier, *The behaviour of platinum single-crystal electrodes in neutral phosphate buffered solutions*, Journal of Electroanalytical Chemistry, 326 (1992), pp. 113–127.

[34] M. Cubeiro and J. L. G. Fierro, *Partial oxidation of methanol over supported palladium catalysts*, Applied Catalysis A: General, 168 (1998), pp. 307–322.

[35] A. Cuesta, A. Couto, A. Rincon, M. C. Pérez, A. Lopez-Cudero, and C. Gutiérrez, *Potential dependence of the saturation co coverage of pt electrodes: The origin of the pre-peak in co-stripping voltammograms. part 3: Pt (poly)*, Journal of Electroanalytical Chemistry, 586 (2006), pp. 184–195.

[36] K. Czelej, K. Cwieka, J. C. Colmenares, and K. J. Kurzydlowski, *Insight on the interaction of methanol-selective oxidation intermediates with au-or/and pd-containing monometallic and bimetallic core@ shell catalysts*, Langmuir, 32 (2016), pp. 7493–7502.

[37] B. Demirata-Öztürk, G. Özen, H. Filik, I. Tor, and H. Afsar, *Spectrofluorometric determination of hydrogen peroxide*, Journal of Fluorescence, 8 (1998), pp. 185–189.

[38] M. Dunwell, J. Wang, Y. Yan, and B. Xu, *Surface enhanced spectroscopic investigations of adsorption of cations on electrochemical interfaces*, Physical Chemistry Chemical Physics, 19 (2017), pp. 971–975.

[39] J. K. Edwards, S. J. Freakley, A. F. Carley, C. J. Kiely, and G. J. Hutchings, *Strategies for designing supported gold–palladium bimetallic catalysts for the direct synthesis of hydrogen peroxide*, Accounts of chemical research, 47 (2014), pp. 845–854.

[40] J. K. Edwards and G. J. Hutchings, *Palladium and gold–palladium catalysts for the direct synthesis of hydrogen peroxide*, Angewandte Chemie International Edition, 47 (2008), pp. 9192–9198.

[41] M. J. Farias, W. Cheuquepán, A. A. Tanaka, and J. M. Feliu, *Identity of the most and least active sites for activation of the pathways for co2 formation from the electro-oxidation of methanol and ethanol on platinum*, ACS Catalysis, 10 (2019), pp. 543–555.

[42] M. M. Forde, R. D. Armstrong, C. Hammond, Q. He, R. L. Jenkins, S. A. Kondrat, N. Dimitratos, J. A. Lopez-Sanchez, S. H. Taylor, D. Willock, et al., *Partial oxidation of ethane to oxygenates using fe-and cu-containing zsm-5*, Journal of the American Chemical Society, 135 (2013), pp. 11087–11099.

[43] S. L. Foster, S. I. P. Bakovic, R. D. Duda, S. Maheshwari, R. D. Milton, S. D. Minteer, M. J. Janik, J. N. Renner, and L. F. Greenlee, *Catalysts for nitrogen reduction to ammonia*, Nature Catalysis, 1 (2018), pp. 490–500.

[44] F. Gao and D. W. Goodman, *Pd–au bimetallic catalysts: understanding alloy effects from planar models and (supported) nanoparticles*, Chemical Society Reviews, 41 (2012), pp. 8009–8020.

[45] N. Garcia-Araez, *Enthalpic and entropic effects on hydrogen and oh adsorption on pt (111), pt (100), and pt (110) electrodes as evaluated by gibbs thermodynamics*, The Journal of Physical Chemistry C, 115 (2011), pp. 501–510.

[46] A. T. Gee, B. E. Hayden, C. Mormiche, A. W. Kleyn, and B. Riedmüller, *The dynamics of the dissociative adsorption of methane on pt (533)*, The Journal of chemical physics, 118 (2003), pp. 3334–3341.

[47] R. Gisbert, G. García, and M. T. Koper, *Adsorption of phosphate species on poly-oriented pt and pt (1 1 1) electrodes over a wide range of ph*, Electrochimica Acta, 55 (2010), pp. 7961–7968.

[48] R. Gómez, J. M. Orts, B. Álvarez-Ruiz, and J. M. Feliu, *Effect of temperature on hydrogen adsorption on pt (111), pt (110), and pt (100) electrodes in 0.1 m hclo4*, The Journal of Physical Chemistry B, 108 (2004), pp. 228–238.

[49] A. Govind Rajan, J. M. P. Martirez, and E. A. Carter, *Why do we use the materials and operating conditions we use for heterogeneous (photo) electrochemical water splitting?*, ACS Catalysis, 10 (2020), pp. 11177–11234.

[50] E. Grantscharova-Anderson and A. B. Anderson, *The prewave in co oxidation over roughened and sn alloyed pt surfaces: possible structure and electronic causes*, Electrochimica acta, 44 (1999), pp. 4543–4550.

[51] S. Grimme, S. Ehrlich, and L. Goerigk, *Effect of the damping function in dispersion corrected density functional theory*, Journal of computational chemistry, 32 (2011), pp. 1456–1465.

[52] S. M. Gurses and C. X. Kronawitter, *Electrochemistry of the interaction of methane with platinum at room temperature investigated through operando ftir spectroscopy and voltammetry*, The Journal of Physical Chemistry C, 125 (2021), pp. 2944–2955.

[53] S. M. Gurses, T. Price, A. Zhang, J. H. Frank, N. Hansen, D. L. Osborn, A. Kulkarni, and C. X. Kronawitter, *Near-surface gas-phase methoxymethanol is generated by methanol oxidation over pd-based catalysts*, The Journal of Physical Chemistry Letters, 12 (2021), pp. 11252–11258.

[54] A. Gutiérrez-González, M. Torio, H. Busnengo, and R. D. Beck, *Site selective detection of methane dissociation on stepped pt surfaces*, Topics in Catalysis, 62 (2019), pp. 859–873.

[55] J. Hafner, *Ab-initio simulations of materials using vasp: Density-functional theory and beyond*, Journal of computational chemistry, 29 (2008), pp. 2044–2078.

[56] F. Hahn and C. Melendres, *Anodic oxidation of methane at noble metal electrodes: an 'in situ'surface enhanced infrared spectroelectrochemical study*, Electrochimica acta, 46 (2001), pp. 3525–3534.

[57] B. Hammer, L. B. Hansen, and J. K. Nørskov, *Improved adsorption energetics within density-functional theory using revised perdew-burke-ernzerhof functionals*, Physical review B, 59 (1999), p. 7413.

[58] C. Hammond, M. M. Forde, M. H. Ab Rahim, A. Thetford, Q. He, R. L. Jenkins, N. Dimitratos, J. A. Lopez-Sanchez, N. F. Dummer, D. M. Murphy, et al., *Direct catalytic conversion of methane to methanol in an aqueous medium by using copper-promoted fe-zsm-5*, Angewandte Chemie, 124 (2012), pp. 5219–5223.

[59] J. F. Haw, W. Song, D. M. Marcus, and J. B. Nicholas, *The mechanism of methanol to hydrocarbon catalysis*, Accounts of chemical research, 36 (2003), pp. 317–326.

[60] B. Hayden, K. Kretzschmar, A. Bradshaw, and R. Greenler, *An infrared study of the adsorption of co on a stepped platinum surface*, Surface science, 149 (1985), pp. 394–406.

[61] M. Henderson, A. Szabo, and J. Yates Jr, *The structure of co on the pt (112) stepped surface—a sensitive view of bonding configurations using electron stimulated desorption*, The Journal of chemical physics, 91 (1989), pp. 7245–7254.

[62] G. Henkelman and H. Jónsson, *A dimer method for finding saddle points on high dimensional potential surfaces using only first derivatives*, The Journal of chemical physics, 111 (1999), pp. 7010–7022.

[63] G. Henkelman, B. P. Uberuaga, and H. Jónsson, *A climbing image nudged elastic band method for finding saddle points and minimum energy paths*, The Journal of chemical physics, 113 (2000), pp. 9901–9904.

[64] F. M. Hoffmann, *Infrared reflection-absorption spectroscopy of adsorbed molecules*, Surface Science Reports, 3 (1983), pp. 107–192.

[65] Y. Hori, *Modern aspects of electrochemistry-electrochemical co 2 reduction on metal electrodes*, 2008.

[66] T. Housmans, C. Hermse, and M. Koper, *Co oxidation on stepped single crystal electrodes: A dynamic monte carlo study*, Journal of Electroanalytical Chemistry, 607 (2007), pp. 69–82.

[67] H. Huang, C. Fierro, D. Scherson, and E. Yeager, *In situ fourier transform infrared spectroscopic study of carbon dioxide reduction on polycrystalline platinum in acid solutions*, Langmuir, 7 (1991), pp. 1154–1157.

[68] Y.-F. Huang, P. J. Kooyman, and M. Koper, *Intermediate stages of electrochemical oxidation of single-crystalline platinum revealed by in situ raman spectroscopy*, Nature communications, 7 (2016), pp. 1–7.

[69] T. Iwasita, F. Nart, B. Lopez, and W. Vielstich, *On the study of adsorbed species at platinum from methanol, formic acid and reduced carbon dioxide via in situ ft-ir spectroscopy*, Electrochimica acta, 37 (1992), pp. 2361–2367.

[70] P. Jacquinot, B. Müller, B. Wehrli, and P. C. Hauser, *Determination of methane and other small hydrocarbons with a platinum–nafion electrode by stripping voltammetry*, Analytica chimica acta, 432 (2001), pp. 1–10.

[71] J. Jang, K. Shen, and C. G. Morales-Guio, *Electrochemical direct partial oxidation of methane to methanol*, Joule, 3 (2019), pp. 2589–2593.

[72] J. S. Jirkovsky, I. Panas, E. Ahlberg, M. Halasa, S. Romani, and D. J. Schiffrin, *Single atom hot-spots at au–pd nanoalloys for electrocatalytic h2o2 production*, Journal of the American Chemical Society, 133 (2011), pp. 19432–19441.

[73] R. Johnson and A. Stanley, *Gc/ms and ft-ir spectra of methoxymethanol*, Applied spectroscopy, 45 (1991), pp. 218–222.

[74] S. W. Jorgensen and R. Madix, *Hydrogen transfer pathways in the oxidation of methanol on pd (100)*, Surface science, 183 (1987), pp. 27–43.

[75] A. Kabbabi, R. Faure, R. Durand, B. Beden, F. Hahn, J.-M. Leger, and C. Lamy, *In situ ftirs study of the electrocatalytic oxidation of carbon monoxide and methanol at platinum–ruthenium bulk alloy electrodes*, Journal of Electroanalytical Chemistry, 444 (1998), pp. 41–53.

[76] J. Kang and E. D. Park, *Aqueous-phase selective oxidation of methane with oxygen over iron salts and pd/c in the presence of hydrogen*, ChemCatChem, 11 (2019), pp. 4247–4251.

[77] Y. Katayama, F. Nattino, L. Giordano, J. Hwang, R. R. Rao, O. Andreussi, N. Marzari, and Y. Shao-Horn, *An in situ surface-enhanced infrared absorption spectroscopy study of electrochemical co2 reduction: selectivity dependence on surface c-bound and o-bound reaction intermediates*, The Journal of Physical Chemistry C, 123 (2018), pp. 5951–5963.

[78] G. Keller and M. Bhasin, *Synthesis of ethylene via oxidative coupling of methane: I. determination of active catalysts*, Journal of Catalysis, 73 (1982), pp. 9–19.

[79] C. S. Kim and C. Korzeniewski, *Vibrational coupling as a probe of adsorption at different structural sites on a stepped single-crystal electrode*, Analytical chemistry, 69 (1997), pp. 2349–2353.

[80] C. S. Kim, W. J. Tornquist, and C. Korzeniewski, *Infrared spectroscopy as a probe of carbon monoxide adsorption at platinum (335) under aqueous electrochemical conditions*, The Journal of Physical Chemistry, 97 (1993), pp. 6484–6491.

[81] R. S. Kim and Y. Surendranath, *Electrochemical reoxidation enables continuous methane-to-methanol catalysis with aqueous pt salts*, ACS central science, 5 (2019), pp. 1179–1186.

[82] B. E. Koel, D. A. Blank, and E. A. Carter, *Thermochemistry of the selective dehydrogenation of cyclohexane to benzene on pt surfaces*, Journal of Molecular Catalysis A: Chemical, 131 (1998), pp. 39–53.

[83] E. V. Kondratenko, T. Peppel, D. Seeburg, V. A. Kondratenko, N. Kalevaru, A. Martin, and S. Wohlrab, *Methane conversion into different hydrocarbons or oxygenates: current status and future perspectives in catalyst development and reactor operation*, Catalysis Science & Technology, 7 (2017), pp. 366–381.

[84] G. Kresse and J. Furthmüller, *Efficiency of ab-initio total energy calculations for metals and semiconductors using a plane-wave basis set*, Computational materials science, 6 (1996), pp. 15–50.

[85] ———, *Efficient iterative schemes for ab initio total-energy calculations using a plane-wave basis set*, Physical review B, 54 (1996), p. 11169.

[86] G. Kresse and J. Hafner, *Ab initio molecular dynamics for liquid metals*, Physical review B, 47 (1993), p. 558.

[87] ———, *Ab initio molecular-dynamics simulation of the liquid-metal–amorphous-semiconductor transition in germanium*, Physical Review B, 49 (1994), p. 14251.

[88] G. Kresse and D. Joubert, *From ultrasoft pseudopotentials to the projector augmented-wave method*, Physical review b, 59 (1999), p. 1758.

[89] K. P. Kuhl, E. R. Cave, D. N. Abram, and T. F. Jaramillo, *New insights into the electrochemical reduction of carbon dioxide on metallic copper surfaces*, Energy & Environmental Science, 5 (2012), pp. 7050–7059.

[90] K. Kunimatsu, T. Sato, H. Uchida, and M. Watanabe, *Adsorption/oxidation of co on highly dispersed pt catalyst studied by combined electrochemical and atr-ftiras methods: oxidation of co adsorbed on carbon-supported pt catalyst and unsupported pt black*, Langmuir, 24 (2008), pp. 3590–3601.

[91] K. Kunimatsu, T. Senzaki, M. Tsushima, and M. Osawa, *A combined surface-enhanced infrared and electrochemical kinetics study of hydrogen adsorption and evolution on a pt electrode*, Chemical physics letters, 401 (2005), pp. 451–454.

[92] G. Kwon, D. Shin, H. Jeong, S. K. Sahoo, J. Lee, G. Kim, J. Choi, D. H. Kim, J. W. Han, and H. Lee, *Oxidative methane conversion to ethane on highly oxidized pd/ceo2 catalysts below 400° c*, ChemSusChem, 13 (2020), pp. 677–681.

[93] J. A. Labinger and J. E. Bercaw, *Understanding and exploiting c–h bond activation*, Nature, 417 (2002), pp. 507–514.

[94] A. H. Larsen, J. J. Mortensen, J. Blomqvist, I. E. Castelli, R. Christensen, M. Dułak, J. Friis, M. N. Groves, B. Hammer, C. Hargus, et al., *The atomic simulation environment—a python library for working with atoms*, Journal of Physics: Condensed Matter, 29 (2017), p. 273002.

[95] N. Lebedeva, M. Koper, J. v. Feliu, and R. Van Santen, *Role of crystalline defects in electrocatalysis: Mechanism and kinetics of co adlayer oxidation on stepped platinum electrodes*, The Journal of Physical Chemistry B, 106 (2002), pp. 12938–12947.

[96] N. Lebedeva, M. Koper, E. Herrero, J. Feliu, and R. Van Santen, *Cooxidation on stepped pt [n (111)×(111)] electrodes*, Journal of Electroanalytical Chemistry, 487 (2000), pp. 37–44.

[97] N. P. Lebedeva, M. T. Koper, J. M. Feliu, and R. A. van Santen, *The effect of the cooling atmosphere in the preparation of flame-annealed pt (111) electrodes on co adlayer oxidation*, Electrochemistry communications, 2 (2000), pp. 487–490.

[98] J. Lee, J. Yang, and J. H. Moon, *Solar cell-powered electrochemical methane-to-methanol conversion with cuo/ceo2 catalysts*, ACS Energy Letters, 6 (2021), pp. 893–899.

[99] J. S. Lee, J. Kim, and Y. Kim, *Methyl formate as a new building block in c1 chemistry*, Applied Catalysis, 57 (1990), pp. 1–30.

[100] L. W. H. Leung and M. J. Weaver, *Real-time ftir spectroscopy as a quantitative kinetic probe of competing electrooxidation pathways of small organic molecules*, The Journal of Physical Chemistry, 92 (1988), pp. 4019–4022.

[101] J. Lichtenberger, D. Lee, and E. Iglesia, *Catalytic oxidation of methanol on pd metal and oxide clusters at near-ambient temperatures*, Physical Chemistry Chemical Physics, 9 (2007), pp. 4902–4906.

[102] M. Lin and A. Sen, *A highly catalytic system for the direct oxidation of lower alkanes by dioxygen in aqueous medium. a formal heterogeneous analog of alkane monooxygenases*, Journal of the American Chemical Society, 114 (1992), pp. 7307–7308.

[103] H. Liu and E. Iglesia, *Selective one-step synthesis of dimethoxymethane via methanol or dimethyl ether oxidation on h3+ n v n mo12-n po40 keggin structures*, The Journal of Physical Chemistry B, 107 (2003), pp. 10840–10847.

[104] ———, *Effects of support on bifunctional methanol oxidation pathways catalyzed by polyoxometallate keggin clusters*, Journal of Catalysis, 223 (2004), pp. 161–169.

[105] M. Lopes, I. Fonseca, P. Olivi, B. Beden, F. Hahn, J. Leger, and C. Lamy, *Integrated electromodulated ir reflectance spectroscopy bands: Part 2: Methanol adsorbates at polycrystalline platinum and pt (111) single-crystal electrodes in acid medium*, Journal of Electroanalytical Chemistry, 346 (1993), pp. 415–432.

[106] A. López-Cudero, A. Cuesta, and C. Gutiérrez, *Potential dependence of the saturation co coverage of pt electrodes: The origin of the pre-peak in co-stripping voltammograms. part 1: Pt (1 1 1)*, Journal of Electroanalytical Chemistry, 579 (2005), pp. 1–12.

[107] Z. Lu, D. Gao, H. Yin, A. Wang, and S. Liu, *Methanol dehydrogenation to methyl formate catalyzed by sio2-, hydroxyapatite-, and mgo-supported copper catalysts and reaction kinetics*, Journal of Industrial and Engineering Chemistry, 31 (2015), pp. 301–308.

[108] J. H. Lunsford, *The catalytic oxidative coupling of methane*, Angewandte Chemie International Edition in English, 34 (1995), pp. 970–980.

[109] H.-B. Ma, T. Sheng, W.-S. Yu, J.-Y. Ye, L.-Y. Wan, N. Tian, S.-G. Sun, and Z.-Y. Zhou, *High catalytic activity of pt (100) for ch4 electrochemical conversion*, ACS Catalysis, 9 (2019), pp. 10159–10165.

[110] M. Ma, B. J. Jin, P. Li, M. S. Jung, J. I. Kim, Y. Cho, S. Kim, J. H. Moon, and J. H. Park, *Ultrahigh electrocatalytic conversion of methane at room temperature*, Advanced Science, 4 (2017), p. 1700379.

[111] S. Maehara, M. Taneda, and K. Kusakabe, *Catalytic synthesis of hydrogen peroxide in microreactors*, Chemical Engineering Research and Design, 86 (2008), pp. 410–415.

[112] S. Maity, R. I. Kaiser, and B. M. Jones, *Formation of complex organic molecules in methanol and methanol–carbon monoxide ices exposed to ionizing radiation–a combined ftir and reflectron time-of-flight mass spectrometry study*, Physical Chemistry Chemical Physics, 17 (2015), pp. 3081–3114.

[113] I. T. McCrum, X. Chen, K. A. Schwarz, M. J. Janik, and M. T. Koper, *Effect of step density and orientation on the apparent ph dependence of hydrogen and hydroxide adsorption on stepped platinum surfaces*, The Journal of Physical Chemistry C, 122 (2018), pp. 16756–16764.

[114] I. T. McCrum and M. J. Janik, *ph and alkali cation effects on the pt cyclic voltammogram explained using density functional theory*, The Journal of Physical Chemistry C, 120 (2016), pp. 457–471.

[115] E. McFarland, *Unconventional chemistry for unconventional natural gas*, Science, 338 (2012), pp. 340–342.

[116] B. A. McGuire, C. N. Shingledecker, E. R. Willis, A. M. Burkhardt, S. El-Abd, R. A. Motiyenko, C. L. Brogan, T. R. Hunter, L. Margulès, J.-C. Guillemin, et al., *Alma detection of interstellar methoxymethanol (ch3och2oh)*, The Astrophysical Journal Letters, 851 (2017), p. L46.

[117] N. E. McGuire, N. P. Sullivan, O. Deutschmann, H. Zhu, and R. J. Kee, *Dry reforming of methane in a stagnation-flow reactor using rh supported on strontium-substituted hexaaluminate*, Applied Catalysis A: General, 394 (2011), pp. 257–265.

[118] R. McVicker, N. Agarwal, S. J. Freakley, Q. He, S. Althahban, S. H. Taylor, C. J. Kiely, and G. J. Hutchings, *Low temperature selective oxidation of methane using gold-palladium colloids*, Catalysis Today, 342 (2020), pp. 32–38.

[119] A. Miki, S. Ye, and M. Osawa, *Surface-enhanced ir absorption on platinum nanoparticles: an application to real-time monitoring of electrocatalytic reactions*, Chemical Communications, (2002), pp. 1500–1501.

[120] E. Miyazaki and I. Yasumori, *Kinetics of the catalytic decomposition of methanol, formaldehyde and methyl formate over a copper-wire surface*, Bulletin of the Chemical Society of Japan, 40 (1967), pp. 2012–2017.

[121] J. Moran, A. Preetz, R. A. Mesch, and M. J. Krische, *Iridium-catalysed direct c–c coupling of methanol and allenes*, Nature Chemistry, 3 (2011), pp. 287–290.

[122] K. Moshammer, L. Seidel, Y. Wang, H. Selim, S. M. Sarathy, F. Mauss, and N. Hansen, *Aromatic ring formation in opposed-flow diffusive 1, 3-butadiene flames*, Proceedings of the Combustion Institute, 36 (2017), pp. 947–955.

[123] A. J. Nagy, G. Mestl, and R. Schlögl, *The role of subsurface oxygen in the silver-catalyzed, oxidative coupling of methane*, Journal of Catalysis, 188 (1999), pp. 58–68.

[124] E. National Academies of Sciences and Medicine, *The Changing Landscape of Hydrocarbon Feedstocks for Chemical Production: Implications for Catalysis: Proceedings of a Workshop*, The National Academies Press, Washington, DC, 2016.

[125] R. Nichols and A. Bewick, *Spectroscopic identification of the adsorbed intermediate in hydrogen evolution on platinum*, Journal of electroanalytical chemistry and interfacial electrochemistry, 243 (1988), pp. 445–453.

[126] L. Niedrach and M. Tochner, *Studies of hydrocarbon fuel cell anodes by the multipulse potentiodynamic method: Iv. effect of various electrolytes on the behavior of hydrocarbons on conducting porous teflon electrodes*, Journal of The Electrochemical Society, 114 (1967), p. 233.

[127] L. W. Niedrach, *Studies of hydrocarbon fuel cell anodes by the multipulse potentiodynamic method: Ii. behavior of methane on conducting porous teflon electrodes*, Journal of The Electrochemical Society, 113 (1966), p. 645.

[128] I.-C. Oğuz, T. Mineva, and H. Guesmi, *The effect of pd ensemble structure on the o2 dissociation and co oxidation mechanisms on au—pd (100) surface alloys*, The Journal of Chemical Physics, 148 (2018), p. 024701.

[129] T. J. Omasta, W. A. Rigdon, C. A. Lewis, R. J. Stanis, R. Liu, C. Q. Fan, and W. E. Mustain, *Two pathways for near room temperature electrochemical conversion of methane to methanol*, ECS Transactions, 66 (2015), p. 129.

[130] M. Osawa, M. Tsushima, H. Mogami, G. Samjeské, and A. Yamakata, *Structure of water at the electrified platinum- water interface: A study by surface-enhanced infrared absorption spectroscopy*, The Journal of Physical Chemistry C, 112 (2008), pp. 4248–4256.

[131] C. Papp, B. Tränkenschuh, R. Streber, T. Fuhrmann, R. Denecke, and H.-P. Steinrück, *Influence of steps on the adsorption of methane on platinum surfaces*, The Journal of Physical Chemistry C, 111 (2007), pp. 2177–2184.

[132] J. Perez, B. Beden, F. Hahn, A. Aldaz, and C. Lamy, *"in situ" infrared reflectance spectroscopic study of the early stages of ethanol adsorption at a platinum electrode in acid medium*, Journal of electroanalytical chemistry and interfacial electrochemistry, 262 (1989), pp. 251–261.

[133] M. L. Perry and T. F. Fuller, *A historical perspective of fuel cell technology in the 20th century*, Journal of the electrochemical society, 149 (2002), p. S59.

[134] E. Pizzutilo, S. J. Freakley, S. Cherevko, S. Venkatesan, G. J. Hutchings, C. H. Liebscher, G. Dehm, and K. J. Mayrhofer, *Gold–palladium bimetallic catalyst stability: consequences for hydrogen peroxide selectivity*, ACS catalysis, 7 (2017), pp. 5699–5705.

[135] E. Pizzutilo, O. Kasian, C. H. Choi, S. Cherevko, G. J. Hutchings, K. J. Mayrhofer, and S. J. Freakley, *Electrocatalytic synthesis of hydrogen peroxide on au-pd nanoparticles: From fundamentals to continuous production*, Chemical physics letters, 683 (2017), pp. 436–442.

[136] A. Plauck, E. E. Stangland, J. A. Dumesic, and M. Mavrikakis, *Active sites and mechanisms for h2o2 decomposition over pd catalysts*, Proceedings of the National Academy of Sciences, 113 (2016), pp. E1973–E1982.

[137] A. Prajapati, B. A. Collins, J. D. Goodpaster, and M. R. Singh, *Fundamental insight into electrochemical oxidation of methane towards methanol on transition metal oxides*, Proceedings of the National Academy of Sciences, 118 (2021).

[138] G. Prieto, *Carbon dioxide hydrogenation into higher hydrocarbons and oxygenates: thermodynamic and kinetic bounds and progress with heterogeneous and homogeneous catalysis*, ChemSusChem, 10 (2017), pp. 1056–1070.

[139] G. Psofogiannakis, A. St-Amant, and M. Ternan, *Methane oxidation mechanism on pt (111): a cluster model dft study*, The Journal of Physical Chemistry B, 110 (2006), pp. 24593–24605.

[140] R. B. Rankin and J. Greeley, *Trends in selective hydrogen peroxide production on transition metal surfaces from first principles*, Acs Catalysis, 2 (2012), pp. 2664–2672.

[141] M. Ravi, M. Ranocchiari, and J. A. van Bokhoven, *The direct catalytic oxidation of methane to methanol—a critical assessment*, Angewandte Chemie International Edition, 56 (2017), pp. 16464–16483.

[142] R. M. Rioux, A. L. Marsh, J. Gaughan, and G. Somorjai, *Oxidation and reforming reactions of ch4 on a stepped pt (5 5 7) single crystal*, Catalysis today, 123 (2007), pp. 265–275.

[143] L. Ruwe, K. Moshammer, N. Hansen, and K. Kohse-Höinghaus, *Influences of the molecular fuel structure on combustion reactions towards soot precursors in selected alkane and alkene flames*, Physical Chemistry Chemical Physics, 20 (2018), pp. 10780–10795.

[144] J. Sambeth, L. Gambaro, and H. Thomas, *Study of the adsorption/oxidation of methanol over vanadium pentoxide*, Adsorption Science & Technology, 12 (1995), pp. 171–180.

[145] J. Sambeth, A. Juan, L. Gambaro, and H. Thomas, *Catalytic oxidation of ch3oh to hcooch3 on v2o5: A theoretical study*, Journal of Molecular Catalysis A: Chemical, 118 (1997), pp. 283–291.

[146] J. E. Sambeth, M. A. Centeno, A. Paúl, L. E. Briand, H. J. Thomas, and J. A. Odriozola, *In situ drifts study of the adsorption–oxidation of ch3oh on v2o5*, Journal of Molecular Catalysis A: Chemical, 161 (2000), pp. 89–97.

[147] G. Samjeské, K.-i. Komatsu, and M. Osawa, *Dynamics of co oxidation on a polycrystalline platinum electrode: A time-resolved infrared study*, The Journal of Physical Chemistry C, 113 (2009), pp. 10222–10228.

[148] T. Sato, K. Kunimatsu, H. Uchida, and M. Watanabe, *Adsorption/oxidation of co on highly dispersed pt catalyst studied by combined electrochemical and atr-ftiras methods: Part 1. atr-ftiras spectra of co adsorbed on highly dispersed pt catalyst on carbon black and carbon un-supported pt black*, Electrochimica Acta, 53 (2007), pp. 1265–1278.

[149] A. Sattler, *Hydrogen/deuterium (h/d) exchange catalysis in alkanes*, ACS Catalysis, 8 (2018), pp. 2296–2312.

[150] S. Schauermann, J. Hoffmann, V. Johánek, J. Hartmann, and J. Libuda, *Adsorption, decomposition and oxidation of methanol on alumina supported palladium particles*, Physical Chemistry Chemical Physics, 4 (2002), pp. 3909–3918.

[151] K. Schwarz, B. Xu, Y. Yan, and R. Sundararaman, *Partial oxidation of step-bound water leads to anomalous ph effects on metal electrode step-edges*, Physical Chemistry Chemical Physics, 18 (2016), pp. 16216–16223.

[152] M. Shao and R. Adzic, *Electrooxidation of ethanol on a pt electrode in acid solutions: in situ atr-seiras study*, Electrochimica Acta, 50 (2005), pp. 2415–2422.

[153] S. M. Sharada, R. K. Karlsson, Y. Maimaiti, J. Voss, and T. Bligaard, *Adsorption on transition metal surfaces: Transferability and accuracy of dft using the ads41 dataset*, Physical Review B, 100 (2019), p. 035439.

[154] K. Shaw, P. Christensen, and A. Hamnett, *Photoelectrochemical oxidation of organics on single-crystal tio2: an in situ ftir study*, Electrochimica acta, 41 (1996), pp. 719–728.

[155] W. Sheng, Z. Zhuang, M. Gao, J. Zheng, J. G. Chen, and Y. Yan, *Correlating hydrogen oxidation and evolution activity on platinum at different ph with measured hydrogen binding energy*, Nature communications, 6 (2015), pp. 1–6.

[156] J. J. Siirola, *The impact of shale gas in the chemical industry*, AIChE Journal, 60 (2014), pp. 810–819.

[157] H. Siwek, M. Łukaszewski, and A. Czerwiński, *Electrochemical study on the adsorption of carbon oxides and oxidation of their adsorption products on platinum group metals and alloys*, Physical Chemistry Chemical Physics, 10 (2008), pp. 3752–3765.

[158] T. Smolinka, M. Heinen, Y. Chen, Z. Jusys, W. Lehnert, and R. Behm, *Co2 reduction on pt electrocatalysts and its impact on h2 oxidation in co2 containing fuel cell feed gas–a combined in situ infrared spectroscopy, mass spectrometry and fuel cell performance study*, Electrochimica Acta, 50 (2005), pp. 5189–5199.

[159] M. Stöcker, *Methanol-to-hydrocarbons: catalytic materials and their behavior*, Microporous and mesoporous materials, 29 (1999), pp. 3–48.

[160] K. Stowers, R. Madix, and C. Friend, *From model studies on au (1 1 1) to working conditions with unsupported nanoporous gold catalysts: Oxygen-assisted coupling reactions*, Journal of catalysis, 308 (2013), pp. 131–141.

[161] R. Sun, I. Delidovich, and R. Palkovits, *Dimethoxymethane as a cleaner synthetic fuel: synthetic methods, catalysts, and reaction mechanism*, ACS Catalysis, 9 (2019), pp. 1298–1318.

[162] S. Sun, J. Clavilier, and A. Bewick, *The mechanism of electrocatalytic oxidation of formic acid on pt (100) and pt (111) in sulphuric acid solution: an emirs study*, Journal of electroanalytical chemistry and interfacial electrochemistry, 240 (1988), pp. 147–159.

[163] S.-G. Sun, P. A. Christensen, and A. Wieckowski, *In-situ spectroscopic studies of adsorption at the electrode and electrocatalysis*, Elsevier, 2011.

[164] V. L. Sushkevich, D. Palagin, M. Ranocchiari, and J. A. Van Bokhoven, *Selective anaerobic oxidation of methane enables direct synthesis of methanol*, Science, 356 (2017), pp. 523–527.

[165] M. Szwarc, *The c–h bond energy in toluene and xylenes*, The Journal of Chemical Physics, 16 (1948), pp. 128–136.

[166] K. Takahashi, N. Takezawa, and H. Kobayashi, *Mechanism of formation of methyl formate from formaldehyde over copper catalysts*, Chemistry Letters, 12 (1983), pp. 1061–1064.

[167] Y. Takahashi, T. Higuchi, O. Sekiguchi, A. Fujizuka, S. Nakajima, and S. Tajima, *Unimolecular metastable decompositions of gem-dimethoxyalkanes (rr'c(och3)2) upon electron impact. i. dimethoxymethane and 1, 1-dimethoxyethane*, Rapid Communications in Mass Spectrometry, 14 (2000), pp. 61–67.

[168] J. Tatibouet, *Methanol oxidation as a catalytic surface probe*, Applied Catalysis A: General, 148 (1997), pp. 213–252.

[169] J.-M. Tatibouët and H. Lauron-Pernot, *Transient isotopic study of methanol oxidation on unsupported v2o5: Mechanism of methylal formation*, Journal of Molecular Catalysis A: Chemical, 171 (2001), pp. 205–216.

[170] A. Taylor and S. Brummer, *The adsorption and oxidation of hydrocarbons on noble metal electrodes. vii. oxidative adsorption of methane on platinum electrodes*, The Journal of Physical Chemistry, 72 (1968), pp. 2856–2862.

[171] W. Tu and Y. H. Chin, *Catalytic consequences of chemisorbed oxygen during methanol oxidative dehydrogenation on pd clusters*, ACS Catalysis, 5 (2015), pp. 3375–3386.

[172] M. J. Van Der Niet, N. Garcia-Araez, J. Hernández, J. M. Feliu, and M. T. Koper, *Water dissociation on well-defined platinum surfaces: The electrochemical perspective*, Catalysis today, 202 (2013), pp. 105–113.

[173] A. Venezia, V. La Parola, G. Deganello, B. Pawelec, and J. Fierro, *Synergetic effect of gold in au/pd catalysts during hydrodesulfurization reactions of model compounds*, Journal of Catalysis, 215 (2003), pp. 317–325.

[174] I. Villegas and M. J. Weaver, *Carbon monoxide adlayer structures on platinum (111) electrodes: A synergy between in-situ scanning tunneling microscopy and infrared spectroscopy*, The Journal of chemical physics, 101 (1994), pp. 1648–1660.

[175] F. Viñes, Y. Lykhach, T. Staudt, M. P. Lorenz, C. Papp, H.-P. Steinrück, J. Libuda, K. M. Neyman, and A. Görling, *Methane activation by platinum: Critical role of edge and corner sites of metal nanoparticles*, Chemistry–A European Journal, 16 (2010), pp. 6530–6539.

[176] I. E. Wachs and R. J. Madix, *The oxidation of methanol on a silver (110) catalyst*, Surface Science, 76 (1978), pp. 531–558.

[177] R. Wang, Z. Wu, C. Chen, Z. Qin, H. Zhu, G. Wang, H. Wang, C. Wu, W. Dong, W. Fan, et al., *Graphene-supported au–pd bimetallic nanoparticles with excellent catalytic performance in selective oxidation of methanol to methyl formate*, Chemical communications, 49 (2013), pp. 8250–8252.

[178] Y. L. Wang, S. Gurses, N. Felvey, A. Boubnov, S. S. Mao, and C. X. Kronawitter, *In situ deposition of pd during oxygen reduction yields highly selective and active electrocatalysts for direct h2o2 production*, ACS Catalysis, 9 (2019), pp. 8453–8463.

[179] Y. L. Wang, S. Gurses, N. Felvey, and C. X. Kronawitter, *Room temperature and atmospheric pressure aqueous partial oxidation of ethane to oxygenates over aupd catalysts*, Catalysis Science & Technology, 10 (2020), pp. 6679–6686.

[180] S. Watanabe, J. Inukai, and M. Ito, *Coverage and potential dependent co adsorption on pt (1111),(711) and (100) electrode surfaces studied by infrared reflection absorption spectroscopy*, Surface science, 293 (1993), pp. 1–9.

[181] R. S. Weber, J. E. Holladay, C. Jenks, E. A. Panisko, L. J. Snowden-Swan, M. Ramirez-Corredores, B. Baynes, L. T. Angenent, and D. Boysen, *Modularized production of fuels and other value-added products from distributed, wasted, or stranded feedstocks*, Wiley Interdisciplinary Reviews: Energy and Environment, 7 (2018), p. e308.

[182] G. T. Whiting, S. A. Kondrat, C. Hammond, N. Dimitratos, Q. He, D. J. Morgan, N. F. Dummer, J. K. Bartley, C. J. Kiely, S. H. Taylor, et al., *Methyl formate formation from methanol oxidation using supported gold–palladium nanoparticles*, ACS Catalysis, 5 (2015), pp. 637–644.

[183] C. Williams, J. H. Carter, N. F. Dummer, Y. K. Chow, D. J. Morgan, S. Yacob, P. Serna, D. J. Willock, R. J. Meyer, S. H. Taylor, et al., *Selective oxidation of methane to methanol using supported aupd catalysts prepared by stabilizer-free sol-immobilization*, ACS Catalysis, 8 (2018), pp. 2567–2576.

[184] R. Wojcieszak, E. M. Gaigneaux, and P. Ruiz, *Low temperature-high selectivity process over supported pd nanoparticles in partial oxidation of methanol*, ChemCatChem, 4 (2012), pp. 72–75.

[185] R. Wojcieszak, E. M. Gaigneaux, and P. Ruiz, *Direct methyl formate formation from methanol over supported palladium nanoparticles at low temperature*, ChemCatChem, 5 (2013), pp. 339–348.

[186] R. Wojcieszak, M. Ghazzal, E. M. Gaigneaux, and P. Ruiz, *Low temperature oxidation of methanol to methyl formate over pd nanoparticles supported on γ-fe 2 o 3*, Catalysis Science & Technology, 4 (2014), pp. 738–745.

[187] R. Wojcieszak, A. Karelovic, E. M. Gaigneaux, and P. Ruiz, *Oxidation of methanol to methyl formate over supported pd nanoparticles: insights into the reaction mechanism at low temperature*, Catalysis Science & Technology, 4 (2014), pp. 3298–3305.

[188] J.-b. WU, R.-p. SHI, Z.-f. QIN, L. Huan, Z.-k. LI, H.-q. ZHU, Y.-x. ZHAO, and J.-g. WANG, *Selective oxidation of methanol to methyl formate over bimetallic au-pd nanoparticles supported on sio2*, Journal of Fuel Chemistry and Technology, 47 (2019), pp. 780–790.

[189] C. Xia, Y. Xia, P. Zhu, L. Fan, and H. Wang, *Direct electrosynthesis of pure aqueous h2o2 solutions up to 20% by weight using a solid electrolyte*, Science, 366 (2019), pp. 226–231.

[190] B. Xu and C. M. Friend, *Oxidative coupling of alcohols on gold: Insights from experiments and theory*, Faraday Discussions, 152 (2011), pp. 307–320.

[191] J. Xu and J. T. Yates Jr, *Catalytic oxidation of co on pt (335): a study of the active site*, The Journal of chemical physics, 99 (1993), pp. 725–732.

[192] Y.-G. Yan, Y.-Y. Yang, B. Peng, S. Malkhandi, A. Bund, U. Stimming, and W.-B. Cai, *Study of co oxidation on polycrystalline pt electrodes in acidic solution by atr-seiras*, The Journal of Physical Chemistry C, 115 (2011), pp. 16378–16388.

[193] S. Yang, A. Verdaguer-Casadevall, L. Arnarson, L. Silvioli, V. Colic, R. Frydendal, J. Rossmeisl, I. Chorkendorff, and I. E. Stephens, *Toward the decentralized electrochemical production of h2o2: a focus on the catalysis*, Acs Catalysis, 8 (2018), pp. 4064–4081.

[194] J. T. Yates Jr, *Surface chemistry at metallic step defect sites*, Journal of Vacuum Science & Technology A: Vacuum, Surfaces, and Films, 13 (1995), pp. 1359–1367.

[195] W.-Y. Yu, L. Zhang, G. M. Mullen, G. Henkelman, and C. B. Mullins, *Oxygen activation and reaction on pd–au bimetallic surfaces*, The Journal of Physical Chemistry C, 119 (2015), pp. 11754–11762.

[196] Y. Yuan, J. Wang, S. Adimi, H. Shen, T. Thomas, R. Ma, J. P. Attfield, and M. Yang, *Zirconium nitride catalysts surpass platinum for oxygen reduction*, Nature Materials, 19 (2020), pp. 282–286.

[197] M. Zboray, A. T. Bell, and E. Iglesia, *Role of c- h bond strength in the rate and selectivity of oxidative dehydrogenation of alkanes*, The Journal of Physical Chemistry C, 113 (2009), pp. 12380–12386.

[198] R. Zhang, L. Song, and Y. Wang, *Insight into the adsorption and dissociation of ch4 on pt (h k l) surfaces: A theoretical study*, Applied surface science, 258 (2012), pp. 7154–7160.

[199] J. Zheng, W. Sheng, Z. Zhuang, B. Xu, and Y. Yan, *Universal dependence of hydrogen oxidation and evolution reaction activity of platinum-group metals on ph and hydrogen binding energy*, Science advances, 2 (2016), p. e1501602.

[200] B. Zhou, E. Huang, R. Almeida, S. Gurses, A. Ungar, J. Zetterberg, A. Kulkarni, C. X. Kronawitter, D. L. Osborn, N. Hansen, et al., *Near-surface imaging of the multicomponent gas phase above a silver catalyst during partial oxidation of methanol*, ACS Catalysis, 11 (2020), pp. 155–168.

[201] Y. Zhu, H. Uchida, and M. Watanabe, *Oxidation of carbon monoxide at a platinum film electrode studied by fourier transform infrared spectroscopy with attenuated total reflection technique*, Langmuir, 15 (1999), pp. 8757–8764.